CHARLES UNIVERSITY PRAGUE

faculty of mathematics and physics

DOCTORAL THESIS

Plasma polymerization in biomedical applications

Andrey Grinevich

Prague, 2008

Aims of the thesis

In general these studies were focused on plasma polymerization processes in order to prepare and characterize thin films for surface modification for biomedical applications. The aims were as follows:

- Study deposition process of nanocomposite metal/plasma polymer films especially using titanium as a metal;
- Characterize deposited films in order to determine their structure, morphology, composition and surface energy using TEM, XPS, RBS/ERDA and contact angle measurements;
- Study deposited nanocomposite films using SPM method;
- Study biological response of the nanocomposite Ti/hydrocarbon plasma polymer films in terms of adsorption and adhesion of proteins and cells; adhesion, growth and differentiation of human osteoblast-like MG 63 cells as well as bovine pulmonary artery endothelial cells of the line CPAE on nanocomposite Ti/hydrocarbon plasma polymer films;
- Study modification of polymer especially polypropylene using DC discharges operated in oxygen, water vapor and in a flowing afterglow of water vapor discharge;
- Characterize modified polypropylene surfaces – their structure, chemical composition, morphology and surface energy by means of AFM, XPS, FTIR and contact angle analysis.

The last two aims were performed in the collaboration with Prof. Rybkin DrSc from Ivanovo State University of Chemistry and Technology, Russia and during my visit to National Institute for Material Science in Tsukuba, Japan.

Acknowledgements

Without the help of many colleagues and friends from the Charles University and other academia abroad, this work could not come into being even as little perfect as it is in its current "final" stage. Therefore I would like to acknowledge the generous support of all these people.

First of all I'm very indebted to my supervisor Prof. RNDr. H. Biederman DrSc and co-supervisor Doc. D. Savinska CSc for their continuous interest, advises and help in accomplishing the experiments and writing the thesis.

I would like to thank my ex-supervisor Prof. Rybkin DrSc under guidance of whom I started my first steps in science and who helped me to accomplish the second part of this work.

For inestimable help in writing this thesis, in neat remarks and current discussions of results during the course of this work I would like to thank in particular senior assistant professor Ing. Andrey Shukurov PhD.

I'm very thankful to MUDr Lucie Bacakova MD, PhD and her colleagues for their help in implementation of biological tests; to doc. Rndr. Josef Pešička, Csc. for TEM and to Rndr. Anna Macková, PhD and Anna Boldyryeva, PhD for RBS/ERDA analysis.

I would like to thank my supervisor Dr. Akiko Itakura and my Japanese colleague and good friend Keisuke Sagisaka PhD for their help and support during my one year stay in Japan in National Institute for Materials Science.

Also I am very obliged to fellow members of Prof. Biederman's group: Jan Hanus PhD, Oleksandr Polonskyi, Jaroslav Kousal PhD, Jindrich Matousek, Martin Drabik, Pavel Solar and Marcela Ublanska for a good and memorable time.

And at last but not at least, I'm obliged very much to my family and friends for the encouragements and untold support.

This work was supported by:

MSM 0021620834 (MŠMT ČR)

1P05OC008 (COST 527)

OC 521.10 (COST527)

1P05ME754 (MŠMT ČR)

BM MSM 113200002 (MŠMT ČR)

KAN101120701 (GAAV ČR)

Contents

Chapter 1 Introduction

Introduction

1.1 Basics of plasma polymerization

Plasma Enhanced Chemical Vapor Deposition (PECVD) of organic compounds, also called plasma polymerization, is a method of deposition of polymer-like thin films by means of a glow discharge, ignited in an atmosphere of organic monomer vapors usually under low pressure. Electrons, gaining energy from the externally applied electric field, excite or ionize the precursor molecules to produce a highly reactive environment. Ions, electrons, photons, radicals and excited species take part in diverse chemical reactions both in the plasma volume and on adjacent surfaces. Some of them may participate in the creation of a plasma polymer network. Since plasma polymerization involves the fragmentation of precursor molecules, the resulting chemical structure of plasma polymer is irregular. For this reason, plasma polymer is essentially different from conventional polymer, which consists of unique units repeating along a polymer chain.

According to [1], plasma polymer formation may be represented by a mechanism of competitive ablation and polymerization (Fig. 1-1). Ablation involves the removal of a portion of solid material from the surface and can be caused both by chemical etching and ion bombardment. Some species arriving at the surface may react with the growing polymer chains to produce non-polymerizable volatile products, which are removed from the deposition zone by pumping. Alternatively, ion sputtering can cause ablation. Generally, a plasma polymer is an isolating material and its surface floats at a negative potential with respect to positive plasma. The potential drop between surface and plasma occurs over a distance called the sheath. Positive ions accelerated in the sheath bombard the surface producing sputtering or restructuring of the outer layers.

The first kinetic models of plasma polymerization date back to the 1960s [2]. It is generally recognized that plasma polymer formation occurs by a combination of processes which

involve gas phase reactions and those at the gas-surface interface. Plasma deposition conditions determine the relative contribution of each mechanism to the overall deposition process.

Williams and Hayes [3] excited an AC (10 kHz) discharge in styrene at a pressure 0.1 – 3 torr using a bell-jar-type reactor with a parallel plate electrode system. They found, that at constant substrate temperature and constant flow of styrene, the polymerization rate at first increased and then reached saturation with either increased pressure at constant discharge current or with increased current at a constant pressure. They also found that the polymerization rate increases with decreasing substrate temperature. Plasma polymer formation proceeds as follows. Positive ions are formed by collisions between the energetic electrons and monomer molecules in the negative glow. These ions are attracted to the electrodes and bombard in the first stage of growth adsorbed monomer molecules. These are activated (fragmented) and react with the unactivated monomer molecules. When the first layers of plasma polymer are created not only adsorbed monomer molecules are activated but also polymer surface molecules. These active species propagate the polymerization reaction by addition of unactivated molecules.

Denaro et al. [4-6] proposed the explanation of plasma polymerization of styrene (at 1 torr) and some other monomers in a 2 MHz discharge. The initiation of the polymerization reaction was done by energetic electrons bombarding the polymer film that was covering the electrodes and resulted in the creation of surface free radicals that react with the adsorbed monomer molecules. They obtained a good agreement with the experiment in case of allylalcohol [6]. A similar model was proposed by Westwood [7] who used a parallel-plate electrode system in RF discharge and relied in his model on activation by bombarding positive ions.

Poll et al. [8, 9] developed a detailed model based mainly on the processes on the surfaces adjacent to the discharge region, e.g. adsorption, desorption and polymerization. He also considered processes leading to the formation of new compounds by the transformation of the monomer under the influence of the discharge. Comparison to the experiment is done for C_2F_4.

Lam et al. [10] developed a model of plasma polymerization of styrene in a RF (800 kHz) discharge using a capacitively coupled parallel plate electrode system. Three steps were considered: (1) Initiations of monomers by electron impact was followed by (2) propagation and (3) termination as in conventional polymerization. Free radical polymerization was assumed. Four mechanism models were examined considering the above mentioned three steps taking place either in the gas phase or on the surface. Comparing the theory and experiment, the following model seemed to be the most probable: Monomers are activated in

the gas phase via collisions with energetic electrons. They diffuse to the surface where they react in propagation reactions with adsorbed monomers and subsequently terminate.

A similar model as above for plasma polymerization of unsaturated hydrocarbons in a RF discharge was proposed by Tibbitt et al. [11].

The overall scheme of plasma polymerization based on Poll's et al. [9] work was proposed by Yasuda and Hsu [12].

According to Yasuda [1], plasma polymer deposition is composed of plasma-state-polymerization and plasma-induced polymerization. The former is a combination of deposition processes from polymer-forming intermediate species produced in plasma and it is believed to be the main route of polymer formation. In some cases, however, when the monomer contains polymerizable structures (e.g. vinyl groups), conventional molecular polymerization on the surfaces activated by plasma can occur. This is so-called plasma-induced polymerization. It is argued that this route of polymerization is likely only at high pressure and low substrate temperature [1].

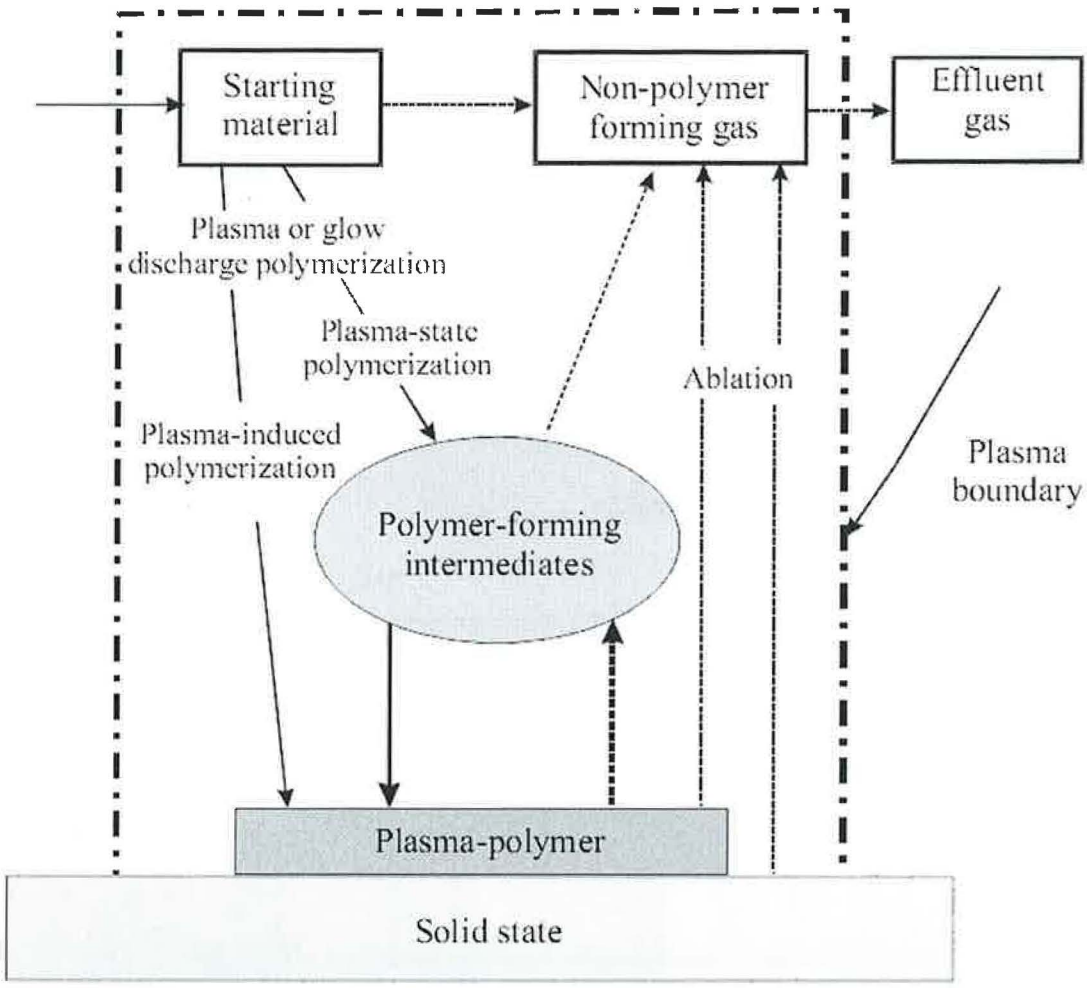

Fig. 1-1 The plasma polymerization scheme (taken from [1])

As to the kinetics of plasma polymerization, Yasuda suggests that the most probable mechanism for all kind of the monomers is rapid step-growth polymerization via free radicals, represented by the following scheme (Fig. 1-2). In this picture, M stands for any neutral species. M• represents the monofunctional activated species, particularly free radicals, capable of covalent bond formation. Bifunctional activated species are given by •M•.

There are two major channels of step growth, which involve the polymerization via mono- (Cycle I) and bifunctional (Cycle II) radicals. Reactions 1 and 4 are the first step with chain propagating through the repeated addition of radicals to the unactivated species. The latter must contain a chemical structure allowing the addition of M•. Reaction 2 represents the termination through radical recombination. Reaction 3 is a recombination of mono- and biradicals, which yields another monofunctional radical. Reaction 5 is a recombination of two bifunctional radicals.

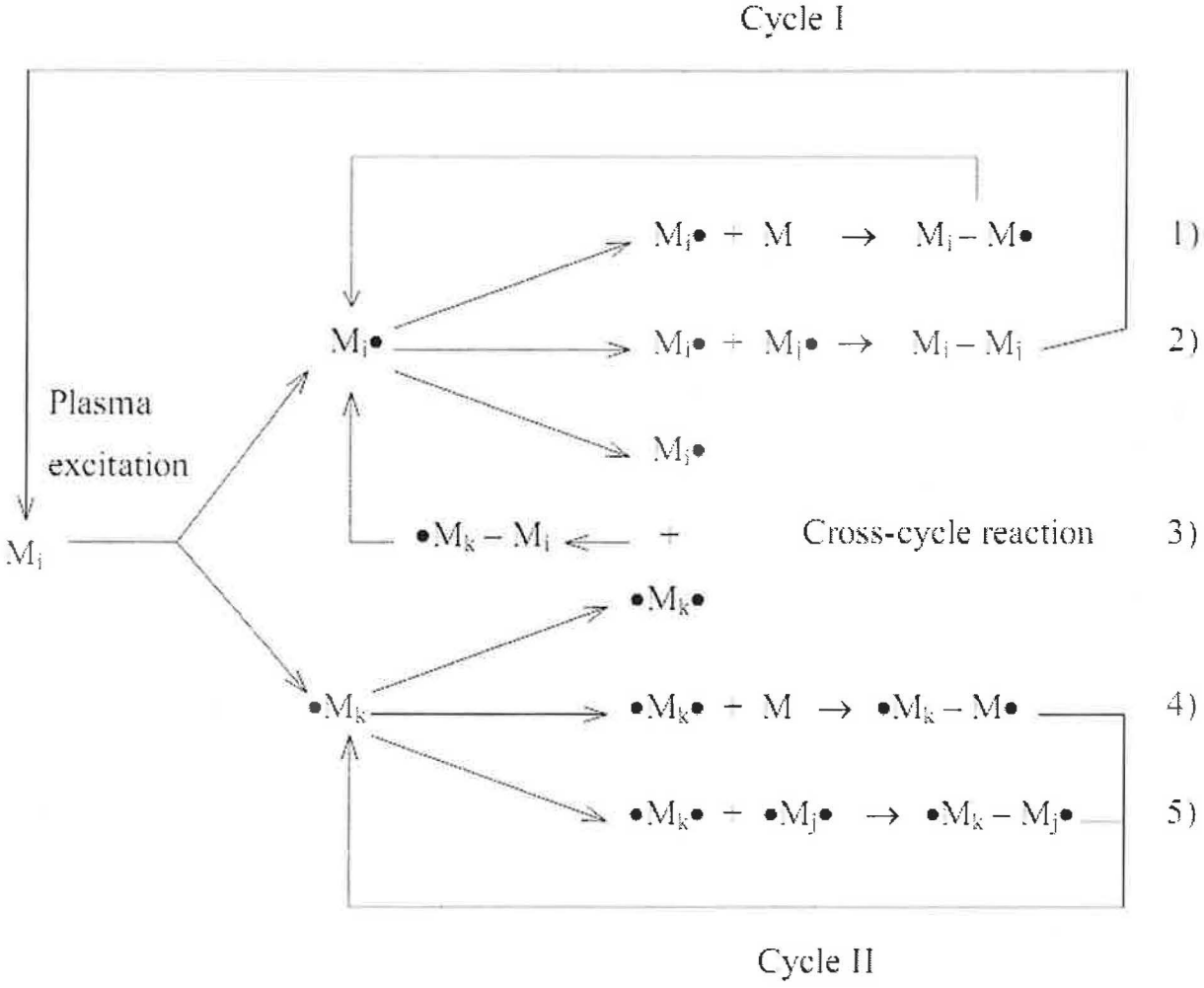

Fig. 1-2 The mechanism of plasma polymerization (taken from [1])

Plasma polymerization is nonspecific, i.e. the chemical nature of monomers is not that crucial as in conventional polymerization. The vinyl and saturated vinyl compounds polymerize by conventional methods with the rates, which are different in orders of magnitude. The rates of plasma polymerization for the same compounds vary only in an order of magnitude and the identical coatings can be obtained from the different precursors [1]. According to Yasuda, the monomers can be divided into three groups:

I) aromatic and triple bonds bearing compounds;

II) compounds bearing double bonds and cyclic structures;

III) compounds with ordinary bonds.

The structure of a monomer determines the predominance of Cycle I or Cycle II in overall polymerization reaction. Double and triple bonds and cyclic structures cleave with formation of biradicals (Cycle II). Monomers from group III produce free monoradicals, mainly by hydrogen detachment, and the main route of polymerization is Cycle I.

An activated-growth model (AGM) has been suggested by d'Agostino [13] for plasma polymerization from fluorocarbon feeds. The film is established to grow via the reactions of CFx radicals with activated sites on polymeric surfaces.

The processing discharge plasmas are typically electrically excited and sustained. A wide range of operating frequencies ranging from DC, AC, and RF up to MW can be applied, resulting in different coupling modes and substantially differing characteristics. The most relevant arrangement for this work is the parallel plate configuration with DC field applied, shown in Fig. 1-3. The glow discharge between two electrodes is ignited raising the applied electrode voltage to value V_i sufficient for electrical break-down, which depends on used gas and cathode material, the gas pressure p, and the electrode distance d according to Paschen's law $V_i = V_i(p \cdot d)$. Afterwards, the glow discharge is sustained at lower voltage, usually in the abnormal mode, with negative glow filling the interelectrode space. Because of the electric excitation, the energy deposition pathway in such plasma is from the field to the charged particles and in collisions from the charged particles to the gas atoms and molecules, important for the production of new particles by ionization, and to the surface interfaces. The electron and ion energy distributions are determined by a dynamic balance between the energy coupled into the plasma and energy losses in the collisions. Due to the large mass difference between electrons and ions, the field energy is most efficiently coupled to the lighter electrons. The rather inefficient collisional energy transfer between the ions and electrons leads to a nonequilibrium plasma with two groups of particles having largely different energies – expressed in terms of energy under the assumption of Maxwellian energy distribution.

Electrons possess temperatures of few eV typically while the ions in bulk are basically cold, at room temperature. In order to prevent the more mobile electrons from leaking off the plasma bulk, positive space charge and electric field builds up in the edge region, the so-called sheath, so that potential in the bulk of electropositive plasma is positive with respect to all walls (see Fig. 1-3. This field in the sheaths accelerates the ions, so that they can reach at active electrodes rather high energies of few 100 eV and cause ion bombardment of the surfaces.

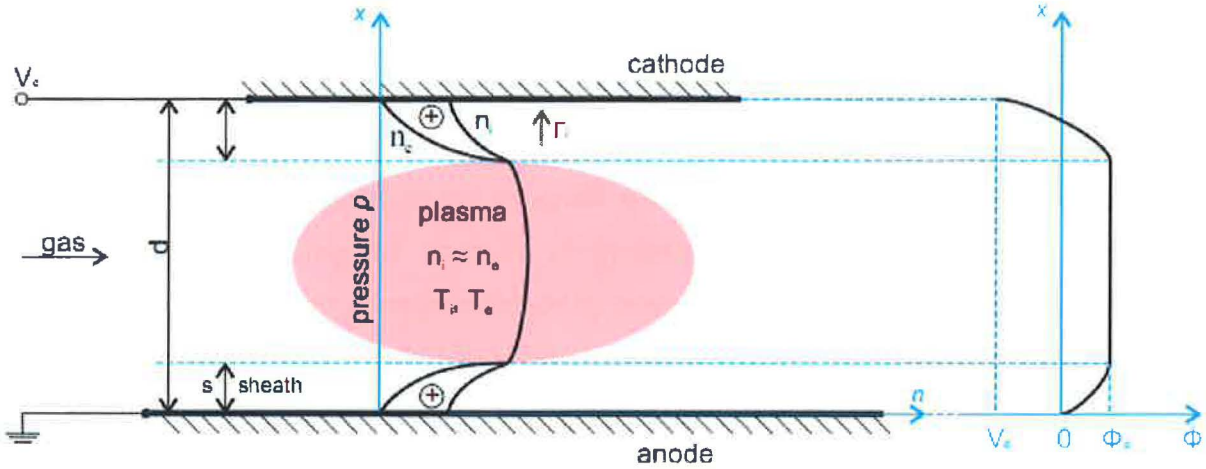

Fig. 1-3 DC discharge arrangement: sheaths, charge densities, flux, and the potential in electropositive plasma

1.2 Carbon based coatings

Thin carbonaceous coatings applied on the top of bulk materials provide a large scale of possibilities to improve or completely modify the surface properties. Selecting the proper deposition conditions, a wide variety of so-called diamond-like-carbon (DLC) coatings with different ratios of sp^3 and sp^2 hybridized carbon-carbon bonds and varying hydrogen content, ranging between the crystalline graphite and diamond films can be achieved. It is largely accepted, that the tetragonal sp^3 bonding is responsible for the mechanical properties while the electrical properties are governed by trigonal sp^2 bonds. Several categories of DLC coatings along with typical techniques of deposition and properties are summarized in Fig. 1-4 and Table 1-1. Soft, partially conducting materials with highest sp^2 hybridization and lowest H content, most resembling the structure of graphite, are typically prepared by physical deposition of carbon such as evaporation or by combustion of resins. Tetrahedral amorphous carbon (ta-C) or amorphous carbon (a-C) with very low H content and high sp^3 hybridization, hence of very high hardness, is typically prepared in arc discharges or by laser ablation. Amorphous (tetrahedral) hydrocarbon materials (a-C:H, ta-C:H) with a relatively high content of H result from PECVD-like deposition processes in hydrocarbon discharges.

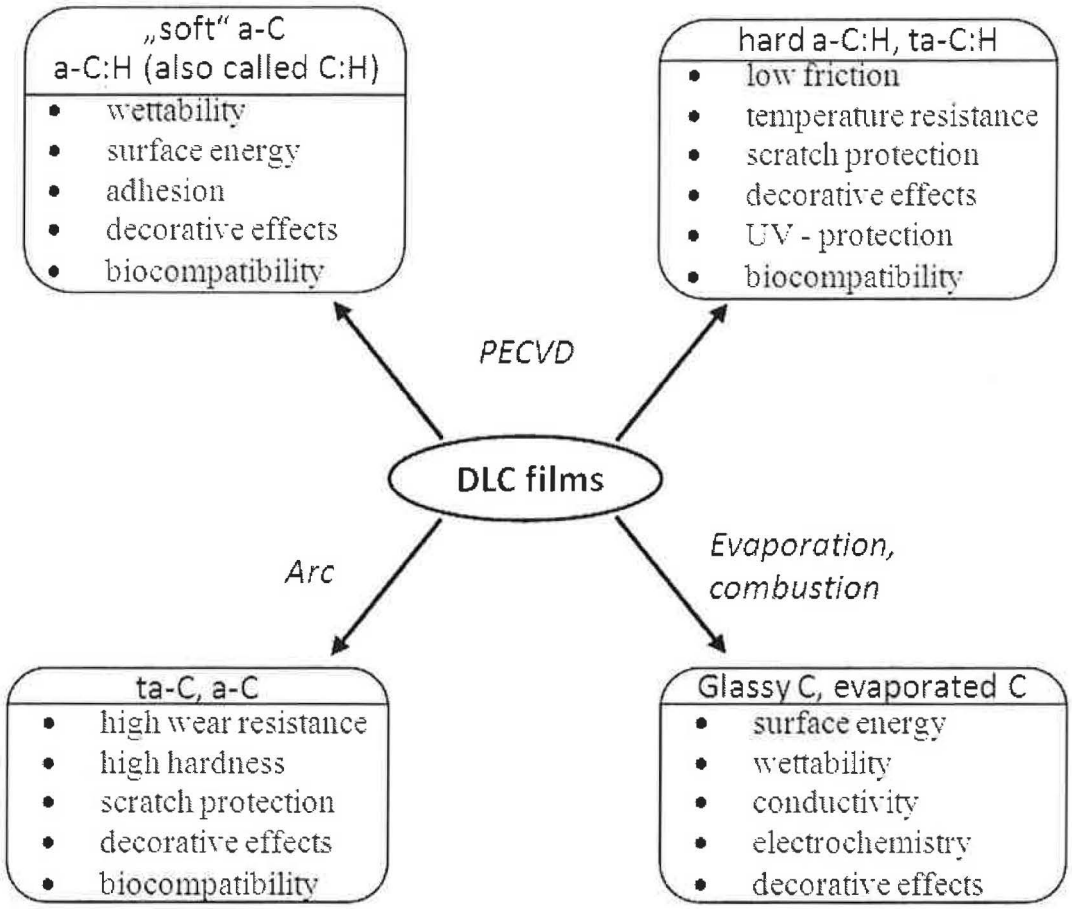

Fig. 1-4 Properties, applications, and techniques used to deposit various DLC films [14]

Table 1-1 Some properties of various carbonaceous films, after [15, 16]

Films structure	Density (g/cm³)	Hardness (GPa)	sp^3 (%)	H (at.%)	Conductivity (Ω·cm)
graphite	2.27		0	0	10^{-4}
glassy C	1.3-1.6	2-3	~0	~0	10^{-3} - 10^{-2}
evaporated C	1.9-2.0	2-5	<5	<5	
sputtered C, a-C	2.2-2.6	10	5-10	<5	$>10^{10}$
soft a-C:H	0.9-1.2	<5	50-80	50-60	10^{6}-10^{14}
hard a-C:H	1.6-2.0	10-35	40-60	30-50	10^{6}-10^{14}
ta-C:H	2.0-2.9	30-60	<75	~ 30	10^{6}-10^{14}
diamond	3.52	100	100	0	$>10^{16}$

1.2.2 Hard amorphous carbon films

Hard plasma polymer films were first prepared by König and Helwig [17] who used a DC glow discharge operated in benzene and grew the films on the anode. They characterized the films by IR spectroscopy [18]. The first a-C:H films were found by Schmellenmeier [19]. Review on these early stages of carbonaceous films was published by Pagnia [20].

Low temperature plasma deposition using a DC glow discharge in a hydrocarbon gas was suggested in order to grow the carbonaceous film on the ion bombarded cathode [21].

Actually, the first economically feasible deposition process was invented in 1976 by L. Holland [22] who suggested using an RF glow discharge in a hydrocarbon gas. He deposited a carbonaceous films on the negatively biased probe capacitively coupled to a RF power supply. In later publication Nyaiesh and Holland [23] related the growth of the film to the RF power input per unit area of the receiver (RF excitation electrode) and unit gas pressure (for methane) and claimed that the soft polymer was deposited from zero up to 5 $W \cdot cm^{-2} \cdot Torr^{-1}$. From this value up to 9 $W \cdot cm^{-2} \cdot Torr^{-1}$, hard plasma polymers were obtained while the temperature of the growing film did not exceed 175 °C. In the range from 10 to 23 $W \cdot cm^{-2} \cdot Torr^{-1}$, a-C:H film was grown. Above 23 Wcm-2Torr-1, graphite like film was created.

It was shown by Biederman et al. [24] that in the case of an RF (20 MHz) discharge operated in benzene at 2 Pa, soft plasma polymer films were deposited for bias values within 0 and -100 V. For bias values ranging from -100 V to -180 V (-200 V), hard plasma polymer films were obtained and for even more increased negative bias values, a-C:H films were grown.

Further studies by Wagner et al. [25] investigated in detail the deposition process using benzene at a pressure of 3 Pa and a DC negative bias $V^B = -1000$ V. Process parameters such as bias voltage, V_B, and pressure, P, determine the a-C:H films structure and their physical properties [26]. Bubenzer et al. [27], in the earlier work where they used 2.3 MHz power, stressed the importance of the energy of positive ions bombarding the growing deposit.

These authors therefore conclude that below $V_B = 100$ V, the films are "polymerlike", transparent and soft. They contain more than 40 at.% H. At biases above 300 V, the films are dense, hard and strongly crosslinked. They noted a transition region between the two types of carbonaceous films (soft plasma polymer and a-C:H) for V_B of 100 – 300 V that correspond to the average ion impact energies between 40 and 120 eV. In this region (more likely between 100 and 200 eV), so called hard plasma polymers are deposited. At higher bias ($V_B = 400$ V) there is no dependence. However, deposition rate ($V_B = 400$ V, pressure P = 3 Pa) decreases from 85 nm/min for benzene to 25 nm/min for n-hexane, and to 5 nm/min for methane [26].

Energetic positive ions Ar^+ (or even hydrocarbon positive ions $C_xH_y^+$) impact on the growing plasma polymer and break C-H bonds. They also push carbon atoms closer together thus creating tetrahedral arrangement. Free radicals on the surface are the sites of further plasma polymerization process. When hydrocarbon ions are used this leads at moderate energies to enormous increase of deposition rate (AGM model d'Agostino [28]). However, when more argon ions than hydrocarbons bombard the growing film – the densification and compaction processes prevail. As a result the amorphous a-C:H material appears. Its structure can be qualitatively described according to Smith [29]: on the short distance sp^3 bound carbon exists and it is continued by sp^2 carbon and polymeric C:H structures – with voids among all of these. Such network is under high compressive stress which builds up with the increasing thickness. When adhesion to the substrate is overcome which is for glass at ~ 200 nm, then a-C:H peels off. However, the adhesion on Si and Ge is very good because of the carbide interface layer that is created. Therefore, a-C:H films were successfully used as optical coatings for the IR region of light. They were also used as hard, non-abrasive (low friction) coatings on various materials, including polymers [23].

In case of unbalanced magnetron with graphite target energy of bombarding positive ions to the substrate is much lower and therefore C:H hard plasma polymer is created. A little of carbon is sputtered from the target; he nce, plasma polymerization process in the plasma volume and mainly on the substrate takes place assisted with the mild positive energetic (hence, light current) bombardment.

1.2.3 Composite metal/hydrocarbon based coatings (Me/C:H) from DC magnetron sputtering

The metal/plasma polymer films appeared in the seventies as a new class of composite thin films [30-32]. In the following years, a number of studies devoted to this topic increased as can be seen from a number of reviews e.g. [2, 33-35]. One should note that the first composite metal/"organic films" were produced by vacuum co-evaporation [36, 37]. Simultaneously metal/inorganic dielectric (cermets) prepared by vacuum co-evaporation and co-sputtering were investigated and these studies layed down some basic concepts for the film property explanations, including theoretical models [38].

Both cylindrical and planar magnetrons were used by Harding and Craig [39, 40] who prepared Fe/C:H composite films by "reactive sputtering" of stainless steel in an Ar/C_2H_2 plasma. Fast neutrals were considered to be responsible for deposition of C:H (hard plasma

polymer instead of usual hydrocarbon (soft) plasma polymer films. At the same time, Sikkens [41, 42] reactively sputtered, in a simple DC diode sputtering arrangement, Ni in an Ar/CH_4 mixture. Weissmantel [43] reported composite films prepared by planar magnetron co-sputtering of graphite and Sn and Ti. Deposits prepared in these studies were claimed to be metal/hard carbonaceous films. Additional metals were incorporated, such as Ta and W [44-46]. The deposition process of metal/C:H composite films was improved after the unbalanced mode of planar magnetron operation was discovered [47]. An escaping beam of plasma from the near target region induces a negative bias (floating potential) from -10 to -70 V against ground of the isolated substrate. This bias attracts mild positive ion bombardment. Biederman et al. [48, 49] prepared, in this way, composite metal/C:H films from a composite metal graphite target using a mixture of Ar and propane. Gold, molybdenum and some others were attempted but mostly silver was investigated [49]. The closed field unbalanced magnetron sputtering arrangement was used for the deposition of graded and multilayered Ti:C-H/TiC thin film systems for wear-resistant application [50]. An unbalanced planar magnetron, equipped with various targets (Ag, Ni, Mo and Ge) in a DC discharge and operated in Ar/n-hexane working gas mixture was used for the deposition of Ag/C:H [51], Ni/C:H [52], Mo/C:H [53], Ge/C:H [54] and Cu/C:H was examined [55]. In recent years, great attention has been paid to Ti/C:H [14, 56-63] because of the tribological applications, optical application (selective absorber) [64] and biomedical applications.

1.2.4 Ti/hydrocarbon coatings

Carbides of transition elements such as titanium carbide are refractive ceramic materials with several remarkable properties such as high melting point, metallic conductivity, and high hardness. Due to their high hardness, such coatings are widely used for coating of cutting and grinding tools. TiC has a high electric conductivity which is almost independent of temperature. Hence it meets the requirements for materials used as metallic interconnects of integrated circuits, which must perform in wide temperature ranges. Because of a low work function, these materials are also potential candidates for electron injecting electrodes in OLED displays. Since these materials are non-stoichiometric and remain in NaCl crystal structures with as many as 50 % carbon vacancies, deposition with variable carbon/metal ratio allow to further control the electrical properties. Titanium, which can easily reduce surface oxides (e.g., native silicon oxide $SiOx$) through formation of TiO_2, efficiently achieves good adhesion on many substrate materials. By deposition of tailored Ti → Ti-C:H → a-C:H film

systems, the covalent bonding can be further propagated over the TiC phase to the a-C:H surface of the film system. Such approach represents an optimal solution to the problem of weak adhesion of carbonaceous films. However, high temperatures (above 1600 °C) are needed for conventional production of TiC compounds from solution [65] or using CVD techniques (> 800 °C). That is incompatible with many substrates and most conceivable microtechnology applications. Plasma-assisted techniques allow the deposition of these films at low-to-moderate temperatures under non-equilibrium conditions. Most typical deposition techniques involve arc deposition [66], dense plasma focus device [67], laser ablation of TiC targets [68], combined eventually with evaporation or magnetron sputtering [69]. Sputtering, combined with PECVD from hydrocarbon vapours can be deployed for the fabrication of various composite Ti / TiC / Ti-C:H / a-C:H coatings [58, 70-73]. Numerous studies within the last decade revealed interesting mechanical and tribological properties of such composites [61, 62, 70, 72, 74]. For example, composite Ti-C:H films can achieve hardness of up to 35 GPa while coefficients of friction are lower than 0.3 for Ti concentrations below 40 at.% [62]. The titanium-containing composites seem to have also favorable biocompatible behavior; *in-vitro* studies point out that the presence of Ti on a a-C:H matrix promotes cellular reactions of bone marrow cells, enhancing bone ingrowth through osteoblast differentiation while reducing bone resorption through osteoblast-like activity inhibition (for more details see next chapter). Therefore, Ti containing hard coatings has been recently proposed for bone implants or dental surgery. Due to the combination of good tribological and mechanical properties, the field of microelectromechanical systems (MEMS) is a promising application area, where complete moving parts can be manufactured by patterning hard TiC layers [68]. Providing such parts with a hydrocarbon or Ti-C:H surface coating could give an optimal material for miniaturized bio-implants.

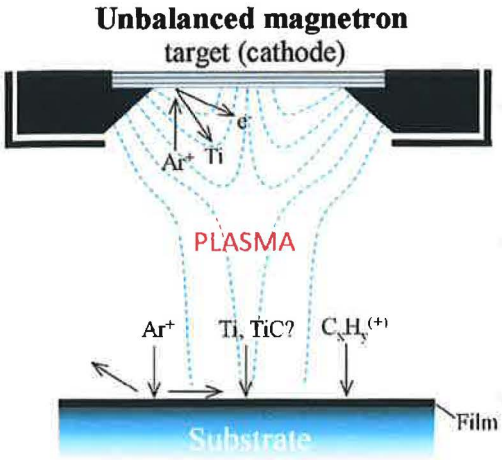

Process involved	
Ar gas only	**n-hexane gas added**
Ti sputtering, secondary electron emission	target poisoning by a-C:H (and TiC ?) film formation, sputtering of coverage film
excitation, ionization, optical emission	reactive gas dissociation, ion & radical production, (bulk chemical reactions ?)
Ti deposition, ion bombardment: removal of weakly bonded species and structural changes	surface chemistry: a-C:H and TiC film growth, creation of new reaction sites, film restructuring

Fig. 1-5 Overview of the important reactions at the target, in the plasma bulk and at the substrate involved in the deposition process in case of clean Ar plasma and after the introduction of the reactive gas

An overview of the most important processes involved in unbalanced magnetron sputter deposition of Ti for different discharge regions in presence of monomers such as hydrocarbons is given in Fig. 1-5. The process hysteresis effect and the dependence on target history are well known phenomena of conventional reactive sputtering. This reactive process is, to a certain extent, similar to conventional reactive sputtering. However, in this particular case, monomer gases typically do not necessarily have to chemically react with the target material but rather cause deposition of a hydrocarbon poisoning films (coverage) on the top of target surface. These films help to control the amount of the sputtered target material. In the unbalanced magnetron configuration, the film growth at the substrate results prevalently from the following two processes: (1) sputtering of the original target material and (2) plasma polymerization processes (or PECVD deposition) of the hydrocarbon component. It is now generally accepted that the mechanism of plasma polymerization in low pressure plasma is initiated in the plasma volume [2, 75]. In the unbalanced magnetron configuration, the reactants participating in the polymerization are generated mainly in the plasma beam. Collisions of electrons and ions with n-hexane, mainly by an electron impact fragmentate the molecules of the monomer and create free radicals, molecular ions, etc. Additionally, these reactions affect quite significantly the electron distribution function since their threshold energies are often lower than those of the inelastic Ar collisions. The film growth proceeds on the surface while the ion bombardment and the substrate temperature play an important role in the growth process. Though the pressure is relatively low, gas phase radical and ionic reactions might play a role for the production of the reactants in the plasma volume.

1.3 Plasma polymerization in biomedicine

Bio-integration is the ideal outcome expected of an artificial implant. This implies that the phenomena that occur at the interface between the implant and host tissues do not induce any deleterious effects such as chronic inflammatory response or formation of unusual tissues. Hence, it is of paramount importance to design biomaterials used in implants with the best surface properties. Meanwhile, these biomaterials must possess bulk properties that meet other requirements, especially mechanical properties in order to function properly in a bio-environment. As it is quite difficult to design biomaterials fulfilling both needs, a common approach is to fabricate biomaterials with adequate bulk properties followed by a special treatment to enhance the surface properties. In this way, it allows one to make ideal biomaterials with surface attributes that are decoupled from the bulk properties. Furthermore, the surface properties can be selectively modified to enhance the performance of the biomaterials. For instance, by altering the surface functionality using thin film deposition, the optimal surface, chemical, and physical properties can be attained [76]. Hence, surface modification of biomaterials is becoming an increasingly popular method to improve device multifunctionality, tribological and mechanical properties, as well as biocompatibility of artificial devices while obviating the needs for large expenses and long time to develop brand new materials. It has become one of the key methods in biomaterials engineering. Usually more than one approach can satisfy the biomaterials requirements, and the ultimate selection must take into account the process reliability, reproducibility, and products yield [77].

A plasma which can be regarded as the fourth state of matter is composed of highly excited atomic, molecular, ionic, and radical species. It is typically obtained when gases are excited into energetic states by radio frequency (r.f.), microwave, or electrons from a hot filament discharge. Plasma is a highly unusual and reactive chemical environment in which many plasma-surface reactions occur. The high-density of ionized and excited species in the plasma can change the surface properties of normally inert materials such as ceramics. Plasma-based techniques combining the advantages of conventional plasma and ion beam technologies are effective methods for medical implants with complex shapes. In particular, modification of the surface energetics of the materials can improve the adhesion strength, surface and coating properties, and biocompatibility, just to name a few [78]. Plasma-based techniques offer the following advantages with regard to biomaterials engineering.

1. The benefits of plasma processing arise from the good understanding of plasma physics and chemistry learned in other fields such as microelectronics, for example, plasma homogeneity and effects of non-uniform plasma on the substrate surface [79].
2. Plasma engineering is usually reliable, reproducible, non-line-of-sight, relatively inexpensive, and applicable to different sample geometries as well as different materials such as metals, polymers, ceramics, and composite [77, 80-82]. Plasma processes can be monitored quite accurately using in situ plasma diagnostic devices.
3. Plasma treatment can result in changes of a variety of surface characteristics, for example, chemical, tribological, electrical, optical, biological, and mechanical. Proper applications yield dense and pinhole free coatings with excellent interfacial bonds due to the graded nature of the interface [83].
4. Plasma processing can provide sterile surfaces and can be scaled up to industrial production relatively easily. On the contrary, the flexibility of non-plasma techniques for different substrate materials is smaller [84].
5. Plasma techniques are compatible with masking techniques to enable surface patterning [85, 86], a process that is commonly used in the microelectronics industry.

As a result, plasma-surface modification (PSM) as an economical and effective materials processing technique is gaining popularity in the biomedical field. It is possible to change in continuum the chemical composition and properties such as wettability, metal adhesion, dyeability, refractive index, hardness, chemical inertness, lubricity, and biocompatibility of materials surfaces. In the biomedical context, ''good biocompatibility'' refers to that a prosthesis or biomaterial device is non-toxic, does not induce deleterious reactions from the bio-medium, performs properly all the functions they have been designed for, and has a reasonable lifetime. The application of plasma based techniques is quite diverse, and examples of applications include cleaning/sterilization, coating or depositing, and implantation modification of surface chemistry of a substrate. Orthopedic prostheses are made harder and more wear resistant by ion implantation into the articulating surfaces. Orthodontic appliances, surgical instruments, and venous catheters, are treated to improve friction, fretting resistance and biocompatibility. Orthopedic hip and dental implants need bone adhesion control on the Ti alloy surface by Ca. Ion implantation, and artificial blood vessels require endothelial cell adhesion control on polymeric surface by ion implantation for non-thrombogenicity [87]. Table 1-2 lists some of the more common research areas and applications of plasma treatment

in biomaterials [88] and Table 1-3 shows the advantages of plasma deposited films in biomaterial

Table 1-2 Common research areas and applications of plasma treatment in biomaterials engineering

Blood-compatible surfaces	Vascular grafts, catheters, stents, heart-valves, membranes (e.g. for hemodialysis), filters (e.g. for blood cell separation), biomolecules immobilized on surfaces
Non-fouling surfaces	Intraoculars (IOLs), contact lenses, wound healing, catheters, biosensors
Tissue engineering and cell culture	Cell growth, antibody production, essays, vascular grafts
Sterilization of surgical tools and devices	Cutting tools of surgeon, tweezers
Biosensors	Biomolecules immobilized on surfaces
Barriers coatings	Drug-release, gas-exchange membranes, device protection, corrosion protection, reduction of leaches (e.g. additives, catalysts, plasticizers, etc.)

Table 1-3 Advantages of plasma-deposited films in biomaterials applications

Easy preparation
Unique film chemistry
Coated on unique substrates with good adhesion
Conformal and pin-hole free films
Excellent permeation barriers with low level of leachables
Sterile upon preparation

applications [76]. More information can be found in the article of Ratner et al [89, 90].

Chapter 2 Experimental

Experimental

2.1 Deposition systems

2.1.1 A reactor for preparation of nanocomposite Ti/hydrocarbon plasma polymer films

The typical operating pressure of magnetron sputter sources lays around 1 Pa (see section 2.2 for detailed magnetron description). At this pressure, current densities still sufficient for efficient sputtering of the target material and cleaning of poisoning films can be achieved while the sputtered species are almost collisionlessly transported to the substrate over distance of the order of few cm. Because the operating pressure of 1 Pa is five orders of magnitude lower than the atmospheric pressure, it is clear that a vacuum system becomes the central part of the experimental setup design.

Compared to the base pressure of most high-vacuum pumps, the required operating pressure does not seem to put much demand on the pumping system at the first sight. However, when highly reactive materials like Ti are sputtered, the situation becomes more critical. If the residual pressure of the contaminants, e.g. the water vapor in the vacuum chamber is high compared to the flux of sputtered particles, these can react with each other and an oxide film instead of metallic film is deposited. Within this work a process for the deposition of films of total thickness of less than 1 μm had to be developed.

Ti/hydrocarbon plasma polymer films were deposited using an unbalanced magnetron (120 mm in diameter) designed in our laboratory with Ti target (75 mm in diameter) operated in the DC mode in a working gas mixture of Ar (of 99.99% purity)/n-hexane(Aldrich, hexane 99+%, $CH_3(CH_2)_4CH_3$). The arrangement of the deposition system is shown in Fig. 2-1. The vacuum chamber was pumped by rotary and diffusion pumps to the base pressure better than $5 \cdot 10^{-4}$ Pa. The depositions were performed at a working pressure of 2 Pa. The pressure was measured by

MKS Baratron 626 absolute pressure transducer. The flow rate of argon was automatically adjusted by a flow-controller (MKS instruments) and set to the value of 19 sccm. The flow rate of n-hexane was manually controlled by a needle-valve to the values of 0.1 – 6.6 sccm. The depositions in pure Ar and n-hexane were also performed. The substrate holder was placed opposite to the magnetron at a distance of 50 mm from the target. A direct current generator MDX 1.5K (Advanced Energy) powered the magnetron in a constant current mode (0.2 A). The target surface was cleaned with abrasive paper and alcohol before and after of each experiment, except the experiments in pure Ar.

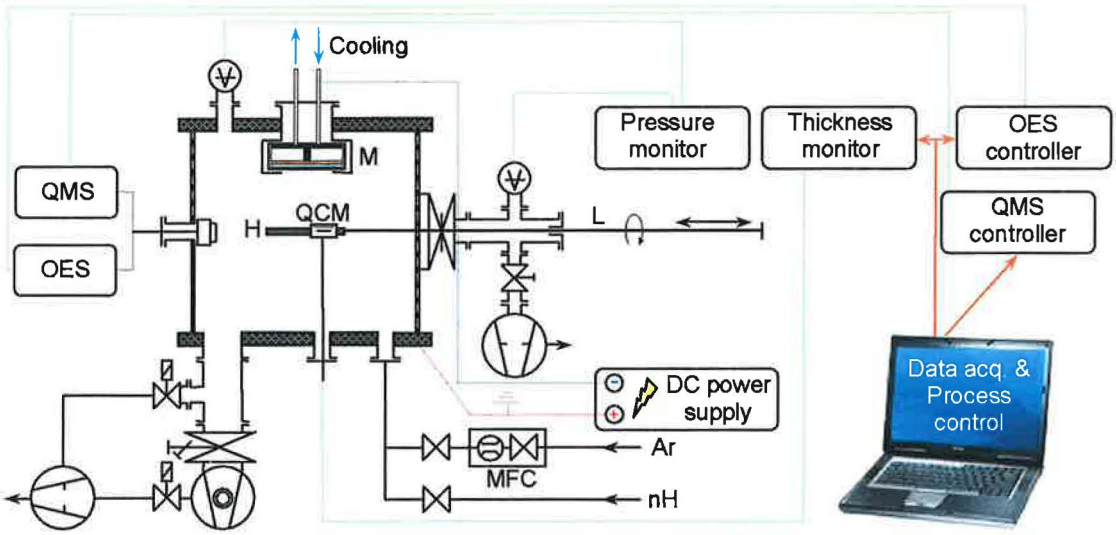

Fig. 2-1 Schematic diagram of the experimental setup for titanium deposition (M magnetron, H substrate holder, QCM - Quartz Crystal Microbalance, L load-lock, OES – Optical Emission Spectroscopy, MFC - mass flow controllers)

2.1.2 Reactor for polypropylene surface oxidation in low pressure DC discharge operated in oxygen and water vapor.

PP film treatment by DC low-pressure discharge was carried out in a homemade flow reactor in Ivanovo State University of Chemistry and Technology (Fig. 2-2) equipped with cylindrical glass tube having internal diameter of 3 cm. Three hollow cylinder electrodes (aluminum) 2.9 cm in diameter were used for discharge excitation. Changing the order of the electrodes connection enabled treating the samples both in positive column and in flowing discharge afterglow. Polymer sample was placed as a ring on an inner thermally stabilized reactor wall. The sample temperature was maintained at 343 K and its area was 18.8 cm^2. Freshly cut

samples were used for each experiment. Flow rate was 50 cm/s under normal conditions. After placing the sample in the reactor, the reactor was first pumped down until 0.1 Pa pressure. During the treatment, the oxygen and water vapor pressure was 100 Pa and discharge current was 80 mA. Degassed double-distilled water was used as a source of water vapor.

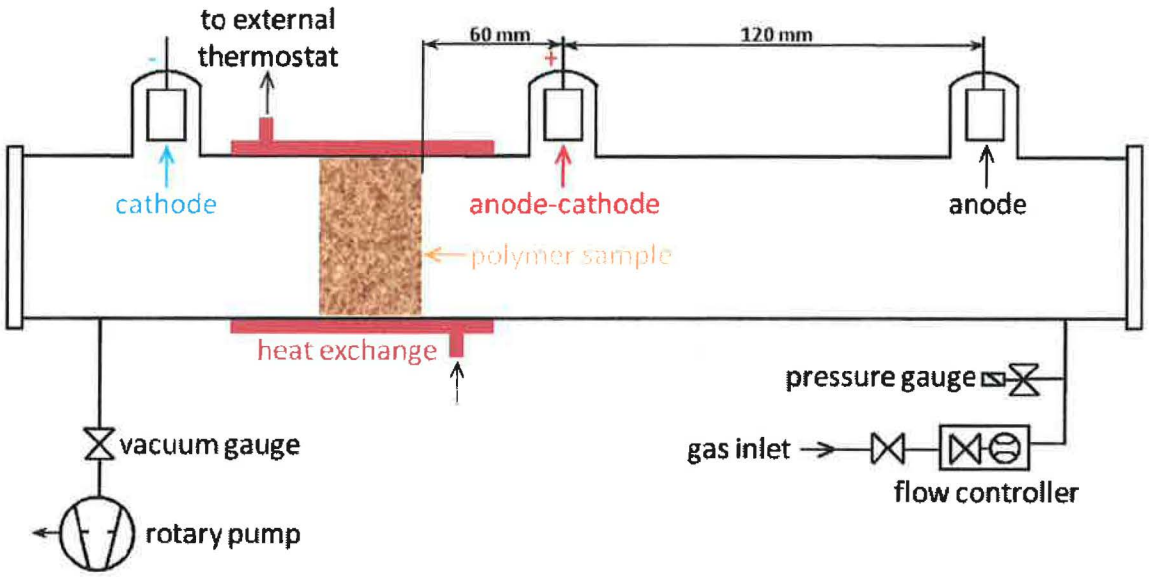

Fig. 2-2 Schematic diagram of the experimental setup for polypropylene surface oxidation

2.2 Unbalanced magnetron

A prototype of the unbalanced magnetron used in this work corresponds to the type II according to the classification given by Window and Savvides in [91] and was constructed in our laboratory. The cross-section of the prototype construction along with the shape of the magnetic field, plasma and the substrate position is shown in Fig. 2-3. The $SrO{\cdot}6Fe_2O_3$ magnets with $B_r = 0.3$ T (1) are mounted as the outer part of the magnetic circuit as shown in Fig. 2-4.

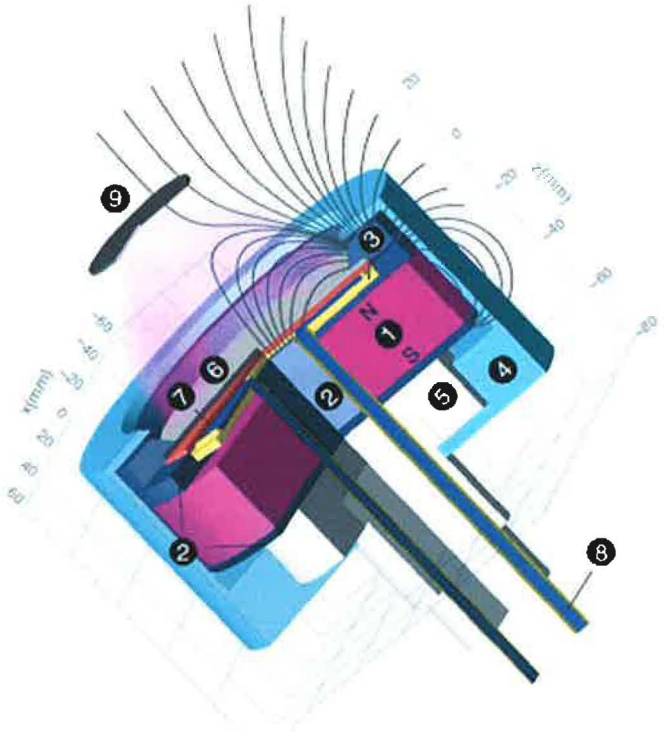

Fig. 2-3 Cross-section of the unbalanced magnetron: 1 - magnets, 2 - iron parts, 3 - coolant channel, 4 - shielding (ground), 5 - insulator, 6 - target, 7 - copper membrane, 8 - coolant channel, 9 - substrate position

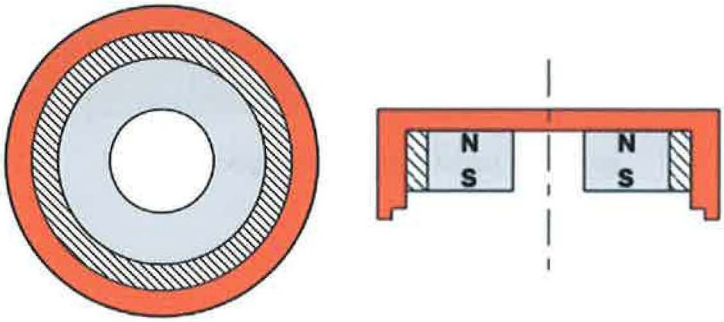

Fig. 2-4 Scheme of magnetic circuit in our unbalance magnetron

The sputter target (6), 80 mm in diameter, is mounted using the ring-shaped mechanical target clamp (2) and connected to the cathode of the power supply over the copper tubing of the

cooling circuit (8). As more than 90 % of the magnetron operating power is transformed into heat in the sputter process at the target surface and since the magnetron body is located in vacuum environment, a cooling system providing sufficient heat transfer from the target becomes an important part of the magnetron design. In our case, power of the order of few 100 W must be efficiently transported away in order to protect magnetron from mechanical deformations as well as to protect the magnets from the demagnetization process. Low temperatures are also desired to prevent excessive degassing of hidden magnetron surfaces and magnets. Therefore water cooling with water channel (3, 8) behind the target is used. To avoid breakthrough of water into the vacuum system, the target is cooled indirectly over a copper membrane (7). In contrast to the original prototype, where a copper plate is sealed against the water circuit by an O-ring, a copper membrane (6) hard-soldered directly to the water channel (3) is used. This construction provides more robustness, reliability, and very efficient cooling because the deformation of the membrane under water pressure (6 – 8 bar) guarantees good thermal contact with the target. The magnetron body is enclosed in grounded shielding made of aluminum and insulated by a Teflon spacer (5) from the cathode potential. On the top of the spacer, Teflon flange that serves as vacuum and electrical feedthrough is attached (Fig. 2-5). Vacuum sealing of the copper tubings is done using O-rings.

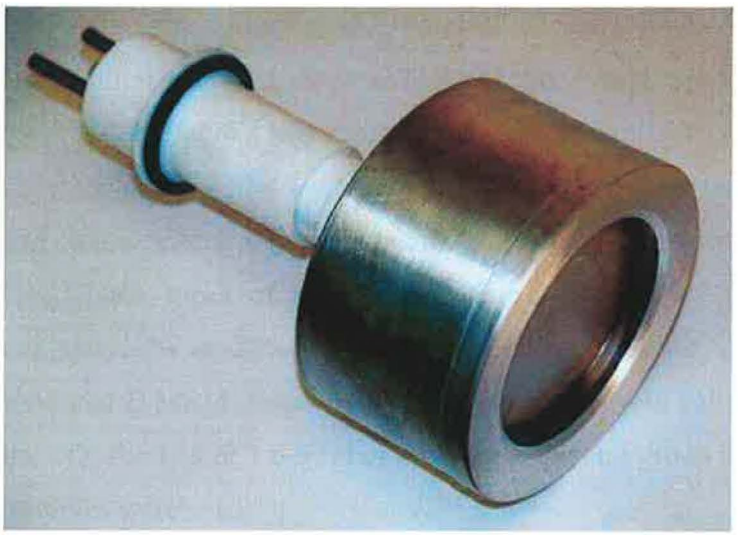

Fig. 2-5 Photograph of the unbalanced magnetron

2.3 Materials

Hexane 99+% purity ($CH_3(CH_2)_4CH_3$) used for preparation of Ti/hydrocarbon films was purchased in Sigma-Aldrich company.

Microscopic glass slides (Marienfeld, Germany, 76x26x1 mm) were used for water contact angle measurements, biological tests.

Silicon wafers (111) used for XPS, RBS/ERDA and AFM were purchased in "On Semiconductor Czech Republic, a.s.".

S160 carbon films 200 mesh Cu (50) used for TEM diagnostics were purchased in "Agar Scientific, UK".

Glass slides coated with hydrocarbon plasma polymer films sputtered in pure n-hexane (less than 1 atomic % of Ti) or pure argon (20 atomic % of Ti) or uncoated slides were cut into pieces of the size of 8 x 8 mm and sterilized by germicide UV irradiation for 60 min on each side. The samples were then inserted into Nunclon Multidishes (NUNC, Denmark, 24 wells, diameter 15 mm) and seeded either with human osteoblast-like cells of the line MG 63 (European Collection of Cell Cultures, Salisbury, UK) or bovine pulmonary artery endothelial cells of the line CPAE (ATCC CCL 209, Rockville, MA, U.S.A.). Each dish contained 10 000 cells per cm^2 and 1.5 ml of the culture media. For MG 63 cells, Dulbecco-modified Eagle Minimum Essential Medium (DMEM, Sigma, U.S.A., Cat. No. D5648) was used, while CPAE cells were incubated in Eagle`s Minimum Essential Medium (E-MEM, Gibco, Cat. No. 41500-067) supplemented with 2mM L-glutamine and Earle`s BSS with 1.5g/L sodium bicarbonate, 0.1 mM non-essential amino acids and 1 mM sodium pyruvate (all chemicals from Sigma, U.S.A.). Both types of medium contained 40μg/ml of gentamycin (LEK, Ljubljana, Slovenia) and 10% or 20% of fetal bovine serum (Sebac GmbH, Aidenbach, Germany) for DMEM and E-MEM, respectively. The cells then were cultured at 37°C in air atmosphere with 5% CO_2 for 1, 3 or 7 days. For each experimental group and time interval, 6 to 10 independent samples were used.

Commercial isotactic PP of 60 μm thicknesses was used for study of polypropylene surface oxidation in DC low pressure oxygen and water vapor discharges and in flowing afterglow of water vapor discharge.

2.4 Diagnostic instruments

This section describes the diagnostics instruments installed permanently at the main reactor chamber and used routinely throughout the experimental work and several other instruments which were used *ex-situ*.

2.4.1 Optical Emission Spectroscopy (OES)

In-situ diagnostics of plasma polymerization process was performed by optical emission spectroscopy (OES). The self-built OES apparatus consists of an optical fiber, ARC SpectraPro-300i monochromator with grid and Hamamatsu photomultiplier R928 [92]. The optical fiber was connected to the reactor co-axially and detected emission through a quartz window.

2.4.2 Thickness measurements

The thickness of plasma polymers deposited on glass was determined using surfometer (Planer Industrial, SF 200) via the scratch test. In this method, several scratches are made on the sample and then the tip of surfometer scans the surface profile in direction perpendicular to the scratches.

For the films with thickness less than 100 nm, the sensitivity of the surfometer was insufficient and atomic force microscopy (AFM, Quesant, Q-Scope 350) was used instead for the scratch test. The accuracy of the thickness measurements by both surfometer and AFM was estimated to be ~20%.

2.4.3 Mass spectroscopy

Monopole mass-spectrometer MX-7304 (Russia) was used for analysis of polypropylene treatment in plasma and in afterglow (Section 3.2.3). The ion source was pumped by differential getter-ion pump NORD 250 (Russia) to the pressure better then 10^{-6} Torr. Taking of a sample was performed through the diaphragm, which was placed on a distance of 10 mm from the sample in the direction of gas flowing (Fig. 2-2).

2.4.4 Scanning probe microscopy (SPM)

This analysis was done at Nagoya University in Japan. The Ti/hydrocarbon films were imaged in air at a relative humidity of 35-40% by an SPM (SPA-300HV+SPI-3800N, Seiko Instruments Inc) in Dynamic Force (DFM), Kelvin Force (KFM) and Visco-Elastic Atomic Force (VE-AFM) modes. A limited number of the AFM force-distance measurements were conducted under 10^{-3} Pa vacuum. The DFM, KFM, VE-AFM and adhesion force measurements were conducted by using a gold-coated silicon cantilever with a spring constant of 1.8 N/m and a resonance frequency (f_r) of 23-25 kHz. The scan rate was 1 Hz and the resolution was 256 data points for all the measurements. The topography measurements were performed in the DFM mode analogous to the tapping mode.

The KFM mode is a two-pass technique. In the first pass, the tip is scanned over the surface under conventional DFM mode and topography is acquired. Then the tip is retraced over the same scan line but it is no longer driven by mechanical oscillations of the piezo. Instead, the sinusoidal voltage is applied on the tip. If the surface bears a local electric charge, the resulting capacitive force between the tip and the surface leads to cantilever oscillations. These are suppressed by the feedback circuit adjusting the tip voltage which, in this case, is equal to surface potential. In this work, an alternating current voltage of 5 V at a frequency (f_r-2 kHz) was applied between the probe and sample.

The VE-AFM measurements combine two-dimensional scanning at constant tip-surface force with the sinusoidal modulation of vertical position of the sample. This results in an indentation of the tip against the sample which depends on stiffness of the latter. The softer areas are indented deeper and induce less cantilever deflection. Therefore, the lower and higher cantilever amplitude measured by a position sensitive detector is indicative of softer and harder areas, respectively. The response of strain to oscillatory stress depends on viscoelastic properties of material. Purely elastic materials have in-phase strain-stress relation, whereas in purely viscous materials there is a 90 degree phase lag between stress and strain. Viscoelastic materials have both elastic and viscous properties and exhibit stress-strain phase lag somewhere in between 0 and 90 degrees. The complex dynamic modulus is written as follows.

$$G = G' + iG'' \tag{2.2}$$

In this equation G' and G'' are storage and loss modules, respectively. G' characterizes the stored energy and is related to elastic contribution. G'' represents dissipated energy and is related to viscous contribution. Both are expressed as is shown in next two equations.

$$G'' = \frac{\sigma_0}{\varepsilon_0}\cos\delta \tag{2.3}$$

$$G'' = \frac{\sigma_0}{\varepsilon_0} \sin \delta \qquad 2.4$$

In last two equations σ_0, ε_0 and δ are amplitude of stress, amplitude of strain and phase lag between them, respectively. The SPM used in this work allowed mapping real and imaginary contributions of cantilever amplitude in a form of $A_0 \cdot cos\delta$ and $A_0 \cdot sin\delta$. Consequently, $A_0 \cdot cos\delta$ and $A_0 \cdot sin\delta$ were related to elasticity and viscosity of the sample, respectively. The cantilever was sinusoidally modulated with amplitude of 5 nm and frequency of 5 kHz.

The adhesion forces between the Ti/hydrocarbon films and silicon were assessed by taking the force-distance curves in air and in vacuum. For this purpose, the cantilevers with the silicon tips were consistently cleaned with acetone, ethanol and water, and dried under gentle nitrogen flow. Furthermore, a series of experiments was done with fibrinogen covered tips.

The performance of implants in contact with blood depends on their ability to prevent thrombus formation. It is generally recognized that biological reactions between a tissue and artificial implants are mediated by protein adsorption. Fibrinogen is a blood plasma protein playing an important role in surface induced blood clot formation (thrombosis) through the polymerization to fibrin. Hence, a research on interaction of fibrinogen with materials intended as implants is relevant.

Fibrinogen was unspecifically adsorbed by incubating the clean silicon cantilever in solution of fibrinogen in PBS. Multiple rinsing with PBS and water was applied thereafter to remove an excess of the protein.

2.4.5 Rutherford back-scattering spectrometry (RBS) and elastic recoil detection (ERD)

The elemental composition of the Ti/hydrocarbon plasma polymer films was also determined by Rutherford back-scattering spectrometry (RBS) and elastic recoil detection (ERD) methods using a Van de Graaf accelerator. The α-particles and protons at kinetic energies between 1 and 3.5 MeV have been elastically scattered by the sample. Since the energy of the reflected species by α -particles strongly depends on the mass of the reflecting sample atoms, the mass discrimination is obtained. By counting the α-particles as a function of energy, the number of atoms of each element present can be determined.

Once the sample irradiated with α -particles, light elements (e.g. H) from the sample are scattered in forward directions and can be detected with a Si detector. From the measured energy spectrum of the recoils a concentration depth profile can be calculated.

The elemental content in composite plasma polymer films was measured. The C and O content was measured using the energy of α -particles of 2.75 MeV. RBS spectra were evaluated by computer code GISA 3, whereas ERD spectra by the SIMNRA code, both using cross-section values from SigmaBase.

This analysis was performed in Department of Neutron Physics, Academy of Science of the Czech Republic.

2.4.6 Transmission electron microscopy (TEM)

Transmission electron microscopy observations (TEM) were performed on a JEOL 2000 FX electron microscope with the aim to observe the morphology of Ti/hydrocarbon polymer thin films. Carbon coated 300-mesh copper grid (3mm in diameter) was used as a specimen (S160, Elektronenmikroskopie, Austria). Thickness of the carbon coating is less than 3nm. Thickness of studied films was 50 - 100 nm.

This analysis was performed at Department of Metal Physics, Charles University Czech Republic.

2.4.7 X-ray photoelectron spectroscopy (XPS)

For the XPS study, the ultrahigh vacuum (UHV) system (base pressure about $6 \cdot 10^{-10}$ Pa) was equipped with a multi-channel hemispherical electrostatic analyser (Phobios 100, Specs), a dual (Al/Mg) anode X-ray source and a differentially pumped sputter ion source (XR50, Specs). In this work the Al Kα line (1486.6 eV) was used with the incidence angle of X-ray 45° to the surface plane. The analyser was operated in the retarding-field mode, applying the pass energy of 40 eV for survey scans and 10 eV for all core level data. The XPS peaks were charge referenced to the aliphatic C 1s (C-C, C-H) component at 285.0 eV. XPS peak positions were determined with an accuracy of 0.1 eV. This setup belongs to Department of Macromolecular Physics.

XPS (PHI Quantera SXM, ULVAC-PHI, Monochromatic Al Kα) was also used for the analysis of the surface composition of polypropylene. The photoemission angle was normal to the surface. High-resolution and survey spectra were collected at a pass energy of 80 and 20 eV, respectively. The XPS peaks were charge referenced to the aliphatic C 1s (C-C, C-H) component at 285.0 eV. Analysis on this setup was performed at National Institute for Material Science, Tsukuba, Japan.

2.4.8 Fourier Transform Infra-Red spectroscopy (FTIR)

A spectrophotometer (AVATAR System 360 ESP, Nicolet) equipped with multiple internal reflectance apparatus was used to obtain the ATR-IR spectra of plasma-treated polypropylene surface. ZnSe prism with a refraction coefficient of 2.4 and the number of reflections equal to 12 was used as an internal reflection element. Wavelength range from 4000 to 400 cm^{-1} was scanned 32 times for spectrum integration. The scanning resolution was 2 cm^{-1}. At least 5 samples were used to obtain the average value of optical densities. The optical densities were normalized by dividing them by the value of own vibration band which represented $-CH_2-$ group in the main polymer chain and appeared at 2915 cm^{-1}.

2.4.9 Contact angle measurement and surface energy

The contact angle measurement was performed on the nanocomposite films deposited on glass substrates. The contact angle of water was measured in the static mode when the constant time (30 sec) passed after dropping of water. The value of the contact angle has been estimated from five independent measurements of water drops (about 2 mm in diameter) with a contact angle device (self built) by a sessile drop method at a room temperature (18-20°C).

To determine the surface free energy of treated PP films, the static contact angles were measured at room temperature by the method of reflected light diagram [93, 94]. In this method a reflected light diagram is obtained from the He-Ne laser (λ=638 nm) used as a light source after dropping sessile drops of both distilled water and glycerol on the modified surface. Then, the surface free energies, together with both polar and dispersion components, were calculated on the basis of the Fowke's equation [95].

2.5 Biological tests

2.5.1 Evaluation of cell adhesion, growth and differentiation

Cell adhesion was evaluated by the number of initially adhered cells, cell adhesion area, assembly of focal adhesion plaques and concentration of talin, a component of focal adhesion plaques participating in the process of cell-substrate adhesion by connecting integrin adhesion receptors to actin cytoskeleton.

For the first two criteria, the cells in 1-day- old cultures were washed in phosphate-buffered saline (PBS, Sigma, U.S.A.) fixed with pre-cooled 70% ethanol (-20°C, 5 min) and stained with hematoxylin and eosin (Sigma, St. Louis, MO, USA) according the manufacturer's protocol. Their numbers were estimated by the phase-contrast microscope (Olympus IX 50, Japan) on microphotographs taken with a digital camera Olympus DP 70. The cells were counted in 9 randomly selected fields on each sample. On the microphotographs, the size of the cell-material contact area was also measured using a software Atlas (Tescan S.R.O., Brno, Czech Republic; 25-35 cells in 6 randomly selected areas on each sample). Cells in contacts were excluded from the analysis.

Focal adhesion plaques were visualized by immunofluorescence staining of talin (please see Section 2.5.2), and the concentration of talin was determined semi-quantitatively ELISA per mg of protein in cell homogenates obtained by ultrasonication (please see Section 2.5.3).

Cell proliferation was estimated by the changes in cell number from day 1 to 7 after seeding, demonstrated by the course and shape of growth curves. The hematoxylin-eosin-stained specimens were used for counting cells in the earlier culture intervals (day 1 and 3). In the later interval (day 7), when the cells were confluent or formed multilayered regions, the cells were detached with a trypsin-EDTA solution (Sigma, U.S.A, Cat. N° T4174) in phosphate-buffered saline (PBS), and counted in a Bürker haemocytometer.

Osteogenic differentiation of MG 63 cells was evaluated by the concentration of osteocalcin, a calcium-binding extracellular matrix glycoprotein. Maturation of endothelial cells was estimated by their ability to form confluent cobblestone-like cell layer and by the concentration of von Willebrand factor, a member of the hemocoagulation cascade. Both osteocalcin and von Willebrand factor were visualized by immunofluorescence staining (please see Section 2.5.2), and their concentration was measured semi-quantitatively by ELISA (please see Section 2.5.3).

2.5.2 Immunofluorescence staining of talin, osteocalcin and von Willebrand factor

On day 3 after seeding, the cells were fixed with cold 70% ethanol (-20°C, 5 min), pre-treated with 0.5% bovine serum albumin in PBS containing 0.05% Triton X-100 (Sigma, St. Louis, MO, U.S.A.) for 20 min at room temperature and incubated with primary antibodies listed in (Table 2-1A). As the secondary antibodies, goat anti-mouse or goat anti-rabbit IgG, both conjugated with Alexa Fluor 488 and diluted in PBS, were used after staining with monoclonal and polyclonal antibodies, respectively (Table 2-1B). The cells were mounted in Gel/MountTM (Biomeda Corp., CA, U.S.A.) and evaluated by Olympus IX 50 epifluorescence microscope equipped with a digital camera DP 70 [20, 21].

2.5.3 ELISA of talin, osteocalcin and von Willebrand factor

The cells were seeded onto hydrocarbon plasma polymer films deposited directly on polystyrene Petri dishes (TPP, Switzerland; diameter 3 cm; 10 000 cells/cm^2, 5 ml of the culture media). On day 7 after seeding, the cells were harvested with trypsin-EDTA solution (see above) in PBS for 5 min at 37°C and treated with an Ultrasonic Homogeniser (Bandelin Sonoplus HD 3080, BANDELIN electronic GmbH & Co. KG, Germany). For better exposure of epitopes of talin, the cell homogenates were incubated with 0.1% Triton-X100 (Sigma, St. Louis, MO, U.S.A.) in PBS at 4°C overnight. Protein content was determined by a modified Lowry's method [96, 97]. Aliquots of the homogenates corresponding to 1 - 50 μg of protein were diluted in 50 μl of water and adsorbed on 200 μl wells of a 96-well microtiter plates (Maxisorp, Nunc, Roskilde, Denmark) at 4°C overnight. After washing twice by PBS (100 μl/well), the non-specific binding sites were blocked by 0.02% gelatin in PBS (60 min, 100 μl/well). The primary antibodies listed in (Table 2-1A) were diluted in PBS and applied in the amount of 50 μl/well for 60 min at room temperature. As secondary antibodies, goat anti-mouse and goat anti-rabbit IgG, both conjugated with peroxidase, were used after staining with monoclonal and polyclonal antibodies, respectively (Table 2-1C). Both secondary antibodies were diluted in PBS and applied for 60 min at room temperature (50 μl/well). After double washing in PBS-0.1% Triton X-100 solution, the orthophenylendiamine reaction (Sigma, St. Louis, MO, U.S.A.) was performed using 0.05% H_2O_2 in 0.1M phosphate buffer (pH 6.0, dark place, 100 μl/well). The reaction was stopped after 10 min by 2 M H_2SO_4 (50 μl/well). The absorbance was measured in the Multilabel Counter Wallac Victor^2 1420 (Perkin Elmer Life and Analytical Sciences, Inc., Wellesley, MA, U.S.A.) at a wavelength of 492 nm.

The absorbances obtained in cells grown on argon-sputtered hydrocarbon plasma polymer films containing 20 at.% of Ti were expressed in % of values measured in cell samples taken from the hexane-sputtered films with less than 1 at.% of Ti. For each experimental group, 6 to 8 independent cell samples were evaluated.

Table 2-1 Primary and secondary antibodies used for immunofluorescence (Immf.) and Enzyme-Linked Immunosorbent Assay (ELISA) of adhesion-mediating molecules and markers of differentiation in osteoblast-like MG 63 cells and vascular endothelial CPAE cells

A. Primary antibodies

Antibody against	Developed in, Type	Company, Cat. No.	Dilution	Incubation
Human talin	Mouse, monoclonal	Chemicon Int.[a], MAB3264	Immf.: 1:200 ELISA: 1:500	Immf.: Overnight, 4°C ELISA: 60 min, RT[d]
Human osteocalcin	Rabbit, polyclonal	Chemicon Int.[a], AB1857	Immf.: 1:200 ELISA: 1:500	Immf.: Overnight, 4°C ELISA: 60 min, RT[d]
Human von Willebrand factor	Rabbit, polyclonal	Sigma[b], F 3520	Immf.: 1:200 ELISA: 1:500	Immf.: Overnight, 4°C ELISA: 60 min, RT[d]

B. Secondary antibodies for immunofluorescence

Antibody against	Developed in	Type	Conjugated with	Company, Cat. No.	Dilution	Incubation
Mouse	Goat	F(ab')2 fragment of IgG (H+L)	Alexa Fluor® 488	Molecular Probes[c], A11017	1:400	60 min, RT[d]
Rabbit	Goat	F(ab')2 fragment of IgG (H+L)	Alexa Fluor® 488	Molecular Probes[c], A11070	1:400	60 min, RT[d]

C. Secondary antibodies for ELISA

Antibody against	Developed in	Type	Conjugated with	Company, Cat. No.	Dilution	Incubation
Mouse	Goat	IgG Fab specific	peroxidase	Sigma[b], A3682	1:1000	60 min, RT[d]
Rabbit	Goat	IgG whole molecule	peroxidase	Sigma [b], A0545	1:5000	60 min, RT[d]

[a] Chemicon International Inc., Temecula, CA, U.S.A.; Czech dealer: Scintilla S.R.O., Jihlava, Czech Republic

[b] Sigma, St. Louis, MO, U.S.A.; Czech Dealer: Sigma-Aldrich S.R.O., Prague, Czech Republic

[c] Molecular Probes, Eugene, OR, U.S.A.; Czech dealer: KRD Ltd., Prague, Czech Republic

[d] Room temperature

2.5.4 Statistical analysis

Quantitative results were expressed as means ± S.E.M from 6 - 10 samples for each experimental group. Statistical analyses were performed using SigmaStat (Jandel Corporation). Multiple comparison procedures were made by the One Way Analysis of Variance (ANOVA), Student-Newman-Keuls method. The p values equal to or less than 0.05 were considered significant.

Chapter 3 Results and discussion

Results and discussion

3.1 Nanocomposite Ti/hydrocarbon plasma polymer films

3.1.1 Diagnostics of deposition process

Deposition process is very sensitive to the working gas composition and external process parameters. The investigated deposition process is not stable by itself in the presence of reactive gas at fixed external process parameters. Therefore, diagnostics providing more adequate insight into the internal state of plasma are necessary for a better characterization and active process control. Several diagnostic methods have been previously deployed for the control of reactive sputter processes [98]. Among these, the optical emission spectroscopy (OES) and quartz crystal microbalance (QCM) were considered for the purpose of this work as the best candidates for *in-situ* measurements.

3.1.1.1 Optical Emission Spectroscopy

For the OES diagnostics, the optical spectrometer setup discussed in Section 2.4.1 was used. A typical OES spectrum of the light emitted from the discharge from the racetrack area of the target is shown in Fig. 3-1. The emission lines were assigned with the help of the atomic spectral line database [99]. The Ar gas discharge spectrum is dominated by Ti, Ar, neutrals and Ar + peaks. With an increasing concentration of n-hexane in the discharge, the Ti, Ar, neutrals and Ar + peaks still dominate the spectrum, while their intensities decrease.

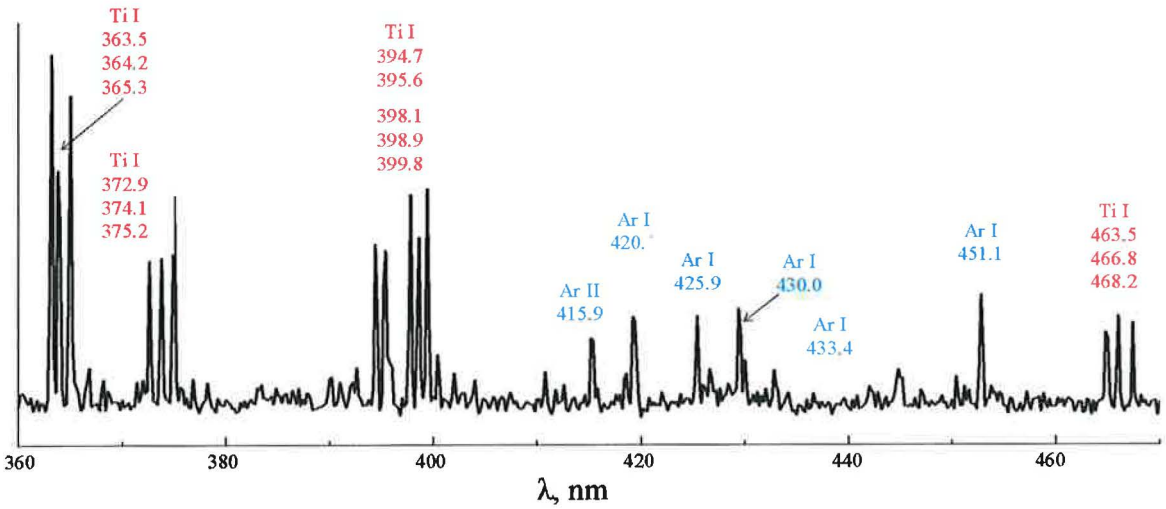

Fig. 3-1 OES spectra acquired in Ar discharge at 0.2 A, monitored Ar and Ti peaks denoted by color

It is well known that the walls and components of the reactor are covered with the layer of water and residual gas molecules in our case when using pumping system with rotary and diffusion pumps (the range of values generally is from $1 \cdot 10^{-3}$ up to $1 \cdot 10^{-4}$ Pa). A number of experiments were performed to obtain optimum parameters to avoid influence of those impurities.

Fig. 3-2 shows the difference in the OES spectra and real photo of the discharge during first minutes after ignition of the discharge. Intensity of lines which correspond to the CO, CH (red line) and OH (black line) groups is decreasing and after 4 minutes intensity of those lines decreases to the noise level. Intensities of Ti (gray region) and Ar (red region) show practically similar growing behavior during the first 2 minutes, but after 3 minutes they stabilize and remain the same up to the end of the experiment.

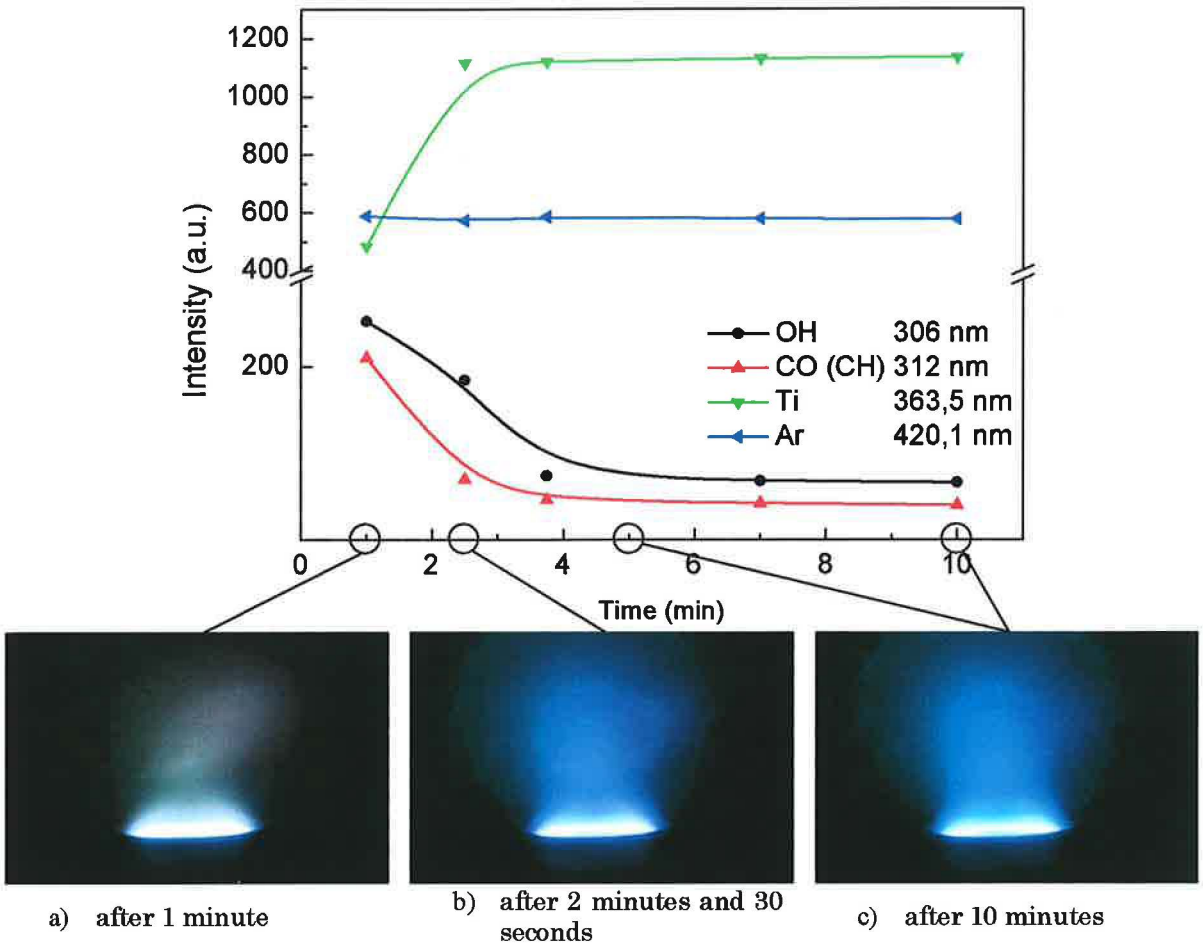

Fig. 3-2 Changes of the OES during the first minutes after starting the discharge

The typical optical emission spectra taken from the discharge in Ar, n-hexane and mixtures of these gases are shown in Fig. 3-3. The spectra were acquired after the discharge was stabilized (after 4 minute period from the beginning). Sputtering in pure Ar leads to intensive emission of neutral Ti atoms with a minor contribution from Ar atoms (Fig. 3-3a). When adding even a small amount (<5%) of n-hexane to argon, a considerable decrease in Ti emission intensity is observed, and in this case, the Ar lines dominate the spectrum (Fig. 3-3b). For depositions in pure n-hexane there is no emission from Ti and Ar atoms, and the spectrum consists of the CH and atomic hydrogen lines (Fig. 3-3c). Such a drastic decrease in sputtering yield of Ti is readily explained by the poisoning effects when the surface of the titanium target is covered by a dielectric carbonaceous layer formed from the plasma polymerization products.

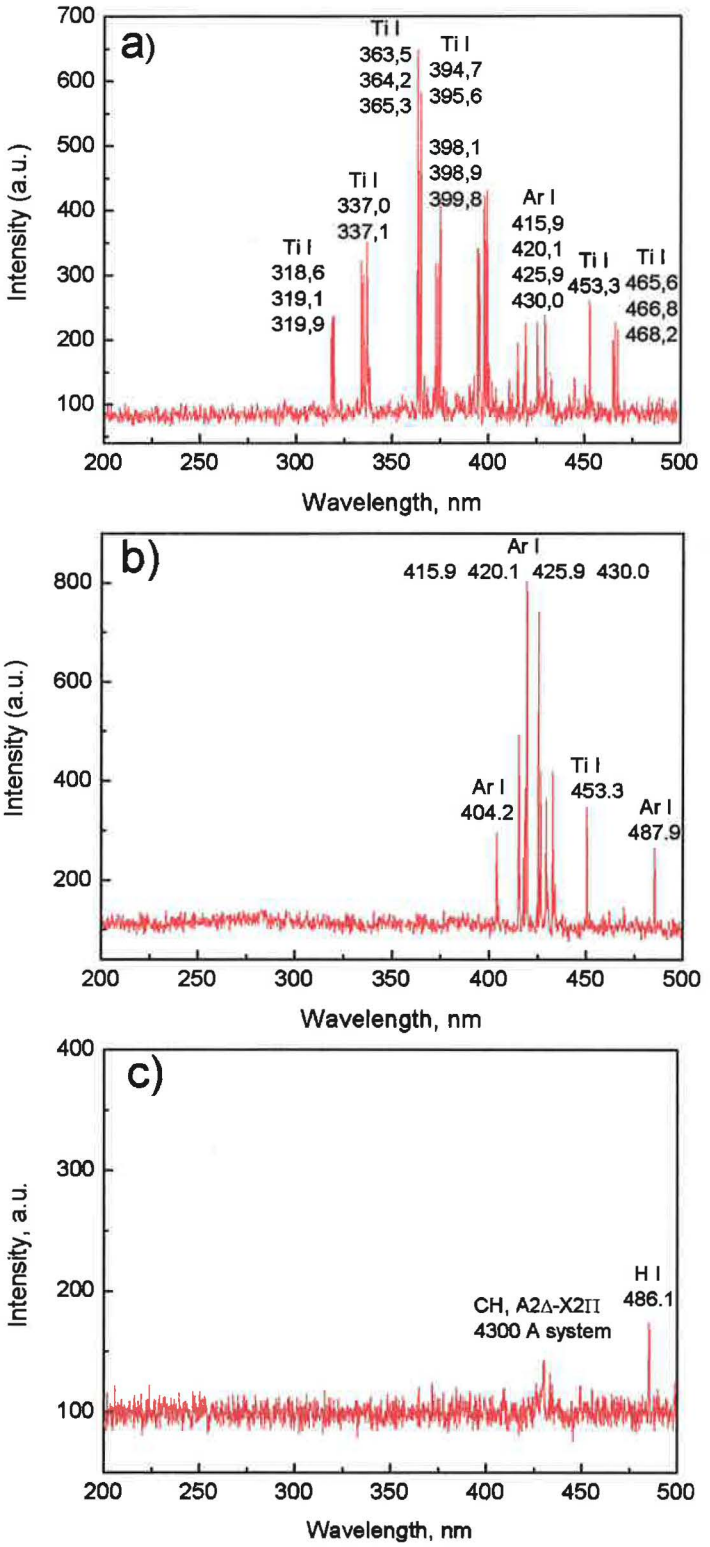

Fig. 3-3 The OES spectra taken in discharge of: a) pure Ar, b) mixture of Ar (97%) and n-hexane (3%) and c) pure n-hexane

The amount of Ti in the resultant films depends strongly on the composition of the reactive gas mixture and the OES analysis may serve as a powerful tool for controlling the deposition

of the films with required composition. For this purpose, we selected intensive and not overlapped lines of Ar at 420.1 nm and Ti at 465.3 nm. Fig. 3-4 demonstrates the deposition parameters adjustment. The discharge was initiated and maintained in pure Ar for 5 minutes with the substrate-holder hidden by shutter (period A). The first minutes of operation are characterized by the rapid increase and successive stabilization of emission from Ti atoms during next several minutes. Next, the valve to hexane line was opened and adjusted to give an intended Ti/Ar ratio (periods B, C). After that the shutter was removed and the deposition was started.

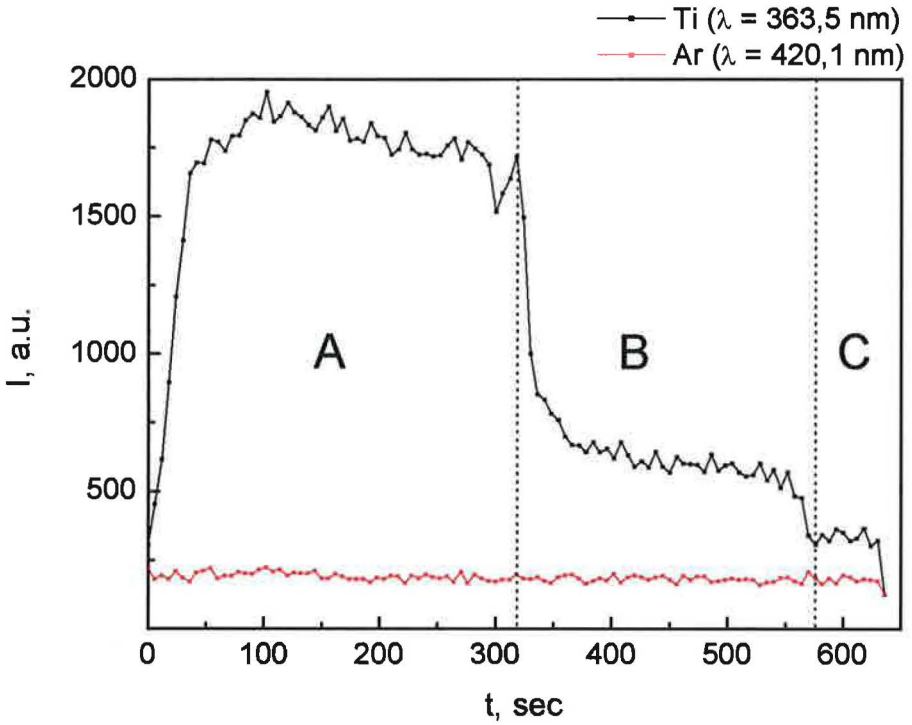

Fig. 3-4 The OES monitoring of the Ti and Ar lines during the deposition

3.1.1.2 Deposition rate in Ar/hexane mixture

Structure, chemical composition and morphology of Ti/hydrocarbon plasma polymer films were investigated in dependence on the flow rates of Ar and hexane in the working gas mixture. After series of experiment an optimum deposition conditions were determined. The deposition rates in pure argon, hexane and there mixture were determined by means of a quartz crystal microbalance. Position of quartz crystal microbalance gauge head above the erosion track of the magnetron target was kept the same (please see Fig. 2-1). Film thickness was estimated by profilometry and AFM with the accuracy within ~10% (please see Section

2.4.2). The dependence of the film thickness on the deposition time for the working gas of different composition is plotted in Fig. 3-5.

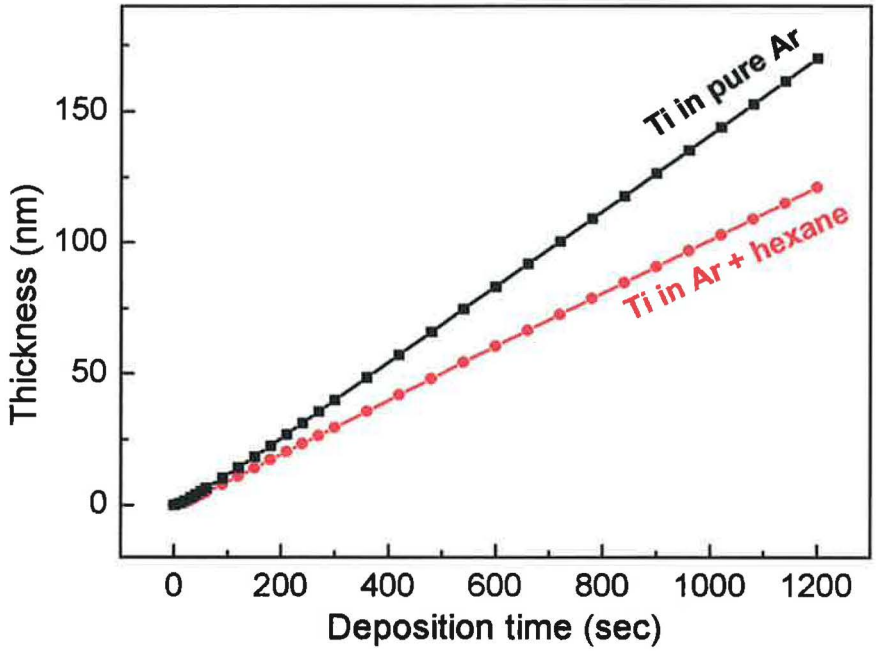

Fig. 3-5 Influence of the working gas composition on the film growth

Red line corresponds to the sample deposited in the mixture of argon (99.16%) and hexane (0.84%). As it will be shown later, the chemical composition of the surface of the resultant film is dramatically changing even is case of adding a small amount of hexane. Fig. 3-6 shows the dependence of the deposition rate of the nanocomposite films versus surface atomic concentration of Ti as obtained from XPS measurements. The flow rate of hexane was varied from 0.1 to 6.0 sccm which corresponds to ~17 at.% and 0 at.% of Ti, respectively. The highest amount of Ti in the films was achieved only during experiment in pure Ar atmosphere. Fig. 3-6 reflects the point that adding hexane to argon in working gas mixture metallic Ti target gets poisoned which decreases emission of Ti. Because of sputter yield of carbonaceous coating on the target is very low the overall deposition rate is decreasing.

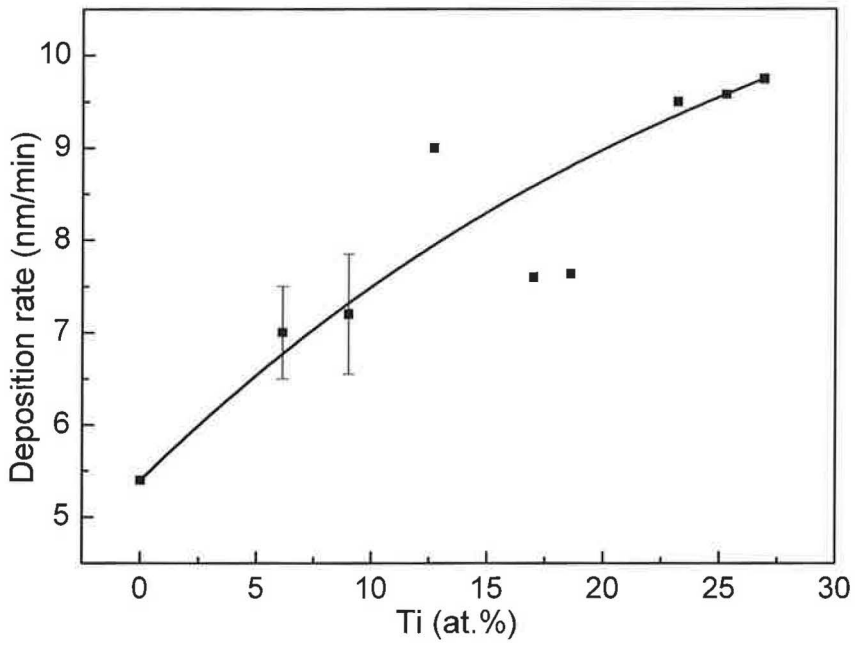

Fig. 3-6 Deposition rate versus surface atomic concentration of Ti derived from XPS spectra

3.1.2 Film deposition

3.1.2.1 Deposition conditions

The flow rate of the working gas Ar was fixed at 19 sccm. Presence of Ar is needed to sustain equilibrium between sputtering and deposition of the carbonaceous layers on the target because the sputter efficiency of carbon deposits is very low. The process pressure was adjusted at the beginning of the deposition process to 2 Pa by a throttle valve installed between the reactor and the diffusion pump. During the deposition process, the hexane flow rate was fixed. The DC power source was operated in constant current mode at discharge current of 0.2 A. The value of the discharge voltage in constant current mode is the lowest with a clean target (please see section 3.1.4). The samples were deposited mainly on Si (111) substrates precleaned with acetone, ethyl alcohol and distilled water in ultrasonic bath (ELMA Transsonic 310/H). Typical operating conditions are summarized in Table 3-1.

Table 3-1 Typical process parameters during the deposition

Parameter	Value
Base pressure	$< 5 \cdot 10^{-4}$ Pa
Leak rate	$< 2.2 \cdot 10^{-3}$ sccm
Process pressure	2 Pa
Argon flow rate	19 sccm
Hexane flow rate	0.1 – 6.6 sccm
Discharge current	0.2 A
Cathode voltage	~ 280 – 440 V
Deposition time	up to 1 hour

3.1.2.2 Substrates arrangement

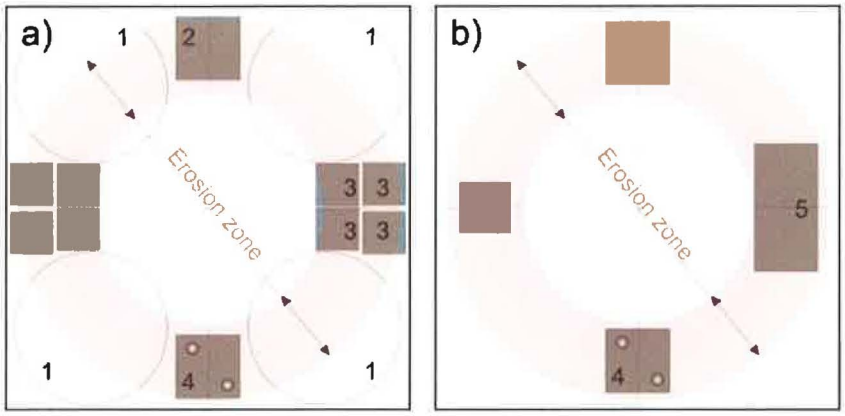

Fig. 3-7 Substrates arrangement for further: a) biological experiments; b) film analysis

Several types of the sample arrangements were used. Fig. 3-7 illustrates the two used layouts. Also position of the erosion zone of the target, which is 40 mm in inner diameter, is shown. The first layout was employed to prepare the samples for biological analysis (Section 2.5) (Fig. 3-7a). The second corresponds to deposit the films for XPS, AFM and FTIR characterizations (Fig. 3-7b). For more details of used substrates see the following table.

Table 3-2 Substrates description

Sample №	Material	Instrument	Description
1	Tissue culture dishes	ELISA	Section 2.5.3
2	Si(111) (1.5x1.5 cm)	XPS	Section 2.4.7
3	glass (1x1 cm)	bio tests	Sections 2.5.1, 2.5.2
4	Si(111) (1.5x1.5 cm) with mask	AFM	Section 2.4.2
5	glass (1.5x3 cm) covered by gold	FTIR RAS	Section 2.4.8
6	Si (1x1 cm)	FTIR transmission	Section 2.4.8

In addition, a series of depositions was performed on copper grids for TEM analysis and on clean glass slides for wettability tests. The samples were facing erosion zone of the magnetron.

3.1.3 Film analysis

3.1.3.1 XPS – surface analysis

The XPS was applied to the films sputtered in argon/hexane mixtures of different composition. The analysis of the films sputtered in pure argon and hexane was also performed.

Sputtering of titanium in pure argon did not produce pure metallic films in contrast with analogous experiments with silver [100]. The XPS detected 24% of titanium, 58% of oxygen and 18% of carbon; the latter probably originated from the hydrocarbon residues in the apparatus. The measured 24% of titanium is a maximal concentration that was achieved during a series of experiments; the concentration varying in the range of several percents under the same deposition conditions. High amount of oxygen was incorporated because of intensive oxidation of titanium when transferring the samples between the deposition chamber and XPS spectrometer in the ambient air. As it is shown below on the high-resolution XP spectra of carbon, titanium and oxygen (Fig. 3-8, Fig. 3-9, Fig. 3-10) nearly all of the titanium atoms are present in the oxidized forms. The most drastic changes in the film composition were detected when varying the n-hexane amount below 0.5% of the total working gas flow. The fitting results and elemental composition for several of these films are summarized in Table 3-3.

Table 3-3 The XPS analysis of Ti/hydrocarbon plasma polymer films

Sample №	Flow rate, sccm		Element	Peak position, eV	Assignment	Elemental content, at. %	Total concentration, at.%
	Ar	n-hexane					
T213	19	0,22 (1.15%)	C1s	281.8	C-Ti	2,2	72
				285.0	C-C, C-H	87	
				286.6	C-O	9,9	
				287.8	C=O	0,3	
				288.9	O-C=O	0,6	
			Ti2p1/2	454	Ti	1,8	6
				455,2	TiC	2,3	
				456,8	TixOy	9,9	
				458,5	TiO2	52,4	
			Ti2p3/2	460	Ti	2	
				461,4	TiC	4,6	
				463,3	TixOy	11,1	
				464,6	TiO2	15,9	
			O1s	530	TiO2	58,5	22
				531,6	TixOy	27,5	
				532,7	C-O, C=O	14	
T208	19	0,17 (0.89%)	C1s	281.8	C-Ti	6,2	63,5
				285.0	C-C, C-H	82,7	
				286.6	C-O	9	
				287.8	C=O	0,6	
				288.9	O-C=O	1,5	
			Ti2p1/2	454	Ti	3,9	9
				455,2	TiC	9,3	
				456,8	TixOy	8	

				458,5	TiO2	9,2	
			Ti2p3/2	460	Ti	0,7	
				461,4	TiC	21,5	
				463,3	TixOy	13	
				464,6	TiO2	34,3	
			O1s	530	TiO2	51,7	27,5
				531,6	TixOy	35,3	
				532,7	C-O, C=O	13	
T214	19	0,1 (0.50%)	C1s	281.8	C-Ti	17,6	48
				285.0	C-C, C-H	71,5	
				286.6	C-O	5,8	
				287.8	C=O	2,5	
				288.9	O-C=O	2,6	
			Ti2p1/2	454	Ti	4,5	17
				455,2	TiC	11,1	
				456,8	TixOy	8,9	
				458,5	TiO2	5,9	
			Ti2p3/2	460	Ti	1,9	
				461,4	TiC	23	
				463,3	TixOy	17,9	
				464,6	TiO2	26,8	
			O1s	530	TiO2	59,7	35
				531,6	TixOy	28	
				532,7	C-O, C=O	12,3	
T227	19	0	C1s	281.8	C-Ti	5	24
				285.0	C-C, C-H	74,8	
				286.6	C-O	7,5	
				287.8	C=O	7,5	
				288.9	O-C=O	5,2	
			Ti2p1/2	454	Ti	6,9	23
				455,2	TiC	5	
				456,8	TixOy	7,9	
				458,5	TiO2	13,2	
			Ti2p3/2	460	Ti	6,5	
				461,4	TiC	7,3	
				463,3	TixOy	12	
				464,6	TiO2	41,2	
			O1s	530	TiO2	75,8	53
				531,6	TixOy	21,3	
				532,7	C-O, C=O	2,9	

Fig. 3-8a shows deconvolution of the C 1s XPS of the sample sputtered in the mixture of argon and hexane with 0.5 % of n-hexane, whereas Fig. 3-8b demonstrates the evolution of the C 1s XPS with increasing the n-hexane content in the working gas mixture. The main peak in all the XPS corresponds to C-C/C-H bonds and is referenced at 285.0 eV. Part of the carbon atoms is oxidized and produce a higher binding energy tail. This was fit with three components at 286.7 (C-O), 287.8 (C=O) and 288.9 (O-C=O) eV. Furthermore, the C 1s spectrum is also characterized by the lower binding energy component. Its position at 281.8 eV allows assigning to titanium carbide. In the case of sputtering in pure argon (Fig. 3-8b black line), the extent of carbon oxidation is higher as there is a strong intensity of the O-C=O peak (for detailed view please see the inset of the figure). With increasing of hexane flow rate

(Fig. 3-8b), this component becomes smaller and the entire tail is less developed. This is consistent with elemental composition data (Table 3-3) showing 53 % of oxygen in the Ar-sputtered versus 22 % in the film with highest flow rate of hexane. The overall intensity of the carbon peak increases which reflects the increasing retention of carbon in the films (Table 3-3). Another distinct difference between the spectra is related with remarkable enhancement of the signal from titanium carbide. It reaches ~18 % of the total carbon signal for the 0.5 % n-hexane/Ar mixture. At higher concentrations of n-hexane this component decays and none of it is present in the film sputtered in pure n-hexane.

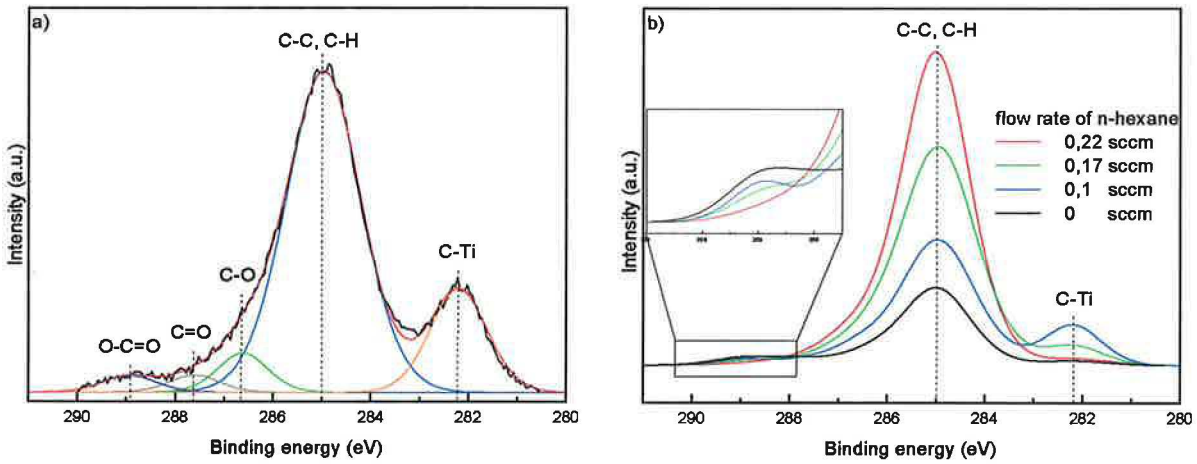

Fig. 3-8 The C 1s XPS of Ti/hydrocarbon plasma polymers: a) example of fitting (T214); b) evolution of the spectra with n-hexane flow rate increasing

The high amount of oxygen, in particular in argon-sputtered film, cannot by itself account for the higher extent of carbon oxidation because a significant part of oxygen is bound in titanium oxide. Titanium oxide is known to form readily when metallic titanium is exposed to the ambient air. The Ti 2p XP spectra depicted in Fig. 3-9 consist of $2p_{3/2}$ and $2p_{1/2}$ spin orbit peaks. The dotted vertical lines indicate the positions of centroids of the fitting components. The fitting procedure was optimized as follows. Each of the spin orbit peaks was fitted with four components. First, the better resolved Ti $2p_{1/2}$ part was deconvoluted. Obviously, the location of the strongest peak at 458.5 indicates that the main titanium species is TiO_2 (blue line). Metallic titanium is usually found between 453.1 and 454.0 eV, and therefore a restriction of binding energy $\leq$454.0 eV was imposed on the metal Ti component of the spectrum (grey line). The peak at 455.2 eV was noticed to behave in accord with TiC component of the C 1s spectra and thus it was ascribed to titanium carbide (green line). Such assignment is further supported by the data from literature giving the position of TiC around

455 eV. Moreover, it was necessary to add another fitting component to the region between TiO_2 and TiC. Titanium monoxide reportedly gives peaks between 454.5 and 456 eV. It seems reasonable to assign this component to substoichiometric titanium oxides Ti_xO_y (pink line). After the fitting procedure for the Ti $2p_{1/2}$ part of the spectrum had been performed the ratio between integral intensities of the TiO_2, Ti_xO_y, TiC and Ti peaks was calculated. Subsequently, the Ti $2p_{3/2}$ part of the spectrum was fitted by the same four components with the ratio between them fixed at the values obtained from the Ti $2p_{1/2}$. The position of the TiO_2 and TiC components was restrained at 464.6 and 464.1 eV with 0.1 eV tolerance, whereas the Ti_xO_y and Ti peaks were allowed to fit with 0.4 eV tolerance. Finally, the overall deconvolution of the Ti 2p spectrum was performed. As seen from Fig. 3-9, the deconvolution procedure works well for all the spectra with a slight exception of the sample with 0.1 sccm of hexane where it was impossible to maintain the ratio between the individual components for the Ti $2p_{3/2}$ part. The uncertainty in position and width of the substoichiometric titanium peak is probably responsible for this shortcoming. The XP spectra demonstrate that in the near surface area titanium is strongly oxidized, the dominating species being TiO_2 and substoichiometric titanium oxides.

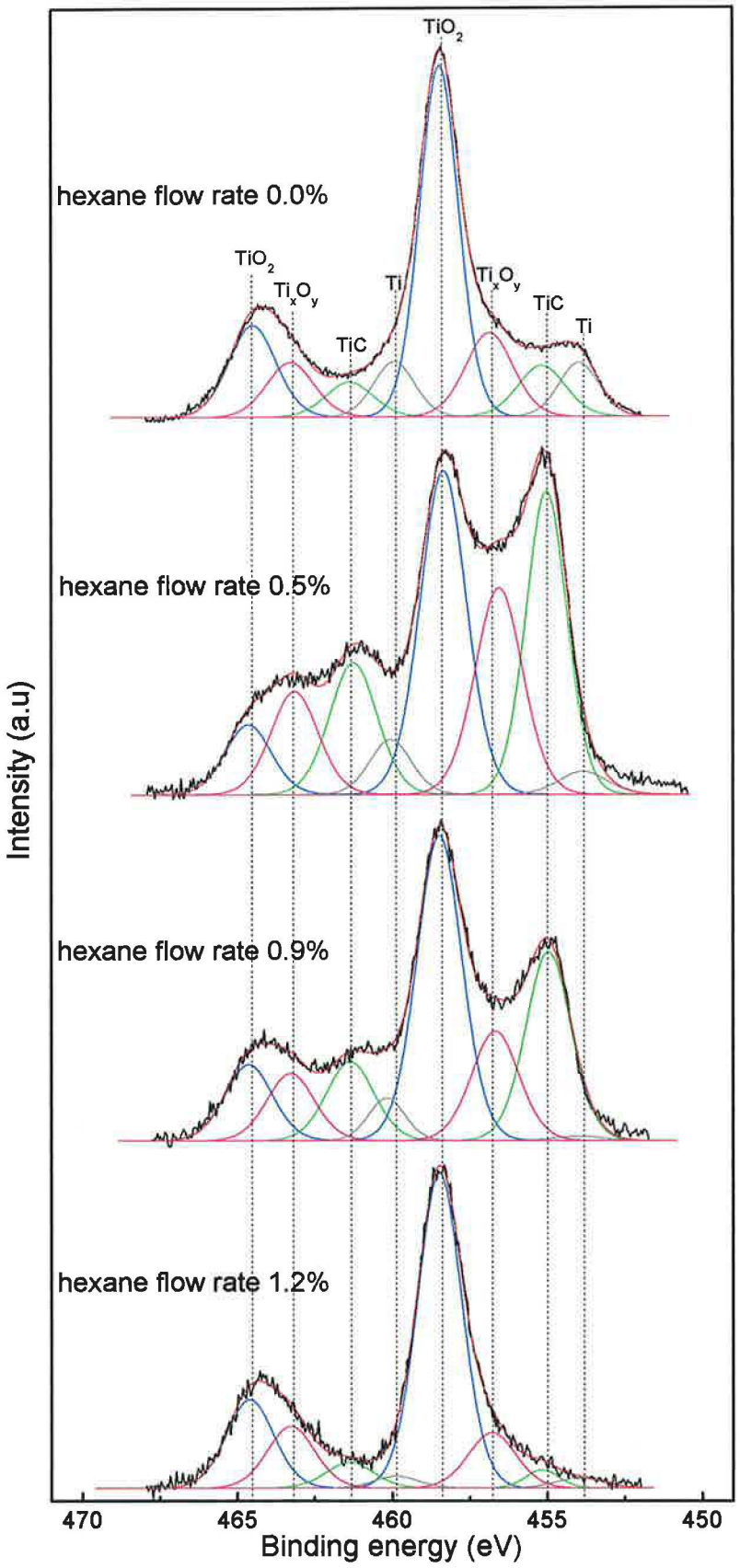

Fig. 3-9 The Ti 2p XPS of Ti/hydrocarbon plasma polymers

The O 1s spectra reveal double appearance which changes in dependence on the film composition. The example of the oxygen peak deconvolution is shown in Fig. 3-10a for the film sputtered with 0.5% of hexane. The distinct shoulder is shifted by 1.6 eV to higher binding energy with respect to the main component at 530.0 eV. Both contributions can be consequently ascribed to oxygen bound with titanium (the main peak) and oxygen bound with carbon (the shoulder). Note that the width of the oxygen-titanium peak is more than 2 eV and such a broadening is evidently caused by substoichiometric titanium oxides. Furthermore, two components only did not suffice to fit the entire spectrum and the third peak was introduced at 532.8 eV. The presence of two bonding environments in the shoulder can be considered as the contribution from the double (531.6 eV) and single (532.8 eV) oxygen-carbon bonds. The chemical shift of about 1.5 eV between C=O and C-O was reported previously in [Briggs, Beamson].

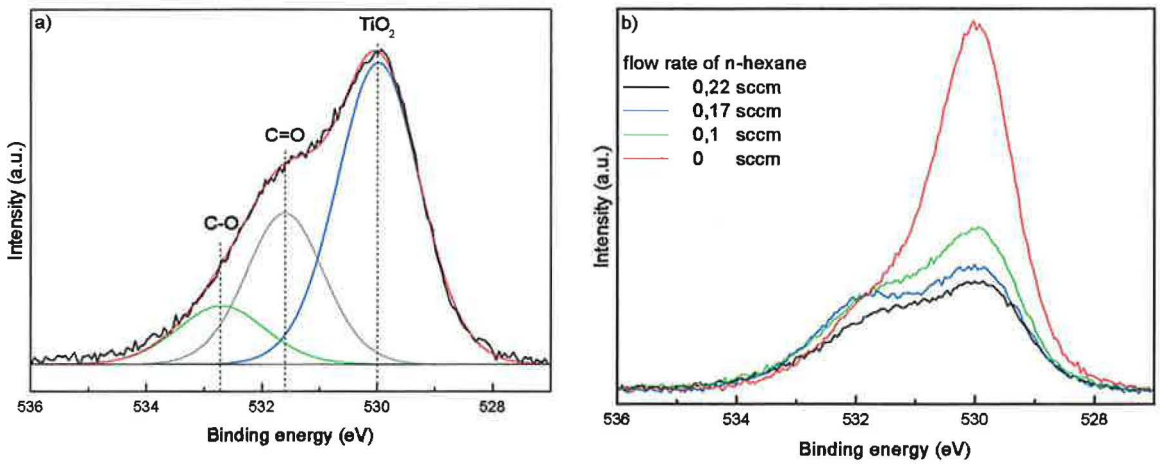

Fig. 3-10 The O 1s XPS of Ti/hydrocarbon plasma polymers: a) example of fitting (T214); b) evolution of the spectra with n-hexane flow rate changing

The film sputtered in pure argon has only slight asymmetry with titanium oxides dominating the spectrum (Fig. 3-10b). This comes in line with the low concentration of carbon in this film. With increasing the amount of hexane in the gas mixture the concentration of carbon in the film increases and the carbon-oxygen species contribute more significantly to the O 1s XPS. As an instance, in the film deposited with 0.22 sccm of hexane about half of oxygen is bound with carbon. Given that there is 22 % of oxygen in this film, ~11 % of it belongs to titanium. The concentration of titanium is 6 % in this film and hence it is mainly in the TiO_2 form (please also see Fig. 3-9d).

Several final conclusions can be drawn from the XPS analysis. By adjusting the hexane content in the gas mixture the concentration of carbon and titanium can be controlled in reciprocal way. Titanium is present in the metallic, TiC, Ti_xO_y and TiO_2 forms, the latter being dominant in all the cases except for the lowest admixtures of hexane where approximately equal contribution from titanium carbide is detected. This is probably explained by the change in plasma parameters when moving from argon to argon/hexane mixtures and further to pure hexane plasma.

3.1.3.2 RBS/ERDA

The same films were analyzed using the RBS/ERDA. The results of elemental composition calculated from the RBS/ERDA data are given in Table 3-4. As expected, the film sputtered in pure hexane contains small amount (<1%) of titanium. The C/H ratio is almost equal to unity. This value is much higher than that of the hexane precursor (C/H=0.43) which indicates the high extent of unsaturation in the plasma polymer. The effect of hydrogen detachment during plasma polymerization was previously observed for various organic precursors [101].

Table 3-4 The RBS/ERDA analysis of Ti/hydrocarbon plasma polymer films.

Sample	Element	Elemental content, at. %
Sputtering in pure Ar, 2 Pa, 18 sccm, 0.2 A, 20 min	H	58.0
	Ti	20.0
	C	9.0
	O	11.0
Sputtering in pure hexane, 2 Pa, 6 sccm, 0.2 A, 15 min	H	48.0
	Ti	0.6
	C	47.9
	O	3.5

Oxygen is found within the hexane-sputtered film in amount of 3.5% as a result of post-deposition oxidation in air. The RBS concentration of oxygen is lower but consistent with that of XPS data taking into account that the latter does not detect hydrogen and gives over-estimated concentration of the other elements.

The film sputtered in argon is remarkable for the anomalously high hydrogen content, the fact which could not be established by XPS. Only 9% of carbon was detected by RBS which contrasts with 58% of hydrogen. Highly unsaturated character of carbon being taken into account, most of hydrogen must be bound with titanium. Titanium is known to bind gases, hydrogen in particular, to form hydrides. We assume here that even small hydrocarbon contamination results in significant increase of atomic hydrogen concentration in the plasma,

which is effectively sorbed by titanium. Titanium is found in amount of 20% in this kind of film. The concentration of oxygen is 11%. This value is much lower than that detected by XPS and indicates that oxidation affects mainly the outermost layers of the film.

3.1.3.3 TEM

The structure of the film bulk was analyzed by means of transmission electron microscopy (TEM). For this purpose, a separate set of samples with thickness of 50-100 nm was deposited on 3 nm carbon foils supported by ø3 mm 200-mesh copper grids. Out of technical reasons the deposition could not be carried out simultaneously with the deposition of thicker samples used for the other analyses.

First TEM analysis was performed on a Jeol FX-2000 microscope at 200 kV accelerating voltage (camera length 930 mm). TEM image (Fig. 3-11) demonstrates that the film deposited by magnetron sputtering in Ar/n-hexane mixture is a composite hydrocarbon plasma polymer with the embedded titanium aggregates (dark dots on the left photo).

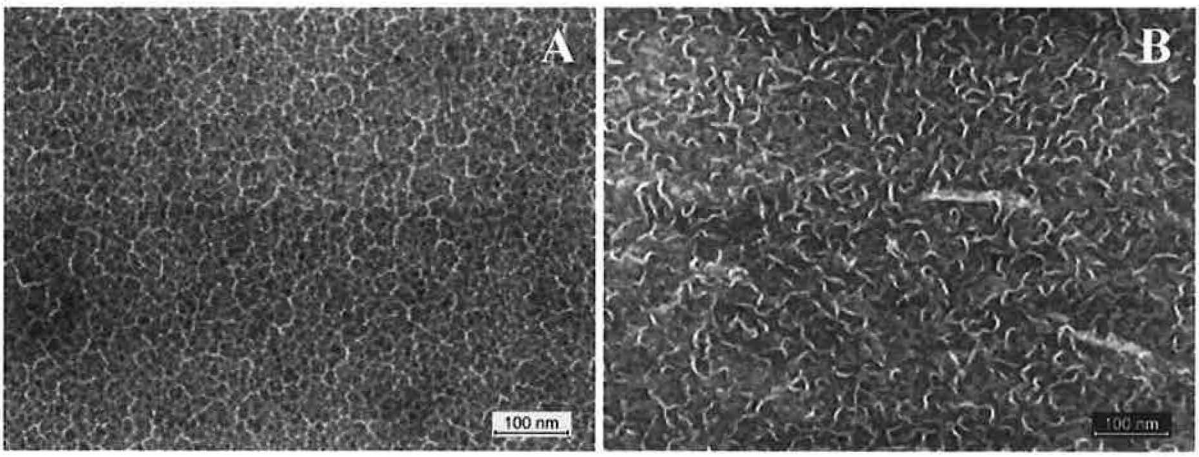

Fig. 3-11 TEM image of composite Ti/hydrocarbon plasma polymer film with a) 6 and b) 0 at.% Ti

3.1.3.4 Contact angle measurement

Static contact angle measurements of the films revealed strong dependence on the Ti/hydrocarbon plasma polymer composition. As it was shown by XPS measurements (please see Section 3.1.3.1) the outermost layers of Ti-rich films consist mainly of oxidized titanium spicies. For example, t he films with 17 and 23 at.% of Ti have 60 and 74% of Ti_xO_y, respectively. It is known that substances such as TiO_x and hydrocarbon exhibit different behavior when their surfaces interact with droplet of water. Hydrophilic titanium oxide surfaces are reported to possess static contact angle of several degrees. On the contrary, hydrocarbon is highly water repellent material with contact angle of about 90 degrees.

Fig. 3-12 shows the results of water contact angle tests, which were done by the method described in Section 2.4.9. The measurements were performed during first 30 minutes after exposing samples to ambient air and on the samples of approximately equal thickness (150 nm) to exclude its influence. It is clearly seen that the films with higher amount of Ti on the surface show hydrophilic behavior. With decreasing Ti concentration static contact angle increases practically linearly.

When analyzing surface wettability one should bear in mind that roughness of the surface may induce significant deviations in contact angle values. In order to estimate the influence of roughness on the values of static contact angles, the AFM observations of topography were performed. Typical AFM image of Ti/hydrocarbon plasma polymer film is shown in Fig. 3-12. The roughness changes from 1.0 nm to 3.3 nm for the samples with 0 and 26 at.% of Ti respectively.

These values are one order of magnitude lower than roughness values usually influencing the contact angle [102, 103]. Also the surface profile analysis was performed by Surfometer SF200 in order to see topography (larger scale roughness). This study also showed that the films are rather flat. The AFM and surfometer studies confirmed that the observed slight increase of roughness could not by itself account for an decrease of contact angle.

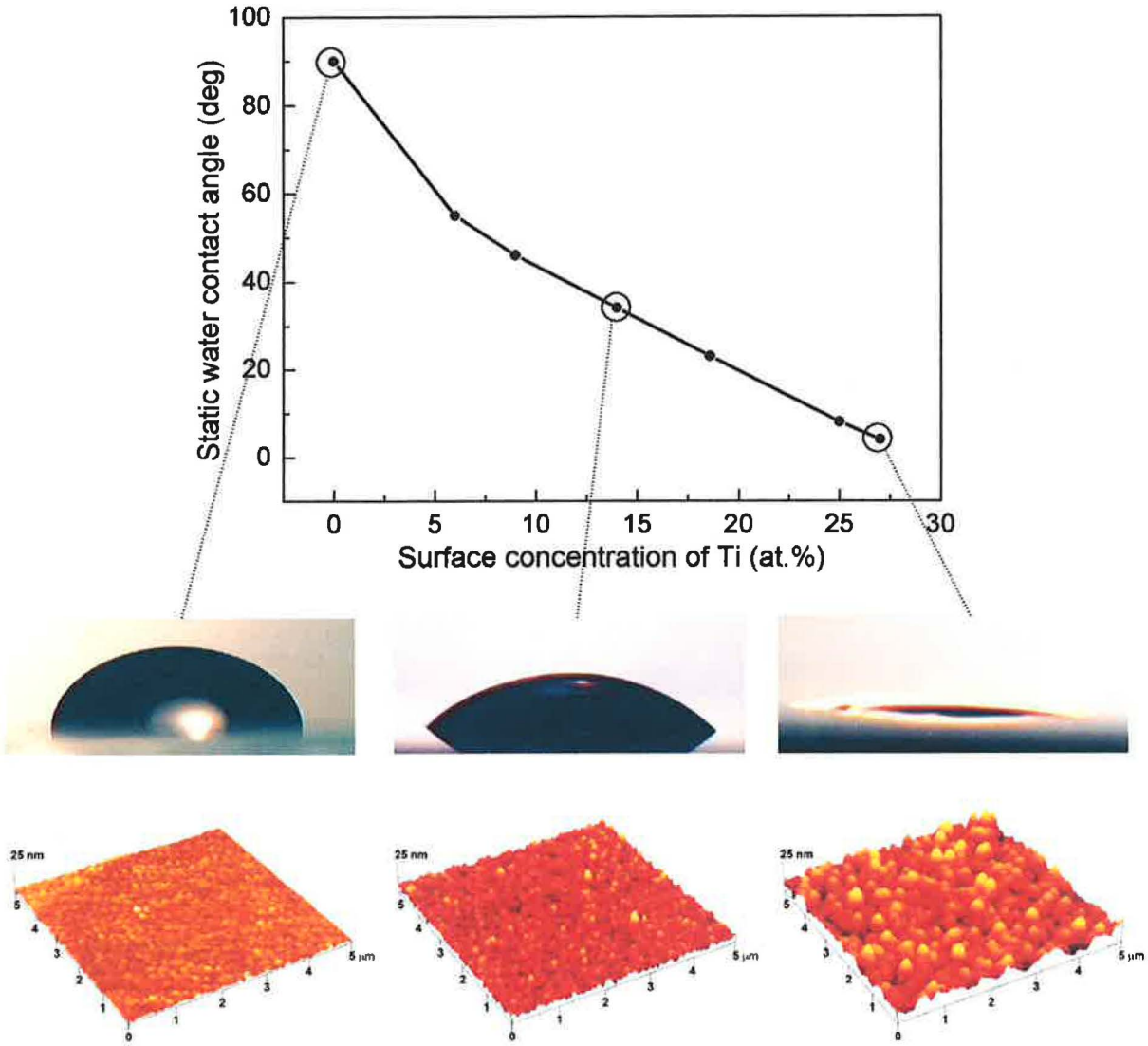

Fig. 3-12 Static contact angle versus surface concentration of Ti and topography of selected samples

3.1.3.5 SPM

The SPM analysis was started by measuring the topography of the Ti/hydrocarbon films with 3 and 20 at.% of Ti in the Dynamic Force Mode (DFM). Both films show identical surface features regardless the film composition (Fig. 3-13). The RMS roughness of the films is about 1.5 nm as measured on the 1x1 µm images. For comparison, the image of silicon substrate is also shown on the same figure. The roughness of silicon is 0.2-0.4 nm.

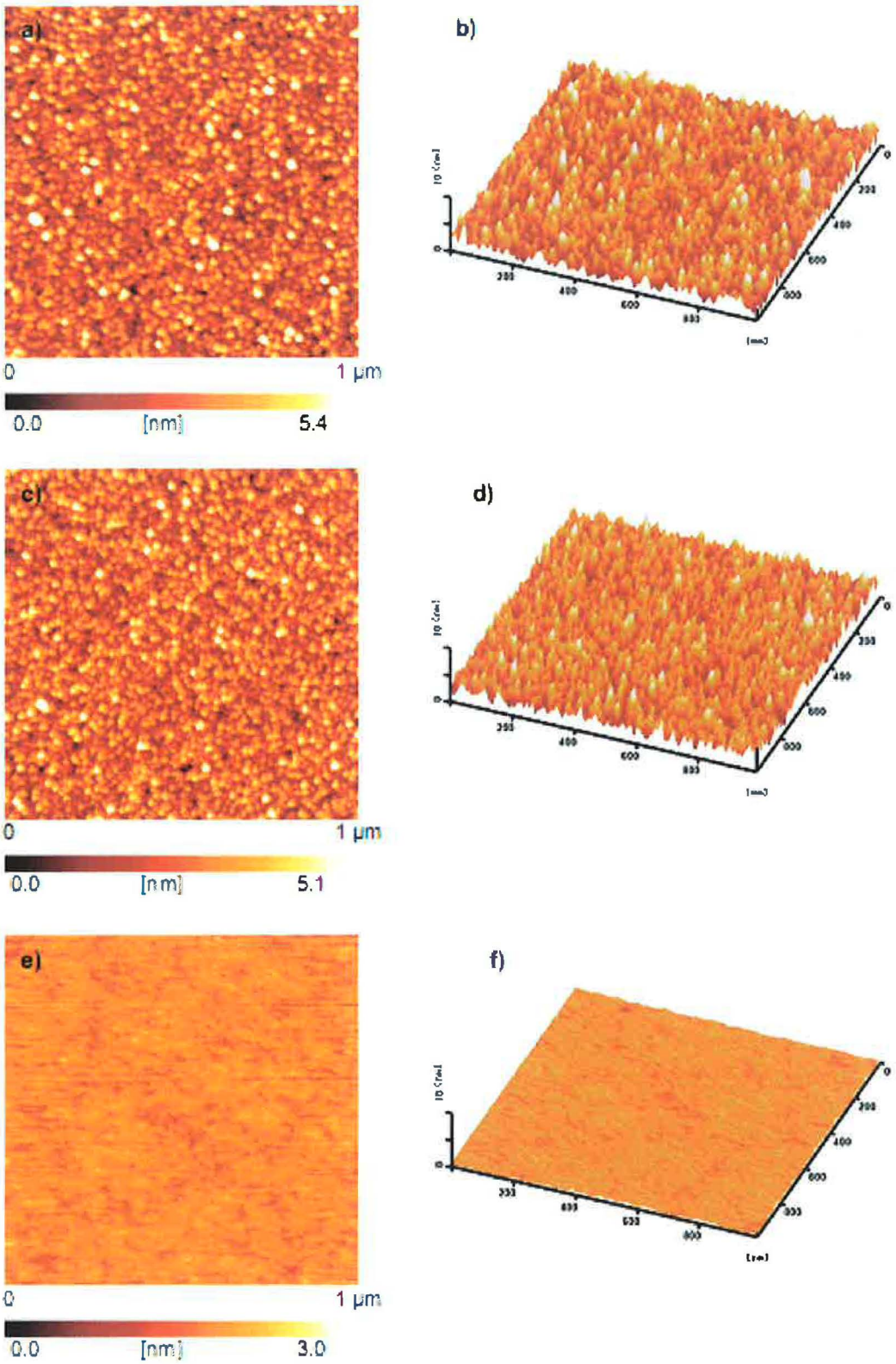

Fig. 3-13 Topography of the Ti/hydrocarbon films deposited on silicon substrate: a,b) 3% Ti; c,d) 20% Ti; e,f) Si

The same films were analyzed in the Kelvin Force Mode (KFM). The scans were conducted over the boundary between the film and silicon substrate. Although the potential imaging in

the KFM mode is less sensitive to topographical features, the films with close thickness were chosen to avoid any inconsistency. The tip was scanned over 30 and 40 nm thick films containing 20 and 3 % of Ti, respectively. The topography and potential images (Fig. 3-14 a-d) were taken simultaneously with the same tip and settings used for both samples. The left part of the images corresponds to the Ti/hydrocarbon film and the right part corresponds to silicon substrate which served as a reference. The topography pictures appear identical for both of the films (Fig. 3-14a, b). However, a significant difference between them can be observed in the potential images. The surface potential of the Ti-rich film is more positive with respect to silicon (Fig. 3-14c), whereas in the case of the film with low concentration of Ti it becomes more negative (Fig. 3-14d). Obviously, the increase of titanium concentration does not influence the surface roughness but has a significant impact on the surface potential of the composite films.

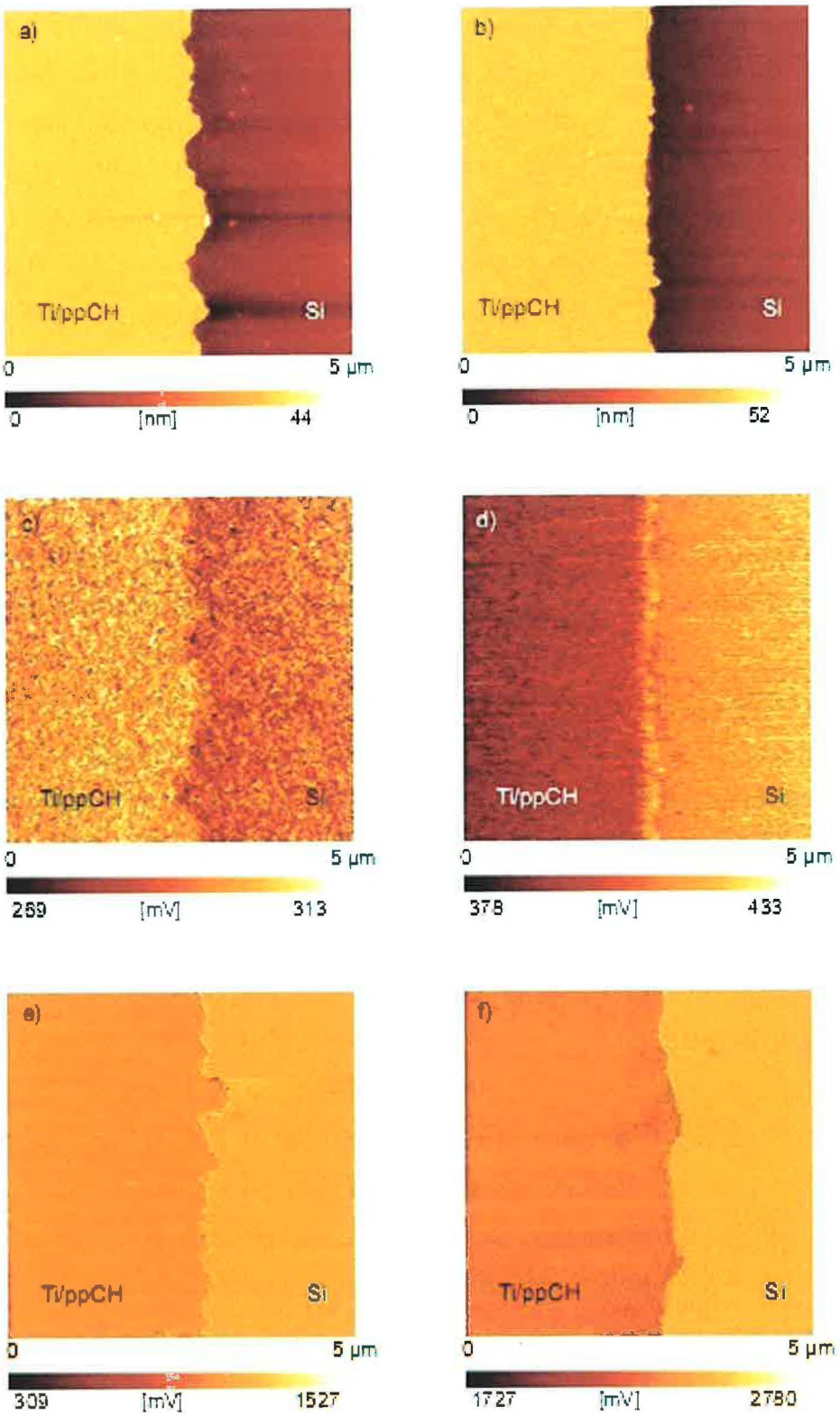

Fig. 3-14 The topography (a, b), potential (c, d) and elasticity (e, f) images of the Ti/hydrocarbon films with 20% of Ti (the left column) and 3% of Ti (the right column)

These findings are consistent with electrokinetic potential measurements. Isoelectric points (IEP) of silica and titania depend on material characteristics such as crystallographic phase

and chemical composition. However, spread in their values published in literature is narrow and IEPs are generally found at about pH 2 and 6 for silica and titania, respectively [104]. This means that under neutral solution the surface of silica will be charged more negatively than titania. The Ti/hydrocarbon surfaces studied here are covered with water molecules at room temperature and relative humidity of 40%. As it was mentioned above, titanium is present predominantly in a form of substoichiometric oxides in these films, whereas the surface of silicon substrate is covered by a layer of native silicon oxide. Oxides exposed to an ambient atmosphere are generally assumed to be rich with surface hydroxyl groups which are protonated or deprotonated depending on pH and IEP of the material. Since the IEP of silica is very low, the predominant surface species are deprotonated silanols SiO^- and the surface is charged negatively under neutral conditions. On the other hand, the IEP of titanium oxide is close to neutral pH so that TiO^- and $TiOH_2^+$ species are present in approximately equal amount. Hence, the net surface charge of Ti-rich film is close to neutral and it is more positive with respect to silicon substrate.

With decreasing Ti content the surface charge shifts to negative values and for the film with 3% Ti it is more negative than the net charge of the silicon substrate. The negative charge of hydrocarbon plasma polymers is a known phenomenon [105] attributed to the presence of oxygen-containing groups, mainly carbonyls and carboxyls. These groups are readily formed as a result of post-deposition oxidation reaction of carbon radicals with oxygen and water molecules [106].

The Visco-Elastic Atomic Force (VE-AFM) images were acquired on the same films immediately after the KFM. The measurements on the films with less than 10 nm thickness showed a bad contrast and are not shown. The cantilever modulation amplitude of 5 nm was not sufficiently small relative to the film thickness to avoid the influence of the substrate. However, the thicker samples reported here produced stable and reproducible contrast (Fig. 3-14e, f). The amplitude of the tip in contact with both composites is lower (darker area) than on underlying silicon substrate meaning they are softer. Furthermore, the elasticity scan of the 3% Ti/hydrocarbon film shows higher contrast with respect to silicon than that of the 20% Ti/hydrocarbon film, i.e. the absolute difference of tip amplitudes between the film and the Si substrate decreases from 140 to 90 mV with increasing Ti content. Thus, as expected the films with higher Ti content are harder.

The adhesion force of the Ti/hydrocarbon films against silicon was measured as a pull-off force of Si tip on the retracting force-distance curve. To avoid an inconsistency between the measurements with different cantilevers the adhesion force was normalized by the tip radius.

For comparison, the force-distance curves were measured against clean silicon substrate as well. The adhesion force measured in air increases with Ti content from 40mN/m for the 0 and 3% Ti/hydrocarbon film to 120 mN/m for the 20% Ti/hydrocarbon film (Fig. 3-15). The combination $Si_{tip}/Si_{substrate}$ provides the highest adhesion force of 630 mN/m. The water contact angle on clean Si was less than 10°. It increased to 25° for the 20% Ti/hydrocarbon film and reached 80° for the plasma polymer without titanium. Hydrophilic surfaces at humidity >30% contain a microscopic layer of water molecules adsorbed on the surface of nanocomposite Ti/hydrocarbon plasma polymer films. Presence of capillary forces is responsible for enhanced adhesion between the 20% Ti/hydrocarbon film and silicon. The measurements performed under $1 \cdot 10^{-3}$ Pa vacuum allow avoiding the influence of the capillary forces. In this case, the hydrophobic samples deficient with Ti exhibit identical adhesion against silicon, whereas hydrophilic surfaces show the adhesion force significantly lower than that measured in air. Nevertheless, the trend of increasing the adhesion with Ti content can be observed.

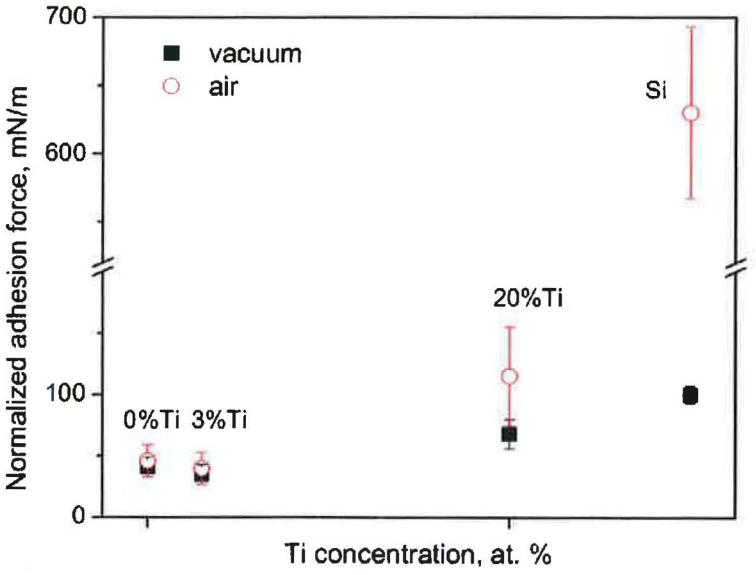

Fig. 3-15 The adhesion force of the Ti/hydrocarbon films against Si

3.1.4 Target analysis

As it is shown on Fig. 3-16, self-bias voltage is rapidly decreasing during first 2 minutes after discharge ignition in the Ar atmosphere. Obviously, the cause for this decay is the sputter-cleaning of the target surface.

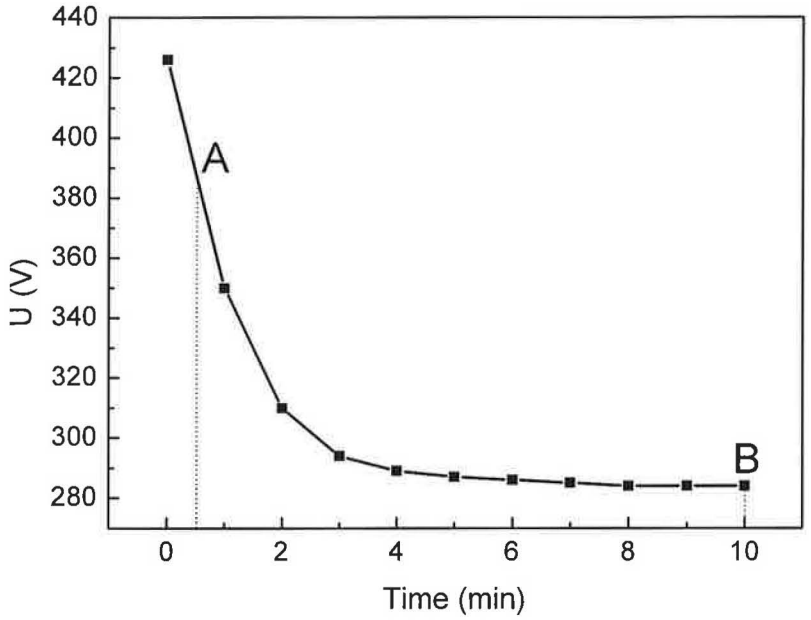

Fig. 3-16 Time dependence of voltage in Ar atmosphere

To demonstrate this, two samples were prepared in Ar under identical conditions but with different deposition time: A – 30 seconds and B) – 10 minutes. Chemical composition of these films according to XPS analysis is following: titanium 20.5 and 24.0 at.%; carbon 27.0 and 18.0 at.%; oxygen 52.5 and 58.0 at.% for A and B regions, respectively. The high-resolution spectra of C 1s and Ti 2p are shown in Fig. 3-17. The apparent difference between the samples is in the ratio of TiC and metallic titanium. For the film deposited for 30 seconds when cleaning of the target has not been yet completed, the TiC peak is clearly seen in the C 1s spectrum (Fig. 3-17a). The intensity of the Ti 2p signal in TiC region is also higher (Fig. 3-17b). The formation of TiC phase in the films deposited with small admixtures of n-hexane was discussed above. Here, the source of carbon is carbonaceous residues which inevitably remain on the target surface despite the pre-deposition cleaning with ethanol and abrasive paper. Vice versa, the film deposited for 10 minutes shows much smaller signal from TiC and enhanced metallic titanium peak. The voltage by this time is already stabilized which indicates that the etching of surface impurities is completed and sputtering proceeds with clean Ti target.

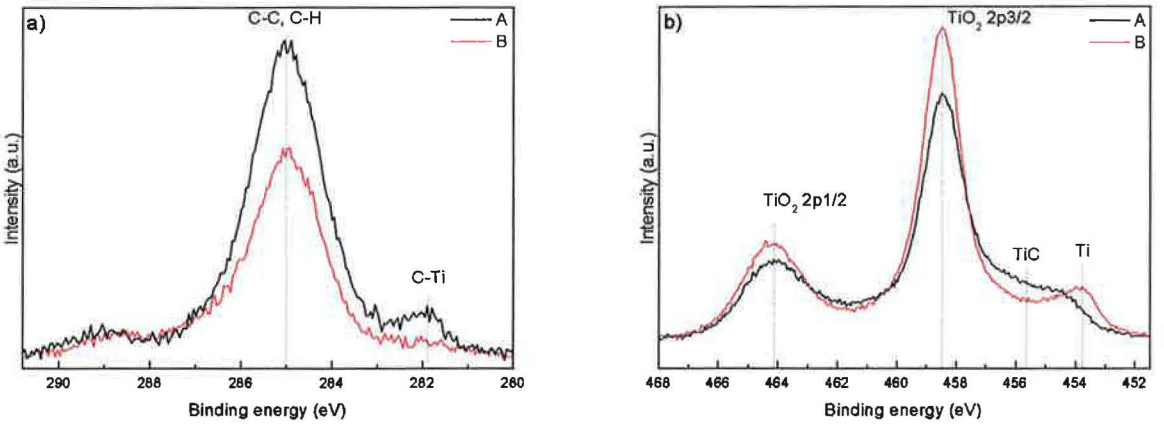

Fig. 3-17 XPS spectra of poisoned and clean target: a) C 1s, b) Ti 2p

As it was described in Section 1.2.4, when hexane is added to Ar when sputtering Ti target plasma polymerization process takes place and a hydrocarbon plasma polymer deposits on adjacent surfaces including surface of the target, i.e. poisoning of the target. The competition between target sputter cleaning to its metallic state and its poisoning depends on hexane concentration and it is reflected in self-bias behavior (Fig. 3-18). Apparently, with addition of hexane the decay of self-bias slows down and even turns to increasing character. At high hexane concentration, the poisoning of the target by carbonaceous layer is very intensive and the self-bias voltage needs to be increased to sustain the discharge.

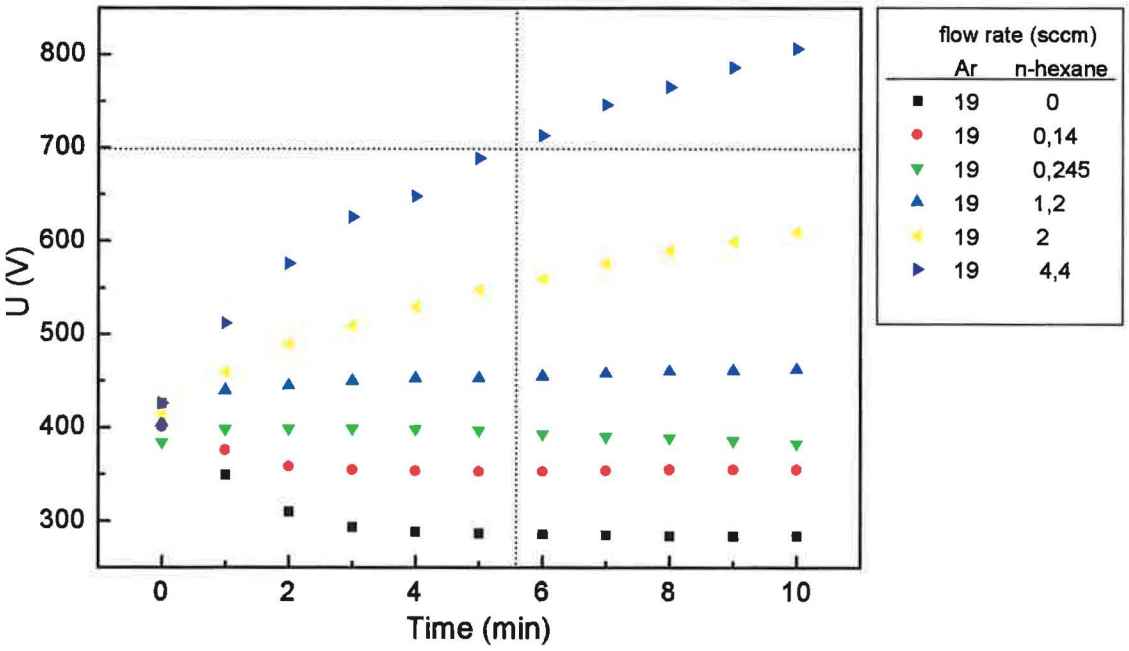

Fig. 3-18 Self-bias voltage versus deposition time for different working gas mixtures

The examples of Ti targets sputtered in Ar and in hexane/Ar mixtures are given in Fig. 3-19. Black carbonaceous deposits are very well seen on the target sputtered with the presence of hexane.

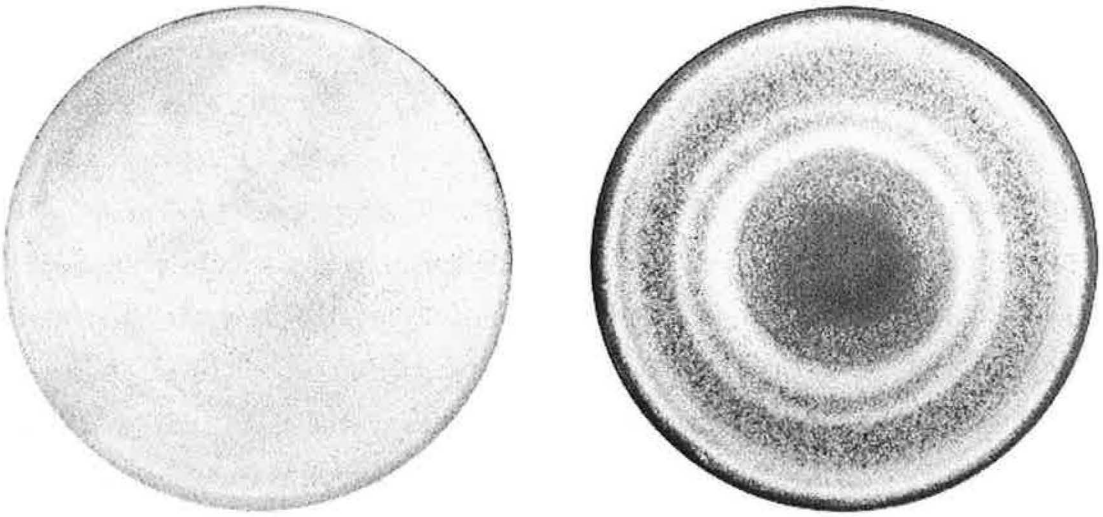

Fig. 3-19 Targets after deposition in Ar and Ar/hexane, respectively

3.1.5 Biological response of nanocomposite Ti/hydrocarbon plasma polymer films

3.1.5.1 Interaction of the Ti/hydrocarbon films with biomolecules

The interaction of the Ti/hydrocarbon films with biomolecules was studied in terms of their ability to adsorb fibrinogen. The samples were dipped into the 50 μg/ml fibrinogen solution in phosphate buffer saline (PBS) for 1 minute so that only one half of the sample was immersed, the other half being kept intact. After immersion, the samples were repeatedly rinsed with Mill-Q water, and blown dry by N_2. The SPM analysis was performed in air at humidity 35-40% immediately after the protein immobilization. Fig. 3-21a,b show the topography of fibrinogen layer adsorbed on the 3% Ti/hydrocarbon film. The left part of the pictures corresponds to the fibrinogen coating, whereas the right part corresponds to the uncovered composite film. The protein strands can be observed, however it is difficult to estimate from topography pattern whether fibrinogen forms a continuous layer (Fig. 3-21a, b). At scan size of 5 μm and resolution of 256 data points the AFM sampling interval used here is 5000/256 ≈ 20 nm. Fibrinogen molecule consists of three globules (two outward D domains and central E domain Fig. 3-20) 5-6 nm in diameter interconnected by the coiled-coil regions which extend for the length of 47 nm in unfolded state [107]. Additionally, two αC domains extend further from the D-domains. At neutral pH αC domains fold back and strongly bind to the central E domain. Hence, with assumption of an individual fibrinogen molecule as a rod with diameter 6 and length 47 nm they may not necessarily be seen at the mentioned scan size and resolution. However, the 1 μm scan with the sampling interval of 4 nm also showed only fibrinogen aggregates of bigger size (data not shown). The average thickness of the fibrinogen layer is 6-10 nm which is consistent with above reported diameter of fibrinogen domains.

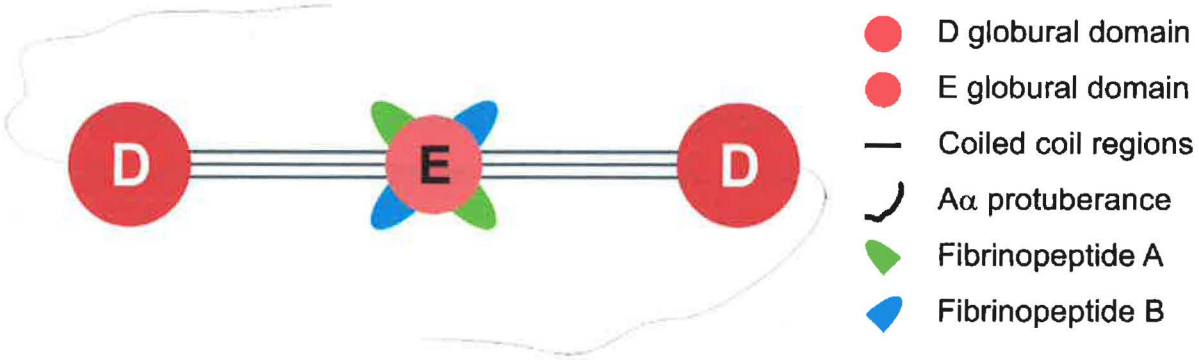

Fig. 3-20 Schematic structure of the fibrinogen molecular

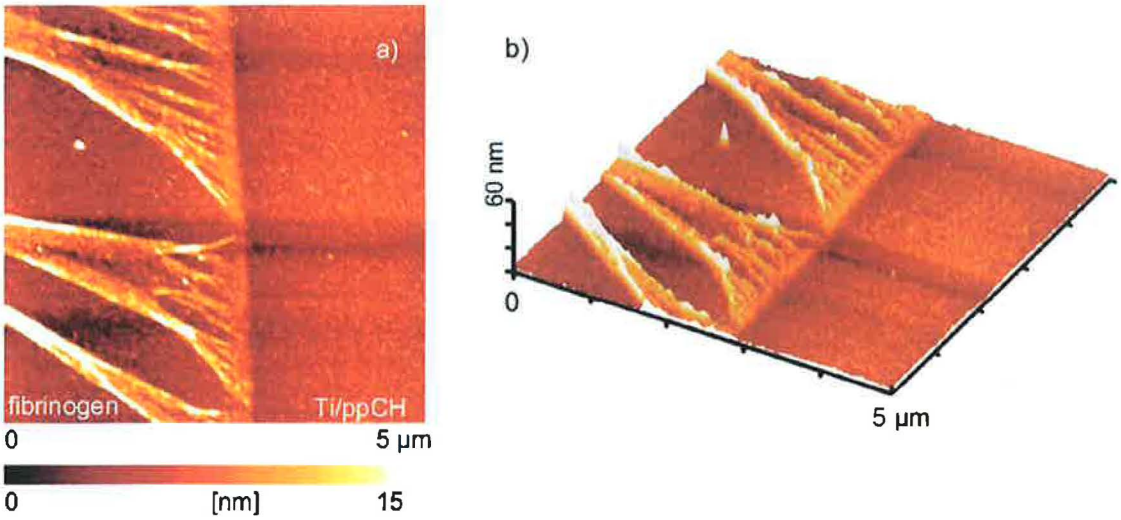

Fig. 3-21 The topography a) top view and b) 3D of fibrinogen adsorbed on 3% Ti/hydrocarbon film

The Kelvin Force mode (KFM) analysis shows the higher potential of the fibrinogen layer in comparison with the Ti/hydrocarbon film (Fig. 3-22).

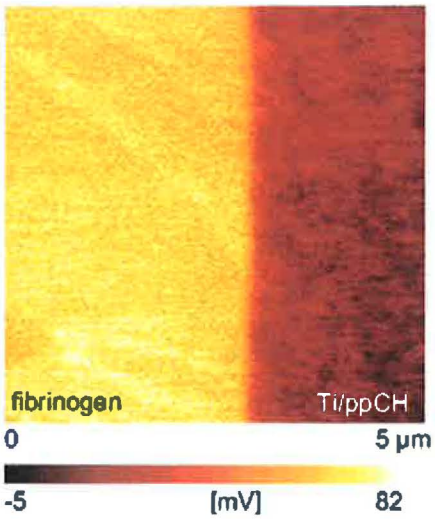

Fig. 3-22 The KMF of fibrinogen adsorbed on 3% Ti/hydrocarbon film

The potential difference was determined from the histogram analysis. Fig. 3-23 shows the statistical distribution of the potential of all the points in the KFM images of different samples. The +50 mV difference between the maxima on the histogram curves correspond to potential difference between the fibrinogen layer and Ti/hydrocarbon film (Fig. 3-23a). Fibrinogen was also adsorbed on clean Si substrate with potential difference being +30 mV (Fig. 3-23b). This is very well consistent with the above mentioned +20 mV potential difference between Si and the 3% Ti/hydrocarbon film (Fig. 3-23c).

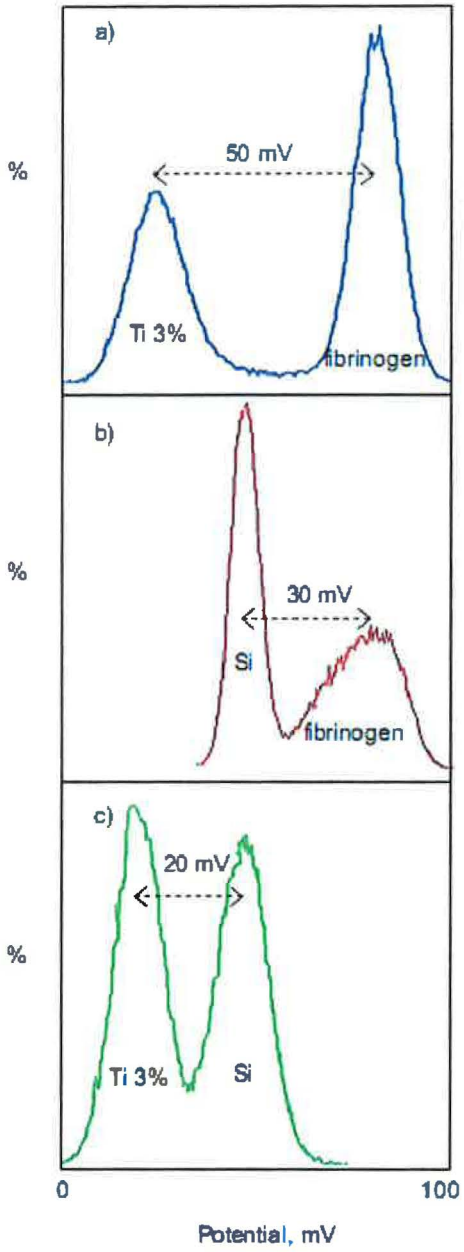

Fig. 3-23 The potential histograms: (a) fibrinogen on the 3% Ti/ppCH film; (b) fibrinogen on silicon and (c) the 3% Ti/CH film on silicon

The fibrinogen domains have different hydrophobic/hydrophilic properties and bear different charges. However the net charge of fibrinogen molecule is negative at neutral pH because it's IEP is 5.5 [108]. The effective adsorption of negatively charged fibrinogen on negatively charged surfaces regardless electrostatic repulsion has been reported in literature [108, 109]. In fact, the zeta potential of fibrinogen layer became less negative and even reversed the sign to positive values with increasing the protein concentration. It has been suggested that the driving force for fibrinogen adsorption was not of an electrostatic nature but rather hydrophobic

interaction and hydrogen bonding [108]. In such a model, fibrinogen forms the inner and outer layers. The inner layer is rich with negative charges and predominantly consists of hydrophobic species. The outer layer is rich with positive charges.

Later, the double layer concept was modified by Jung et al [110]. The authors considered the charges on particular domains of fibrinogen molecule. The D and E domains have the highest concentration of negative charge residues. The αC domains are rich with lysine and arginine side groups with pK_a 10.5 and 12.5, respectively. Hence, at neutral pH the αC domains are charged positively. These αC domains make weak electrostatic contact with negatively charged surface while the rest of the fibrinogen molecule resides on the αC intermediate layer and is not in direct contact with surface. Thus, the positively charged αC domains are screened by the negatively charged E and D domains.

In our case of Ti/hydrocarbon film, the adsorption of fibrinogen proceeds with formation of multiaggregates combining to the strands. In this process, the individual fibrinogen molecules take the comformations which ensure the positive net charge of fibrinogen layer with respect to both Ti/hydrocarbon and silicon. This comes in line with [108, 109] but contradicts the model by Jung et al [110]. Obviously, when fibrinogen adsorbs on the Ti/hydrocarbon film the positively charged αC domains stay exposed and the D and E domains which are more hydrophobic [110] interact with the surface via hydrophobic interactions and hydrogen bonding. An important note which should be addressed here is that amount of adsorbed fibrinogen is not a crucial parameter influencing the surface biocompatibility. Rather, the accessibility of peptide sequences responsible for interaction with platelet receptors must be considered [111]. The preferential orientation of fibrinogen domains during the protein adsorption may affect the accessibility of platelet binding moieties and thereby the fibrinogen activity. Taking this into account, it is of importance to establish orientation and conformation of adsorbing fibrinogen molecules.

It is also worth noting that in contrast to distinct pattern of fibrinogen strands on topography image almost none can be discerned on the KFM image. The fibrinogen strands and the regions between them are at the same potential which is higher than that of the Ti/hydrocarbon film. The most likely explanation is that the regions between the observable strands are also covered with fibrinogen molecules, yet they are buried in the outermost layer of the composite film. It has been shown recently that biomolecules can penetrate into the film of a plasma polymer when in solution [112]. The degree of accessibility depends on the swelling characteristics of the surface and is related in the case of plasma polymers with the extent of

cross-linking. It is reasonable to assume here that the surface network of the Ti/hydrocarbon film is sufficiently flexible in solution to embed fibrinogen molecules.

The cantilever amplitude image (Fig. 3-24a) shows a very strong contrast between the fibrinogen layer and the Ti/hydrocarbon film. Fibrinogen area appears darker which means that the cantilever responds the modulation less and supports the assumption that the protein layer is much softer.

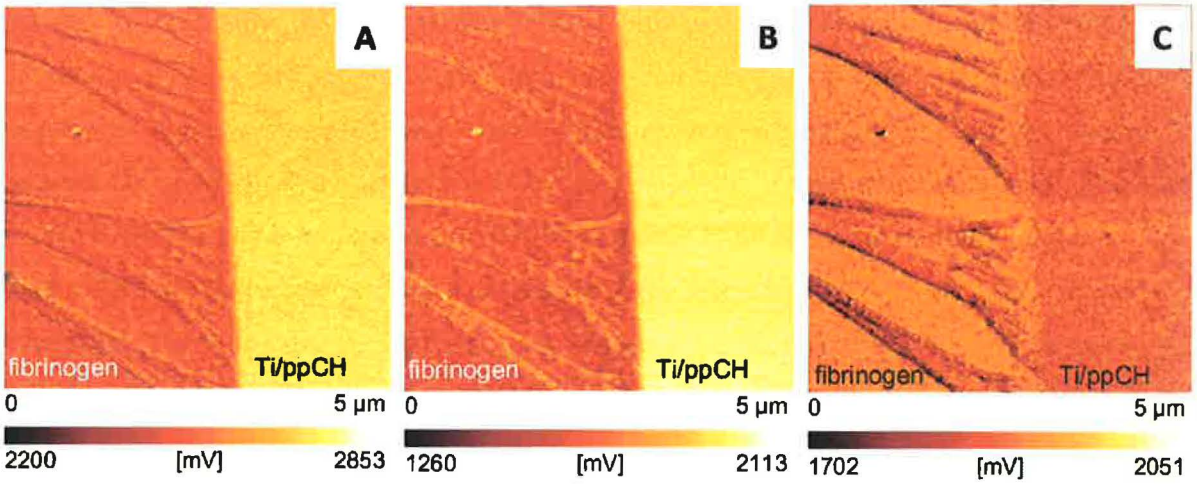

Fig. 3-24 The SPM images of fibrinogen adsorbed on 3% Ti/ppCH film: a) VE-AFM amplitude b) VE-AFM elasticity c) VE-AFM viscosity

The elasticity and viscosity components of the complex cantilever amplitude are shown on Fig. 3-24b, c. Both essentially match the corresponding topography and amplitude images, the viscosity image being inverted. In Fig. 3-24b the area covered by the fibrinogen layer appears darker and in Fig. 3-24c lighter than the Ti/hydrocarbon film. This means that fibrinogen is less elastic and more viscous than the Ti/hydrocarbon film. Considering the values of the complex amplitude with its real and imaginary parts it can be concluded that elastic response of fibrinogen is significantly stronger than viscous response. Indeed, the difference between the tip amplitude on the composite film and on the fibrinogen layer is 200 mV. The elasticity image shows 270 mV shift of amplitude between fibrinogen and the Ti/hydrocarbon film whereas the viscous component of the amplitude changes only by 90 mV, i.e. the energy stored within the fibrinogen layer during the sample excitation is significantly higher than the dissipated energy. In other words, fibrinogen is more elastic than viscous. Apparently, this is valid only under the given experimental conditions. No direct information, however, on the viscoelastic properties of fibrinogen under aqueous environment has been obtained yet. The time of transferring the samples from the solution to the SPM chamber was minimized so that the topography and KFM images were taken in first minutes after the contact of the sample

with air. The VE-AFM images, however, were acquired in 15-20 minutes after the sample exposure and the changes in viscoelastic properties following the spatial rearrangement of the protein subunits or even partial denaturation cannot be completely ruled out.

The VE-AFM results support the assumption of the buried fibrinogen layer as it was suggested by the KFM data. After the contact with fibrinogen solution the complete area including the area between the proteins strands exhibits lower elasticity and higher viscosity. This might be caused by the plasma polymer swelling effects without implementation of protein adsorption. However, after the treatment with fibrinogen solution the entire sample with treated and intact areas was thoroughly rinsed with water which obviously resulted in identical changes of viscoelastic properties throughout the Ti/hydrocarbon film. Hence, the formation of interfacial mixed layer of fibrinogen and plasma polymer appears to be the cause of such changes.

The adhesion between fibrinogen molecules and Ti/hydrocarbon films was studied by measuring the force-distance curves with fibrinogen modified tips. For this purpose, the cantilevers with silicon tip were successively cleaned with ethanol, water and UV-treatment. After the cleaning procedure the cantilevers were immersed into the 1 μg/ml solution of fibrinogen in PBS for 2 hours. In a separate QCM experiment analogous to [113], fibrinogen at such concentration has been found to form a monolayer on silica surface in less than an hour. After the incubation, the cantilevers were carefully rinsed with pure PBS and with Mill-Q water. The force-distance measurements were conducted in air immediately thereafter.

Fig. 3-25 shows the approaching and retracting curves for the Ti/hydrocarbon films with 3 and 20% of titanium. The retracting curve is not upright but exhibits a long-range nonlinear interaction between the tip and the surface. This is typical for the measurements with protein-covered tips [114]. Such a complex interaction of proteins with the surface over a long range is attributed to unfolding of the protein molecules and breaking of the multiple contact points during the withdrawal of the tip. The absolute value of adhesion force measured here is significantly higher than that usually measured under aqueous solutions. In humid air a water bridge builds up between the cantilever and the hydrophilic surface and the capillary forces are essentially responsible for the magnitude of the adhesion force. The larger adhesive jump in the retracting trace is observed for the film with 20% of titanium. Hence, adhesion of fibrinogen is stronger for Ti-rich surface.

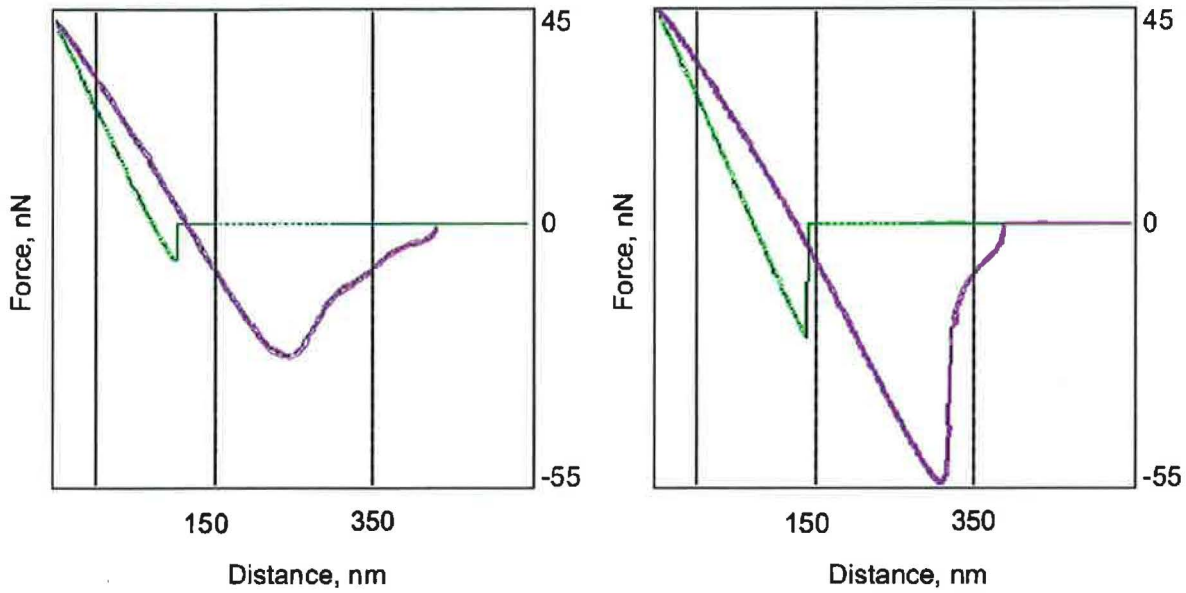

Fig. 3-25 The force-distance curves of fibrinogen modified tips against: a) the 3%Ti/hydrocarbon film b) the 20%Ti/CH film

3.1.5.2 Cell adhesion, growth and differentiation on Ti/hydrocarbon plasma polymer films

Human osteoblast-like MG 63 cells adhered and grew in a similar manner on all tested surfaces, i.e. on hexane-sputtered hydrocarbon plasma polymer films with less than 1 at.% of Ti, argon-sputtered hydrocarbon plasma polymer films with 20 at.% of Ti or on uncoated microscopic glass slides. They attached in similar initial cell numbers and by comparable cell-material contact areas (Fig. 3-26). As revealed by growth curves, their growth dynamics from day 1 to 7 after seeding was also similar (Fig. 3-26A).

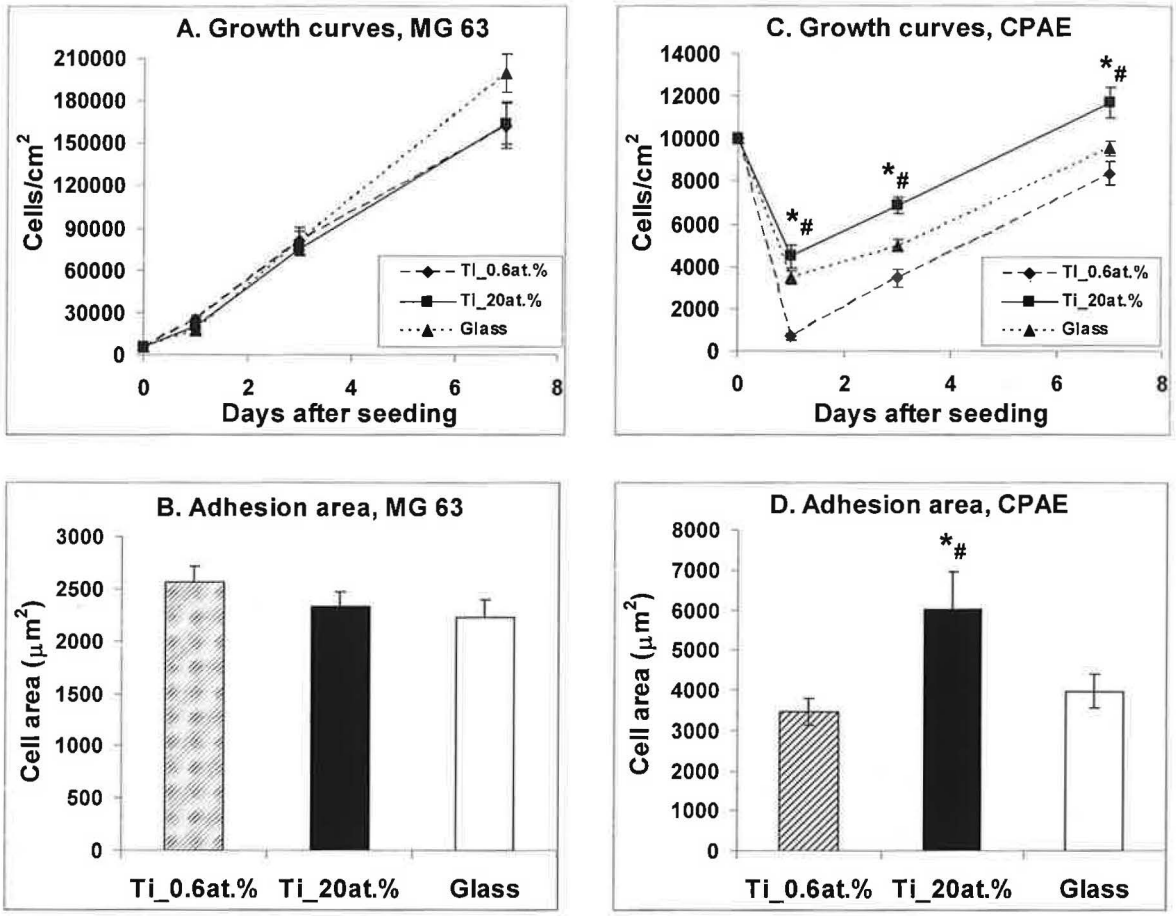

Fig. 3-26 Growth curves (**A, C**) and cell spreading area on day 1 after seeding (**B, D**) of human osteoblast-like MG 63 cells (**A, B**) or bovine pulmonary artery endothelial cells of the line CPAE (**C, D**) grown on microscopic glass slides coated with hexane-sputtered hydrocarbon plasma polymer films with 0.6 at.% of Ti (Ti_0.6at.%), argon-sputtered hydrocarbon plasma polymer films with 20 at.% of Ti (Ti_20at.%) or on uncoated microscopic glass slides (Glass).

Means ± SEM from 6 to 10 samples for each experimental group and time interval. ANOVA, Student-Newman-Keuls method; * and #: significantly different ($p \leq 0.05$) compared to Ti_0.6at.% and glass, respectively.

On all surfaces, the cells were of similar polygonal morphology or star-like shape with protrusions (Fig. 3-27). Cells on all tested surfaces displayed well developed strike-like focal adhesion plaques containing talin and localized preferentially at the cell periphery or at the ends of cell protrusions (Fig. 3-28). Osteocalcin, a marker of osteoblastic cell differentiation, showed homogeneous and fine-granular distribution in MG 63 cells on all studied surfaces (Fig. 3-29). The concentrations of talin and osteocalcin, measured by ELISA per mg of total cellular protein, were also comparable in cells growing on films with both lower and higher Ti

concentrations or on tissue culture polystyrene dishes, although the average values tended to be the highest in cells on films with 20 at.% of Ti (Fig. 3-30 A, B). Similar results were obtained earlier in bone marrow cells isolated from rat femur and tibia and cultured on amorphous hydrogenated carbon with 0 to 13 at.% of Ti or microscopic glass coverslips [115].

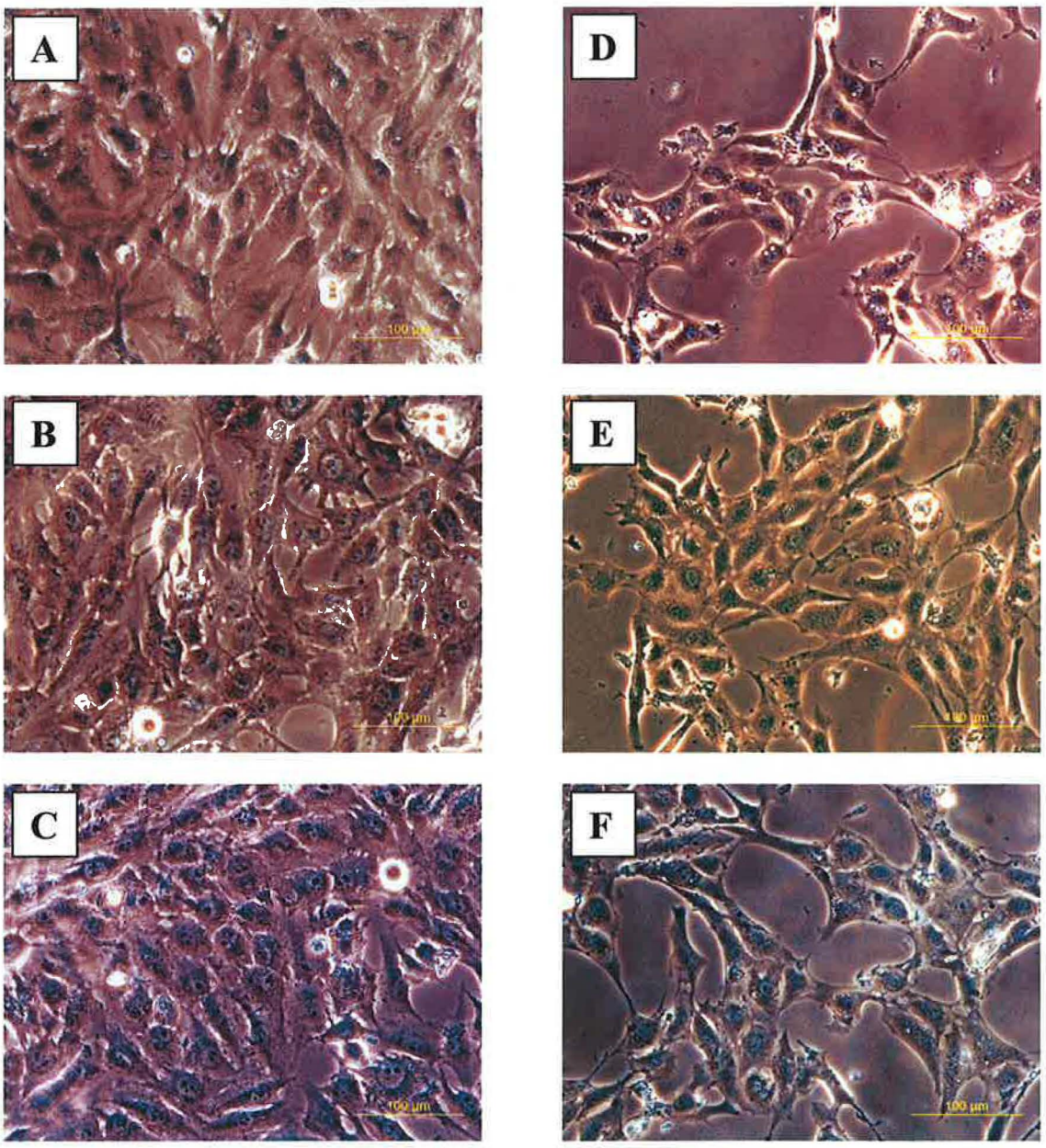

Fig. 3-27 Morphology of living human osteoblast-like MG 63 cells (A-C) or bovine pulmonary artery endothelial CPAE cells (D-F) on day 3 after seeding on microscopic glass slides coated with hexane-sputtered hydrocarbon plasma polymer films with 0.6 at.% of Ti (A, D), argon-sputtered hydrocarbon plasma polymer films with 20 at.% of Ti (B, E) or on uncoated microscopic glass slides (C, F). Microscope Olympus IX 50, digital camera DP 70, obj. 20x. Bar=100 μm.

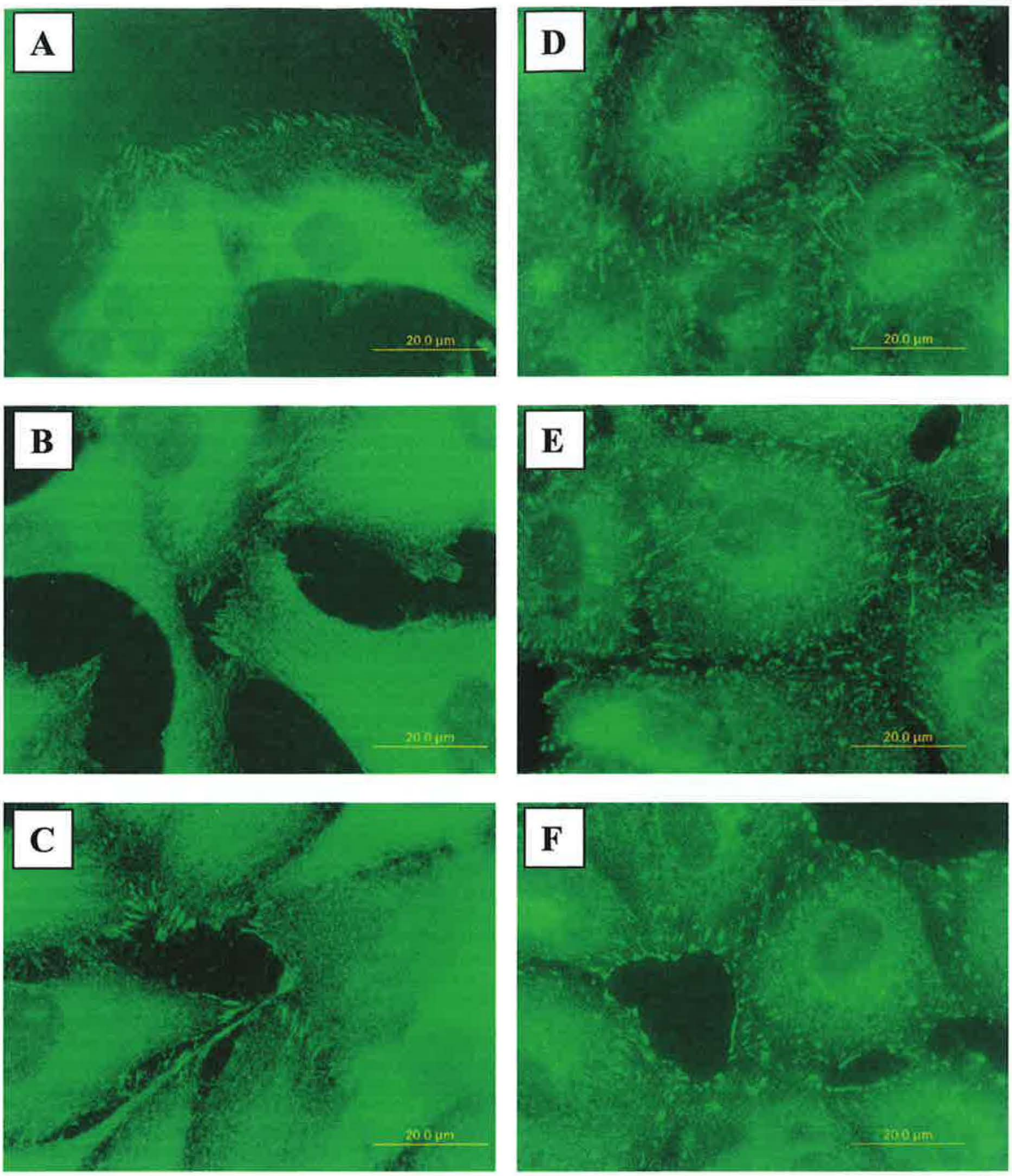

Fig. 3-28 Immunofluorescence of talin, a protein of focal adhesion plaques, in human osteoblast-like MG 63 cells (A-C) and bovine pulmonary artery endothelial cells of the line CPAE (D-F) on day 3 after seeding on microscopic glass slides coated with hexane-sputtered hydrocarbon plasma polymer films with 0.6 at.% of Ti (A, D), argon-sputtered hydrocarbon plasma polymer films with 20 at.% of Ti (B, E) or on uncoated microscopic glass slides (C, F). Microscope Olympus IX 50, digital camera DP 70, obj. 100x. Bar=20 µm.

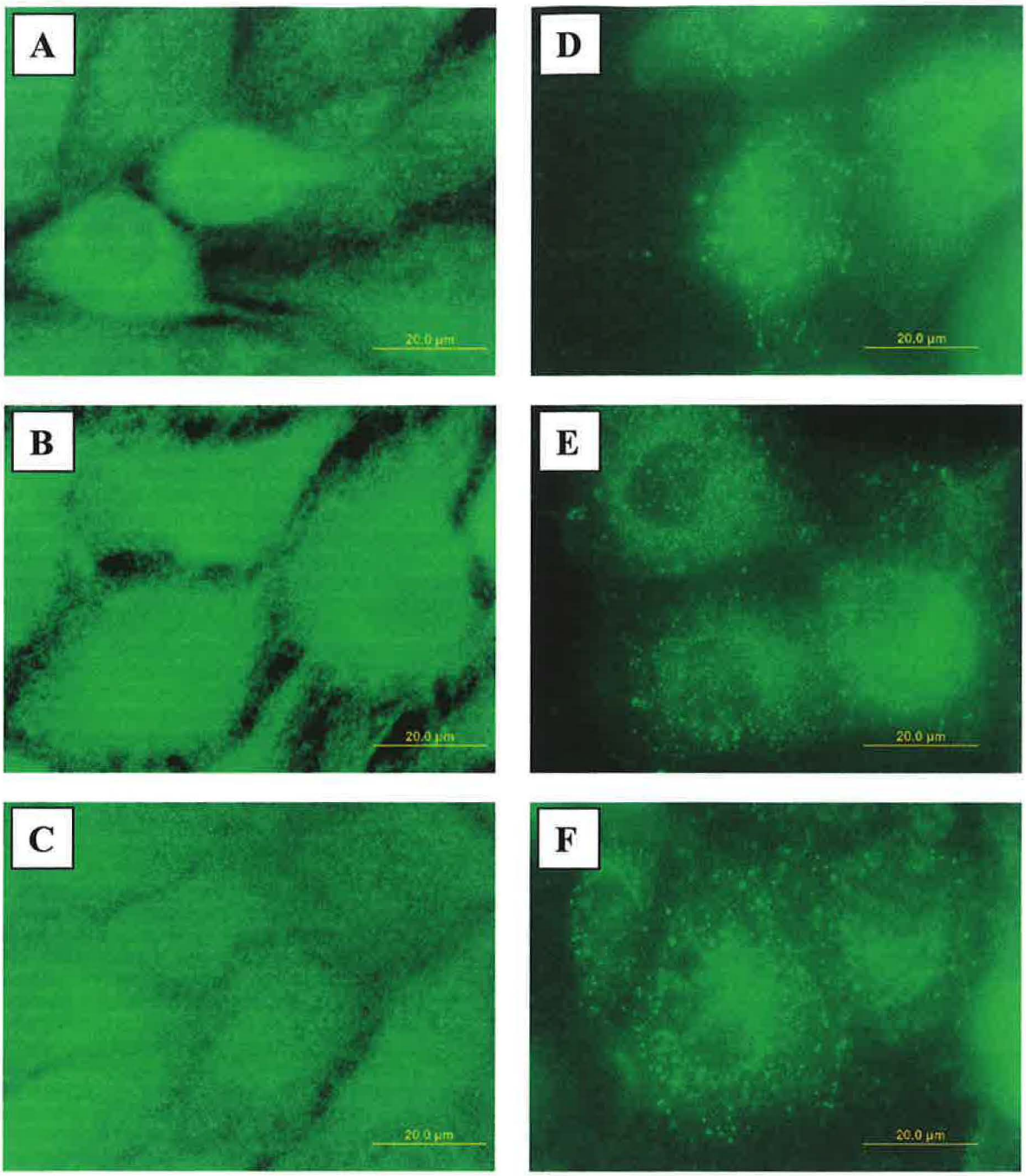

Fig. 3-29 Immunofluorescence of osteocalcin, a calcium-binding extracellular matrix protein and marker of osteogenic cell differentiation, in human osteoblast-like MG 63 cells (**A-C**), and von Willebrand factor, a hemocoagulation factor and a marker of vascular endothelial cell differentiation in bovine pulmonary artery endothelial cells of the line CPAE (**D-F**) on day 3 after seeding on microscopic glass slides coated with hexane-sputtered hydrocarbon plasma polymer films with 0.6 at.% of Ti (**A, D**), argon-sputtered hydrocarbon plasma polymer films with 20 at.% of Ti (**B, E**) or on uncoated microscopic glass slides (**C, F**). Microscope Olympus IX 50, digital camera DP 70, obj. 100x. Bar=20 µm.

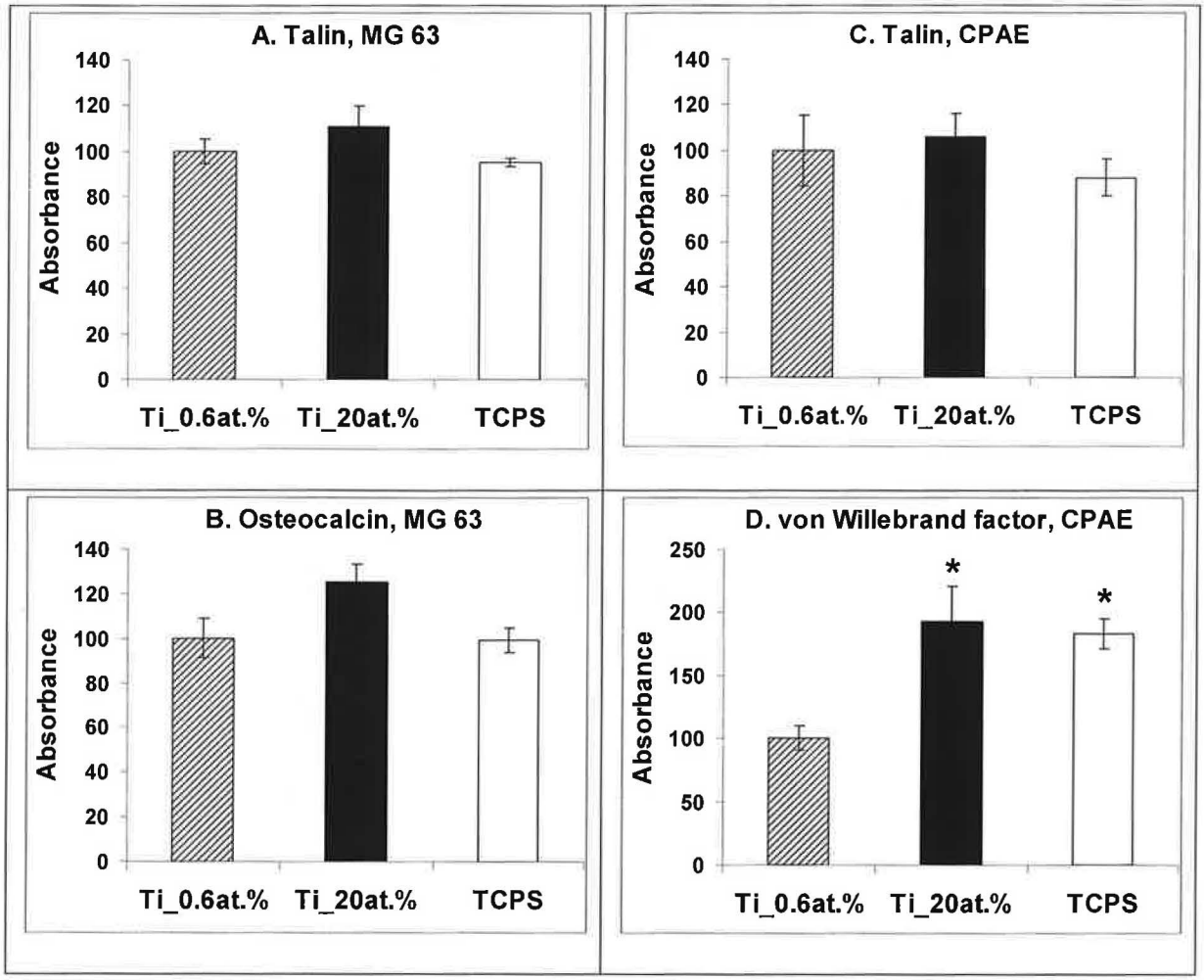

Fig. 3-30 Concentration of talin, a protein of focal adhesion plaques (A, C), osteocalcin, a calcium-binding extracellular matrix protein and marker of osteogenic cell differentiation (B) and von Willebrand factor, a hemo-coagulation factor and a marker of vascular endothelial cell differentiation (D) in human osteoblast-like MG 63 cells (A, B) or bovine pulmonary artery endothelial cells of the line CPAE (C, D) grown on tissue culture poly-styrene dishes coated with hexane-sputtered hydrocarbon plasma polymer films with 0.6 at.% of Ti (Ti_0.6at.%), argon-sputtered hydrocarbon plasma polymer films with 20 at.% of Ti (Ti_20at.%) or on pure tissue culture polystyrene dishes (TCPS).

Measured by ELISA per mg of protein. Absorbance values are expressed in % of values obtained from cell samples grown on Ti_0.6at.%. Means ± SEM from 6 to 8 samples for each experimental group. ANOVA, Student-Newman-Keuls method. *: significantly different ($p \leq 0.05$) compared to Ti_0.6at.%.

The morphology and lysosomal activity of these cells was similar and the activity of alkaline phosphatase, another marker of osteoblastic cell differentiation, tended to be higher in cells on the films with higher Ti concentrations. In contrast to our results, the number of bone marrow cells was significantly increased on Ti-containing samples compared to cells on glass [115]. This disproportion could be explained by a higher sensitivity of primocultured or low-pasaged bone marrow cells to different physical and chemical properties of the material surface in comparison with the line MG 63 used in our study, which is tumor-derived, highly passaged and well-adapted to long-term cultivation *in vitro* conditions. Similar higher sensitivity to roughness, topography and other physical and chemical surface properties was observed in our earlier study in rat vascular smooth muscle cells (VSMC) in low-passaged cultures on carbon fibre-reinforced carbon composites (CFRC) coated by carbon-titanium layer. The increase in cell adhesion and growth on Ti-containing surfaces was more pronounced in VSMC than in MG 63 cells [116].

However, in the present study, a higher responsiveness to the physicochemical properties of the material surface was found in the endothelial cells of the line CPAE, derived for the bovine pulmonary artery. On day 1, 3 and 7 after seeding, these cells reached significantly higher population densities on argon-sputtered films with 20 at.% of Ti compared to the values on hexane-sputtered films with less than 1 at.% of Ti and microscopic glass slide, and adhered by a significantly larger cell spreading area (Fig. 3-26C, D). The elongated or polygonal shape of endothelial cells on day 3 after seeding was similar on all tested surfaces (Fig. 3-27C, D). The concentration of talin was also similar, although the dot- and strike-like talin-containing focal adhesion plaques were slightly brighter on films with 20 at.% of Ti (Fig. 3-28 and Fig. 3-30C, D). Von Willebrand factor, a marker of endothelial cell maturation, was localized in well apparent dot-like Weibel-Palade bodies in cells on all studied surfaces (Fig. 3-29). However, its concentration was significantly higher in cells on Ti-rich than on Ti-deficient layers, and similar to the value found in cells grown on control TCPS surface (Fig. 3-30C, D).

The higher adhesion, growth and differentiation of CPAE cells on argon-sputtered layers could be attributed to the increased content of Ti (20 at.%). Titanium is known as highly biocompatible material promoting up-regulation of genes related to an increased metabolic activity of cells, such as genes encoding various receptors or proteins participating in exocytosis, vesicular transport and related to the cell membrane and actin cytoskeleton [117].
The argon-sputtered, Ti-rich films were also more wettable. Their static water drop contact angle was less than 10°. On the contrary, it reaches 86° for the film deposited in pure hexane.

A higher wettability of the Ar-sputtered film can be explained by an increased content of oxygen (11 at.%) in a form of TiO, TiO_2 and oxygen-containing chemical functional groups, such as C-O, C=O and O-C=O. The increased oxygen content and wettability of the material surface is usually associated with adsorption of cell adhesion-mediating molecules (mainly vitronectin and fibronectin) from the serum of the culture media in a flexible form enabling good accessibility of specific sites on these molecules by cell adhesion receptors, e.g. integrins [118]. In our earlier experiments, the creation of oxygen-containing groups on polystyrene irradiated by fluorine ions and its increased wettability were associated with increased adhesion, growth and maturation of vascular smooth muscle and endothelial cells in cultures on the polymer [96, 97].

Another factor highly contributing to the increased adhesion and other functions of cells on solids is surface roughness. Nanostructured materials mimic the nanoarchitecture of the natural tissues (e.g., nanoscale loops of the extracellular matrix molecules, nanoscale organization of the cell membrane etc.), which further contributes to the adsorption of cell adhesion-mediating molecules in a spatial conformation advantagous for their accessibility by cell adhesion receptors. Nanophase titania added to poly-lactide-*co*-glycolide scaffolds developed for bone tissue engineering markedly increased adhesion, growth, alkaline phosphatase activity and calcium deposition in a human osteoblast cell line in comparison with conventional titania grain of the size in micrometers [119]. Nanostructured titanium dioxide ceramics promoted formation of vinculin-containing focal adhesion complexes in cultured rat cardiomyocytes, and maintained the differentiated phenotype of these cells [120]. In our case, both Ti-deficient and Ti-rich films deposited on polished silicon, glass and polystyrene dishes were of similar nanoroughness (1-6 nm RMS) as measured by the AFM on the 1x1 μm images. No dependence of roughness on deposition conditions was detected. Hence, it seems that the observed differences in the behavior of endothelial cells on the films were governed primarily by surface chemistry. Similarly, fibroblasts, chondrocytes and smooth muscle cells were influenced by the surface chemistry and energy rather than the fiber dimensions [121]. Another line of human bone-forming cells (ATCC CRL-11372) in cultures on supports made of carbon and polymeric fibers reacted primarily to the substrate nanostructure. This different responsiveness of various cell types has been explained by enhanced adsorption of vitronectin on nanostructured materials and its specific spatial conformation, recognized preferentially by osteoblasts [121].

On day 7, the endothelial cells on all surfaces were able to develop a confluent layer of cobblestone-like appearance, typical for maturing endothelial cells (Fig. 3-31). Thus, it can be

concluded that our newly developed nanocomposite Ti/hydrocarbon plasma polymer films from reactive magnetron sputtering in both hexane and argon are suitable growth supports for bone-forming and vascular endothelial cells. These films could be used for increasing the biocompatibility and bioactivity of bone implants in which good integration with the surrounding bone tissue is desirable. For example, these coatings could be deposited on the bone-anchoring stems of joint prostheses. In addition, these nanofilms, especially those with higher, i.e. 20 at.% Ti concentration, might be applicable for supporting endothelialization of artificial valves, stents or even inner surface of blood vessel prostheses. Coating artificial blood-contacting devices with a confluent and mature endothelial cell layer is considered as the best protection of these devices against hemocoagulation [97, 122, 123].

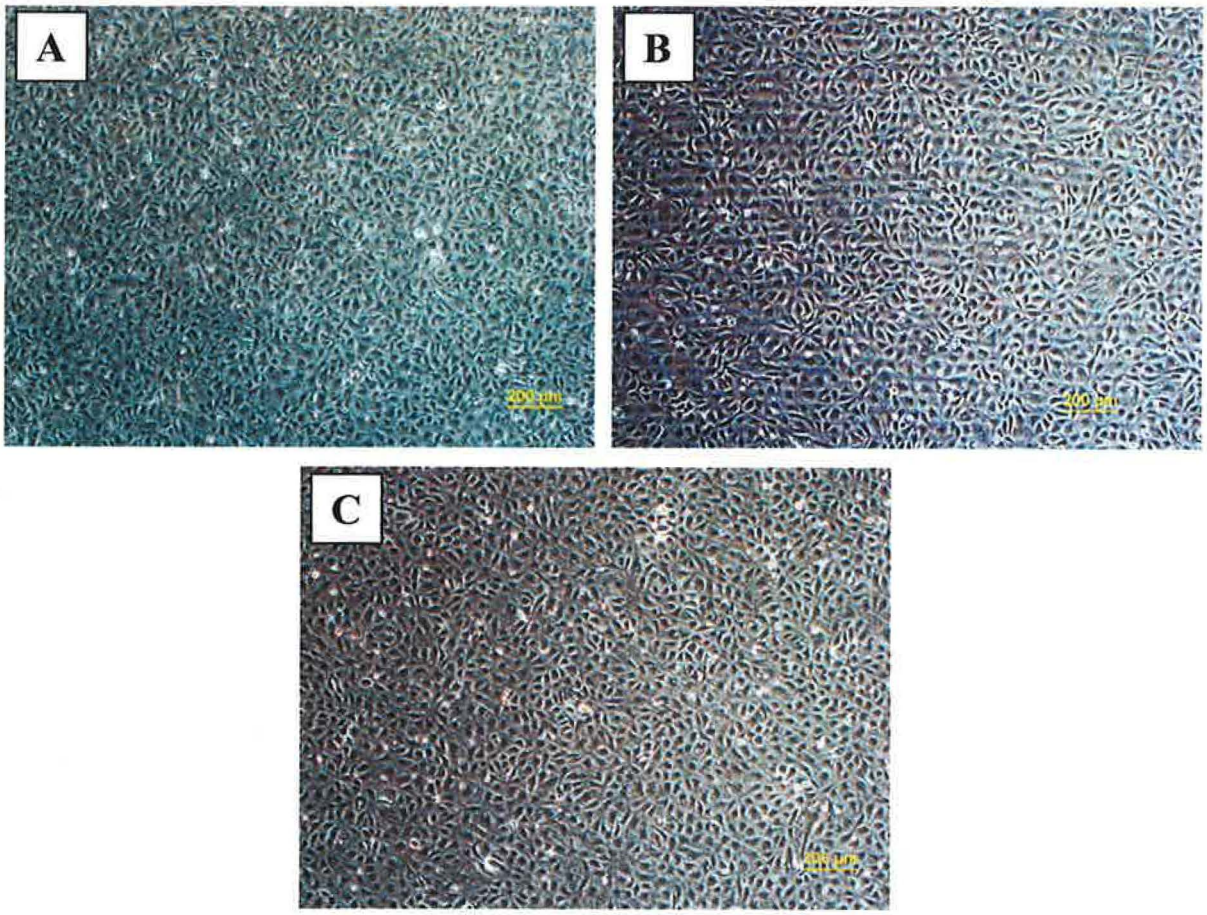

Fig. 3-31 Morphology of living bovine pulmonary artery endothelial cells of the line CPAE on day 7 after seeding on a glass slide coated with a-C:H (**A**), a-C:H with 20 at.% of Ti (**B**) and pure glass slide (**C**). Microscope Olympus IX 50, digital camera DP 70, obj. 4x. Bar=200 μm.

3.2 Polypropylene treatment by O_2 plasma

3.2.1 Motivation of polymer foil modification is plasma

In biomedical applications it is often needed to increase surface energy of a polymeric solid in order to improve wettability of this surface. This is usually done in low pressure plasma containing oxygen or air and it can also be done in atmospheric pressure discharge such as corona.

In this study we decided to investigate modification processes on polypropylene surface when subjected to DC discharge in oxygen and water vapor plasma. Also flowing afterglow plasma experiments were explored.

In previous studies water vapor was added into argon DC discharge for the improvement of wettability of hydrocarbon plasma polymer [124]. In another study PP foil surfaces were subjected to the fluence of oxygen cluster ions and the modification effect was studied by XPS, AFM and contact angle measurements [125].

Surface oxidation of polymers by means of high energy chemistry methods has been developed several decades ago. Five gas-phase processes are mainly used for the purpose of surface modification including flame, corona discharge under atmospheric pressure (more correctly, dielectric barrier discharge), low-pressure plasma of DC or RF discharges in oxygen or air, and comb ined ozone–UV irradiation [126]. All these processes result in different polymer surface oxidation effects. In the case of low-pressure plasma, corona, and ozone - UV irradiation, the formation of low molecular weight oxidized products was observed as a result of polymer chain scissions [127, 128]. These products remain adsorbed on the surface but can be easily removed by washing with water. Otherwise, the low molecular weight species may further interact with the plasma through formation of gaseous products; this leads to so-called polymer etching [129]. An ox idation mechanism has been proposed [128] as a result of computational modeling of reaction kinetics in the corona and in the flame. It was proposed that the process starts with hydrogen abstraction in the reactions $RH+O \rightarrow R^{\cdot}+{}^{\cdot}OH$ and $RH+{}^{\cdot}OH \rightarrow R^{\cdot}+H_2O$. The subsequent development of the process depends on the proportion between the oxidative species. In the case of predominating atomic oxygen, alkoxy radicals are mainly formed in reactions between atomic oxygen and alkyl radicals. The alkoxy radicals so formed are further decomposed through polymer chain scission, which results in the formation of low molecular weight oxidized products. If molecular oxygen is predominant, the prevalent species are peroxy radicals formed in the reaction $R^{\cdot}+O_2 \rightarrow ROO^{\cdot}$. Subsequent

reactions lead to the formation of various oxygen-containing functional groups without substantial polymer chain scission. Strobel et al. [128] suggested that this mechanism was plausible for flame treatment where the OH and O_2 were the main components. In other cases, however, the important species was atomic oxygen. But it is known that spontaneous dissociation of an alkoxy radical is endothermic and has rather high activation energy. For this reason, it was proposed that oxidative thermal destruction of polyolefins occurs at temperatures lower than 140°C via monomolecular synchronous destruction of peroxy radicals rather than alkoxy ones (Scheme 3-1) [130].

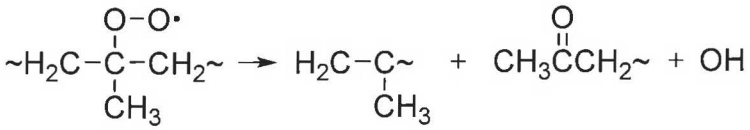

Scheme 3-1 Monomolecular destruction of peroxy radicals

Another hypothesis was proposed in a study by Dorofeev [131]. The main idea is that atomic oxygen is not only the initiator of hydrogen abstraction but also its exothermic reaction with oxygen-containing radicals including peroxy ones results in polymer chain scission and etching. For example see Scheme 3-2, Scheme 3-3.

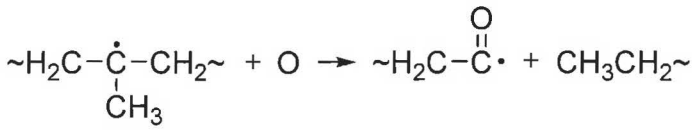

Scheme 3-2 Polymer chain scission under the action of atomic oxygen

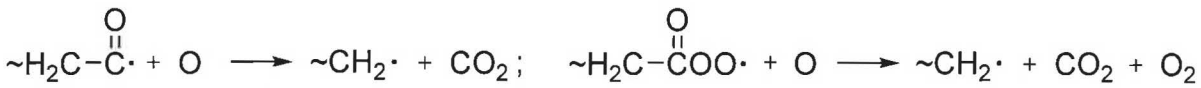

Scheme 3-3 Etching process with participation of atomic oxygen

Such reaction mechanisms, in which atomic oxygen simultaneously participates in both formation and destruction reactions, can probably limit the extent of surface oxidation and the depth of the oxidized layer in the case of the application of air corona [132], oxygen low pressure plasma [133], and UV irradiation [134]. That supposition was experimentally confirmed in the study by Shikova et al. [135], in which it was shown that the joint action of the atomic oxygen, O_2 metastable ($a^1\Delta_g$) and ground ($X^3\Sigma_g$) states in flowing afterglow of O2 discharge onto the polyethylene surface resulted in simultaneous surface oxidation and etching, while the action of metastable ($a^1\Delta_g$) and ground ($X^3\Sigma_g$) states resulted mainly in the oxidation.

In the afterglow, the etching rates were lower than in plasma and no formation of end double bonds as a result of chain scission was observed. Furthermore, an additional way to stimulate the etching process in plasma can involve an UV irradiation. As shown in studies [136, 137], the joint action of atomic oxygen and UV irradiation leads to a much greater increase in etching rate than individual actions of either of them.

If, instead of molecular and atomic oxygen, the dominating species is OH then according to the suggestion of study [128] it can be expected that the surface will be rich in hydroxyl groups. The problem of obtaining monotype functional groups is also important [138]. Although water plasma studies are rather limited, it is known that besides water the main neutral components of this plasma are H_2 and O_2 molecules and OH and H radicals [139]. Therefore, gas discharge in water vapor and in its flowing afterglow seems to be promising. For this reason, the main goal of this work was to study the influence of different oxidative environments with respect to the poly(propylene) (PP) modification.

3.2.2 Diagnostics of modification process

An overview of the water vapor spectrum is presented in Fig. 3-32a. The most intensive lines were H_α(656 nm), H_β(434 nm) and OH($A^2\Sigma \rightarrow X^2\Pi$) bands whereas only weak lines of OI($3p^3P \rightarrow 3s^3S$, 845 nm) and OI($3p^5P \rightarrow 3s^5S$, 777 nm) were observed. No bands of molecular oxygen and hydrogen were detected. It seems that under these conditions any process of dissociative excitation by electron impact is improbable because of the high threshold energy

$$H_2O + e \rightarrow OH(A^2\Sigma) + H(^2S) + e, \varepsilon_{ex} \approx 9.2\text{eV};$$

$$H_2O + e \rightarrow OH(X) + H(3p^2P) + e, \varepsilon_{ex} \approx 17.1\text{eV};$$

$$H_2O + e \rightarrow H_2(X) + O(3p^5P) + e, \varepsilon_{ex} \approx 15.7\text{eV}.$$

The stepwise processes of $H_2O+e \rightarrow OH+H$ or H_2+O ($\varepsilon_{ex} \approx 5$ eV) type, with subsequent reactions

$$O(^3P) + e \rightarrow O(3p^{5,3}P) + e \ (\varepsilon_{ex} \approx 10.7 \text{ eV}),$$

$$H + e \rightarrow H(3p^2P) + e \ (\varepsilon_{ex} \approx 12.1 \text{ eV}),$$

$$OH(X) + e \rightarrow OH(A^2\Sigma) + e \ (\varepsilon_{ex} \approx 4.1 \text{ eV})$$

are more probable in this case. The excitation energies of the OI($3p^{5,3}P$) from the ground state are lower than for the H($3p^2P$) and the electron impact cross-sections are of the same order of

magnitude [140, 141]. Therefore, $O(^3P)$ concentration has to be substantially lower than that of $H(^2S)$.

In the oxygen plasma (Fig. 3-32b), only the OI lines and a single band of $O_2(b^1\Sigma_g^+ \rightarrow X^3\Sigma_g^-$, 0-0, 762 nm) were present in the range of 200-1000 nm. The 845, 777 nm lines were the most intensive. Intensities of other lines of quintet (645.616, 926 nm) and triplet (700,725,822 nm) transitions were markedly lower. Hence, atomic oxygen and O_2 singlet metastable molecules are the main active species in this case.

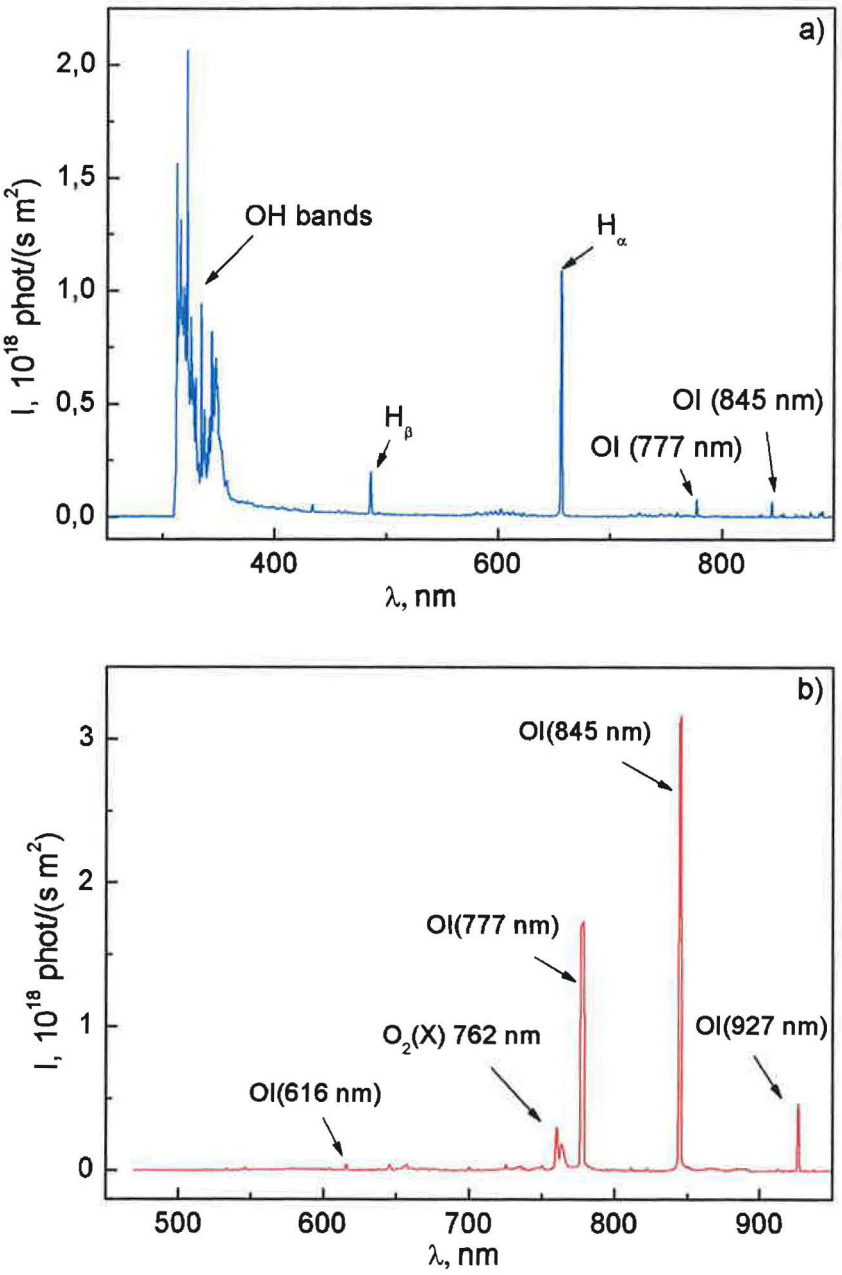

Fig. 3-32 Overview of a) water vapor, b) oxygen plasma discharge spectrum.

3.2.3 Film analysis

3.2.3.1 XPS analysis

The XPS analysis was performed on pristine PP surface and on the samples treated in the afterglow of the water vapor discharge. The spectrum of pristine PP is dominated by carbon (99.5 at. %) with small traces of oxygen (0.5 at. %). After 5 minutes of the treatment in the afterglow, the surface concentration of oxygen significantly increases to 7.0 at. % and the carbon content correspondingly decreases to 93.0 at. %. Obviously, the afterglow treatment favors the incorporation of oxygen into the PP surface. This is further supported by the comparison of the high-resolution XP spectra (Fig. 3-33).

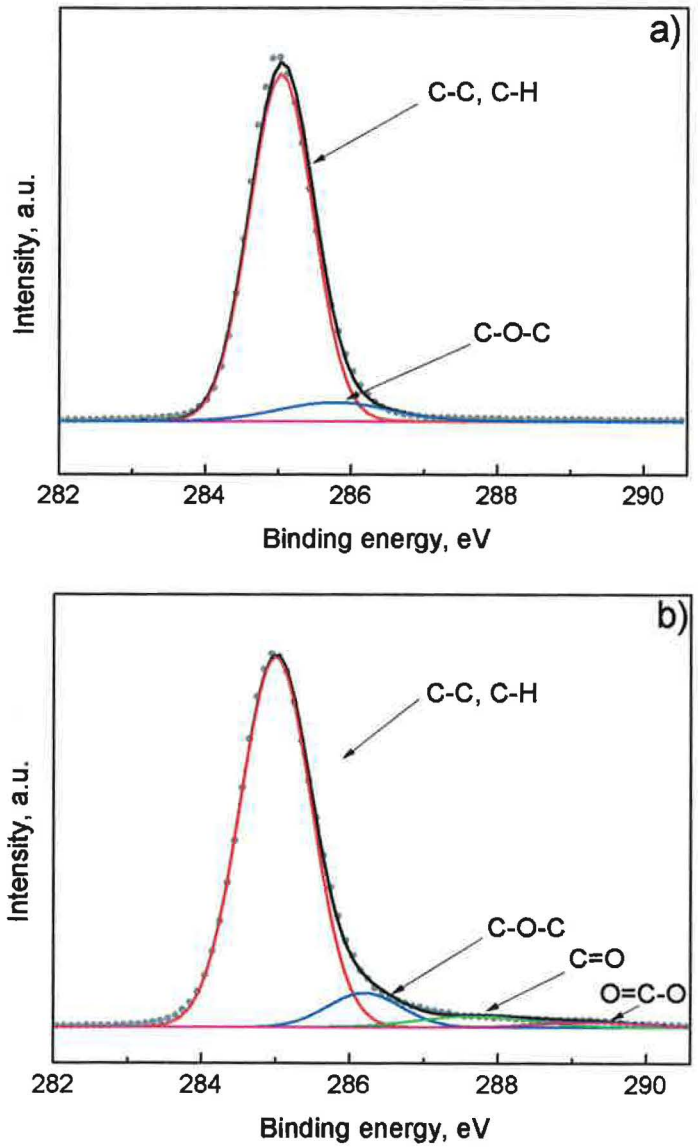

Fig. 3-33 The XPS of a C1s core level of a) untreated PP and b) PP treated in afterglow of water vapor discharge during 5 min

The presence of a small amount of oxidized carbon in pristine PP is indicated by asymmetry at the higher binding energy side which can be seen in the C 1s spectra (Fig. 3-33a). Such asymmetry is attributed to a component with binding energy 1.3 eV higher than the primary aliphatic component. The position of this component allows us to assign it to the C-O-C binding environment. For the sample treated in the afterglow an enhanced oxidation is manifested by both the increase of the signal from oxygen (Fig. 3-34) and the broadening of the C 1s XPS signal (Fig. 3-33b). The total Full-Width-at-Half-Maximum (FWHM) of 1.2 eV is higher than that of the pristine PP peak (1.0 eV) and additional components had to be added to the deconvolution to obtain a reasonable fitting. These are located at 287.8 and 289.3 eV and were assigned to carbonyl (C=O) and carboxyl (COO) based species. Hence, the XPS results are consistent with the FTIR data showing an increase of highly oxidized carbon species after the treatment in the afterglow of the water vapor discharge.

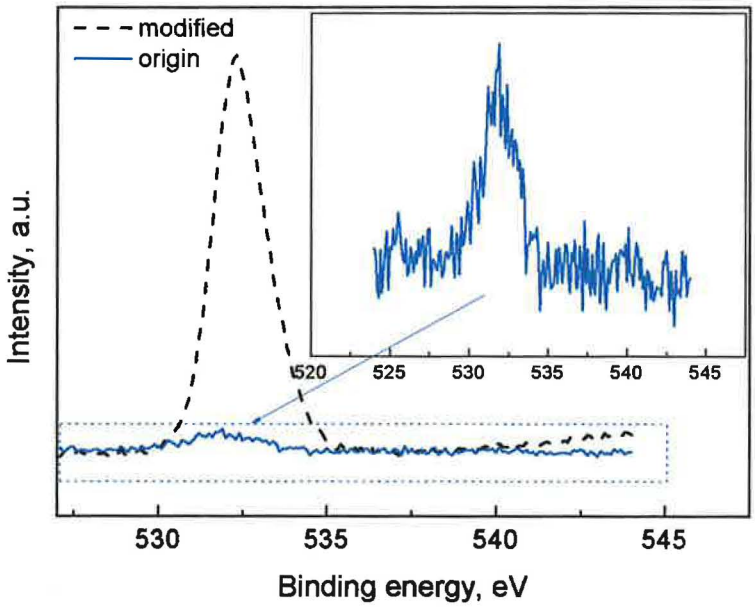

Fig. 3-34 The XPS of an O1s core level of PP treated in afterglow of water vapor discharge for 5 min

3.2.3.2 ATR-FTIR analysis

It was rather surprising that regardless of the significant difference in the composition of active species between H_2O and O_2 plasmas the ATR-FTIR spectra of the PP samples were very close both qualitatively and quantitatively. Fig. 3-35a-c present the differential spectra obtained by subtraction of the virgin spectrum from the treated one. The action of both types of plasma leads to the formation of the end double bonds of vinyl (910 cm^{-1}) or vinylidene

(889 cm^{-1}) type (Fig. 3-35a). These bonds are always formed as a result of chain scission and polymer degradation during the action of low pressure oxygen plasma [133], VUV [142] and in auto-oxidation processes [143]. The absorbance value of these bands for both oxygen and water vapor plasma was approximately the same. The action of both oxygen and water plasma results in the formation of a broad set of C=O groups with various overlapping bands located in the wavenumber range from 1550 up to 1850 cm^{-1} (Fig. 3-35b). These bands can be attributed to esters, ketones, unsaturated ketones, aldehydes, oxyketones and carboxylic acids. The spectra in Fig. 3-35c show an increase of the absorption bands of the OH-groups (3100-3700 cm^{-1}). Absorption intensities are also increased in the region between 900 and 1400 cm^{-1} where the bands of O-H deformation vibrations and C-O stretching vibrations are located (not shown).

Unlike the plasma action, the treatment in flowing afterglow of water vapor discharge during the same period of time leads to the formation of a more homogeneous composition of C=O groups as can be seen from Fig. 3-35b. Moreover, for afterglow the absorbance of both OH and C=O groups is about one order of magnitude higher. However, the absorption bands related to the end double bonds of vinyl or vinylidene were not observed (Fig. 3-35a).

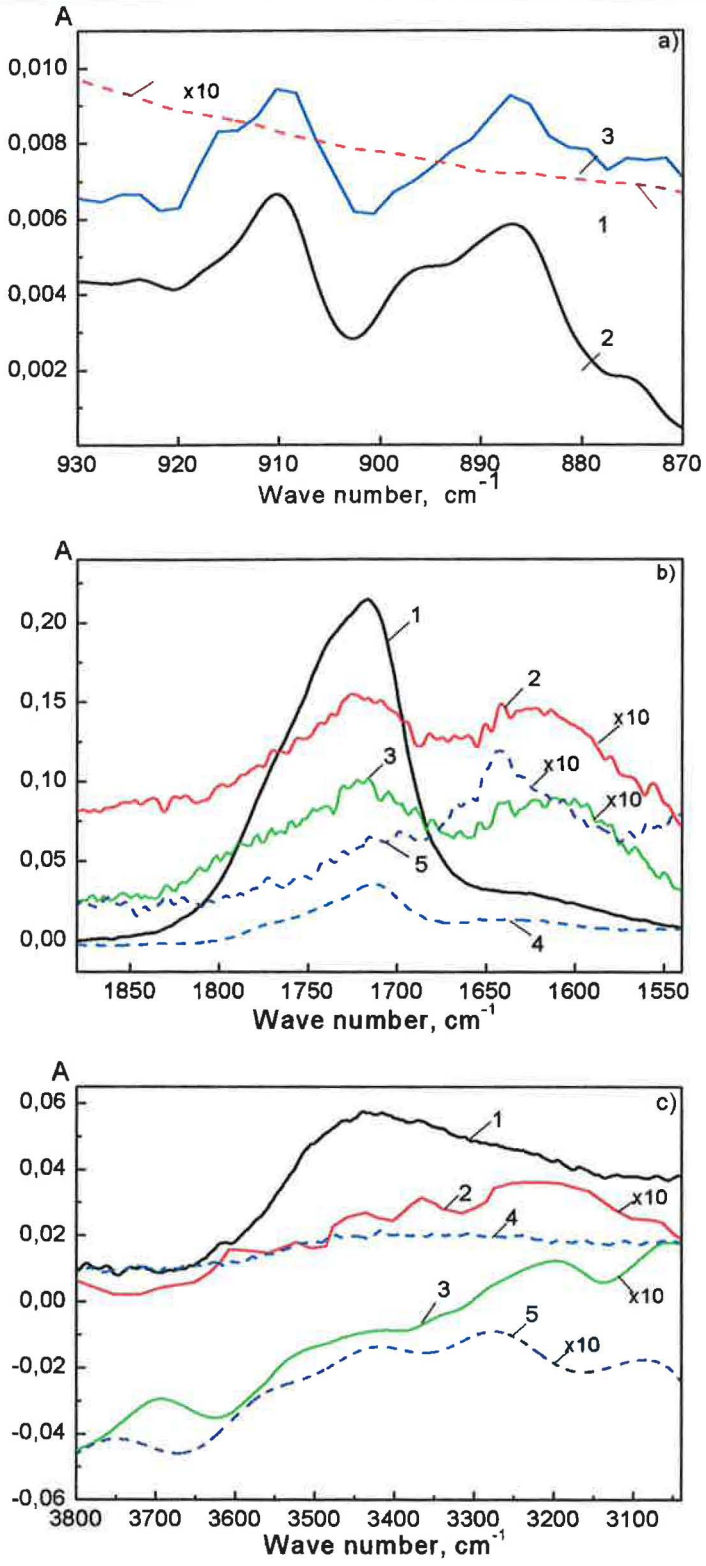

Fig. 3-35 Differential spectra of the PP samples in the range of: a) vinyl (910 cm^{-1}) and vinylidene (889 cm^{-1}) double bonds, b) various carbonyl groups, c) hydroxyl groups after 5 min of treatment.

1 – afterglow of water vapor plasma, 2 – oxygen plasma, 3 – water vapor plasma, 4 – after water vapor plasma afterglow treatment and washing, 5 - after water vapor plasma treatment and washing. A is the optical density.

3.2.3.3 Surface analysis

The AFM data confirm the etching process (Fig. 3-36). After the action of afterglow active species the polymer surface becomes smoother and homogeneous. Compared with the virgin sample, both the mean height of roughness and root-mean-squared roughness (the value of standard deviation of height) essentially decreased.

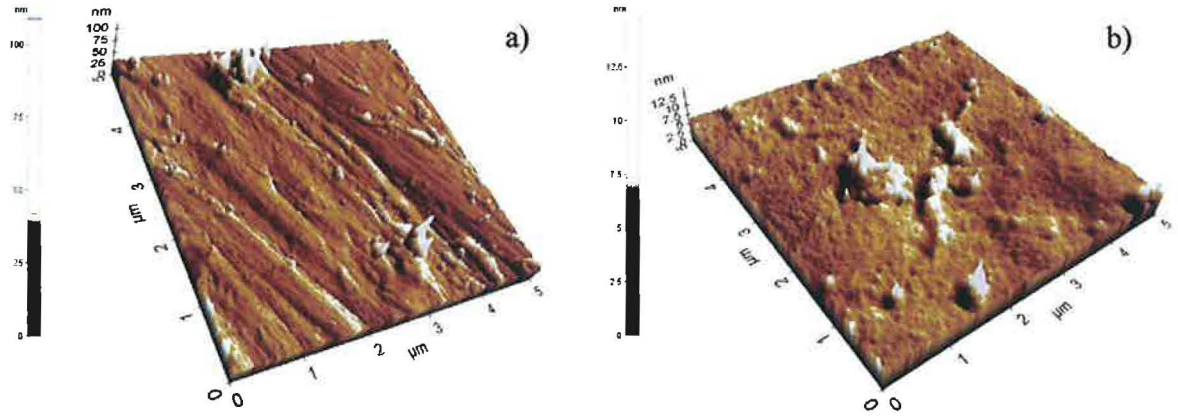

Fig. 3-36 Surface topology of: a) virgin PP sample, b) PP sample treated during 5 min in water vapor plasma afterglow

Minimal height of roughness is R_{min}=21 nm and 4 nm, maximal height of roughness is R_{max}=47 nm and 10 nm, mean roughness is R_m=34 nm and 7 nm, root-mean-squared roughness (the value of standard deviation of height) is R_q=3 nm and 0.7 nm respectively for virgin PP and treated one.

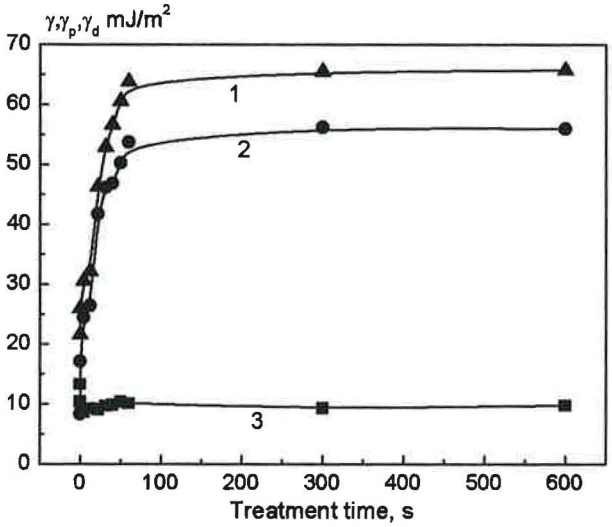

Fig. 3-37 Current changes of surface energy and its components under the treatment in water vapor plasma flowing afterglow. 1 – total surface free energy, 2 – polar component, 3 – dispersion component.

As shown in Fig. 3-37, the PP treatment also results in an increase of surface free energy, γ. The main contribution of γ increase comes from its polar component γ_p. It is necessary to point out that the saturated value of γ for both plasmas and afterglow treatment was approximately the same. The γ value leveled off over the time of ~100 s. In contrast, the leveling time of the FTIR absorbance of oxygen-containing groups was substantially longer, as seen in Fig. 3-38. Because the analysis depth for IR is about 1 μm we suppose that in the case of the afterglow treatment the oxidation processes propagate deeper into the sample bulk compared with plasma action due to a lower ratio between etching and oxidation rates. As a result, a longer time is required to attain a stationary state for oxygen-containing groups. It is worth noting that the samples have gained specific interference coloration after the treatment.

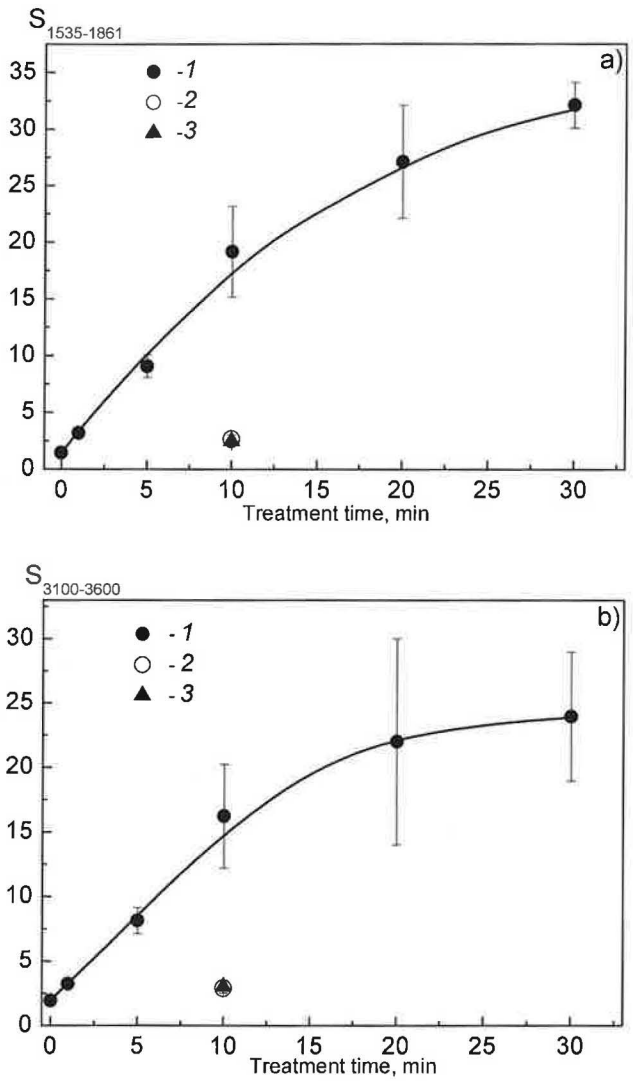

Fig. 3-38 Optical densities of different: a) carbonyl groups and b) hydroxyl groups versus treatment time.

Densities were obtained by means of integration over the 1535-1861 cm^{-1} range. 1 – afterglow, 2 – oxygen plasma, 3 – water vapor plasma.

3.2.4 Possible explanations

It is rather difficult to explain the above results in terms of the process mechanism because the exact composition of the active species reaching the sample is unknown. Nevertheless, some estimation is possible. We can at least assert that the action of VUV radiation and charged particles in the afterglow is excluded. The end double bonds of vinyl and vinylidene type are probably formed during the plasma treatment due to the action of the plasma agents mentioned above. According to the study [144], the water dissociation degree is about 40% under our experimental conditions. Assuming that the water molecules dissociate in accordance with their stoichiometry, at a temperature of 343 K and a pressure of 100 Pa the concentration of H_2O, O_2 and H_2 will be 1.3×10^{16}, 2.8×10^{15} and 5.6×10^{15} cm^{-3}, respectively. The concentration of the O, OH and H radicals is expected to be at least less than O_2 and H_2. The characteristic time of particle transportation from plasma to the sample over the afterglow zone is $\tau_T = L/V = 6/50$=0.12 s, where L is the distance between plasma and the sample (please see Fig. 2-2). The typical value for the diffusion coefficients of gases D is about 400 cm^2/s [145]. The characteristic diffusion time is $\tau_D \approx L^2/D = 0.09$ s. Therefore, the transport process is accomplished by means of diffusion and convection. On comparing the characteristic time of reaction with the times mentioned above it is possible to estimate the reduction of the concentration of various active species during their transportation over the afterglow zone. The characteristic time of heterogeneous destruction can be estimated as $\tau_g = 2R/(\gamma V_t)$, where R =1.5 cm is the discharge tube radius, $V_t = \sqrt{8kT/\pi m}$ the average thermal velocity and γ the probability of heterogeneous destruction (the typical value of which for the afterglow is ~10^{-4}-10^{-5}). Taking the γ value of 10^{-4}, we obtained $\tau_g \approx 0.44$ s. Therefore, $\tau_D / \tau_g \approx$20% of the initial particle concentration will be lost heterogeneously. The reactions between O, OH, H, H_2, and O_2 particles were well studied in a so-called combustion process [146]. Under low pressure, three-body reactions are not effective. Among two-body reactions, the most important are the following:

$O+H_2 \rightarrow OH+H$ (5×10^{-17} cm^3/s) (1) $O+OH \rightarrow O_2+H$ (2.8×10^{-11} cm^3/s) (2)

$O_2+H \rightarrow OH+O$ (2.1×10^{-20} cm^3/s) (3) $H+H_2O \rightarrow OH+H_2$ (2.9×10^{-23} cm^3/s) (4)

$OH+H_2 \rightarrow H_2O+H$ (1.5×10^{-15} cm^3/s) (5) $OH+OH \rightarrow H_2O+O$ (1.7×10^{-12} cm^3/s) (6)

where the values in the brackets correspond to the reaction rate constant calculated at 343 K for the data from study [146].

The loss of O, H radicals in reactions (1), (3) and (4) is negligible because the appropriate lifetime of these particles is more than one order of magnitude longer than τ_D and τ_g. The lifetime of OH in reaction (5) is 0.12 s and is comparable with τ_D. Unfortunately, the exact concentration of OH radicals is unknown. Supposing that the OH lifetime in reaction (6) is the same as in reaction (5) we obtain an OH concentration of 5×10^{12} cm^{-3}. This value is quite reasonable. In this case, reaction (2) is the main process of decay of the O atoms which gives the O atoms a lifetime of $\sim7\times10^{-3}$ s. Taking into consideration that O atom concentration in plasma is much less than OH, we can conclude that reaction (6) is the main process of O atom formation in the afterglow and these atoms are transformed quickly by reaction (2) forming O_2 and H. This analysis shows that the OH concentration must drop substantially, at least no less than two times, during the transport through the afterglow zone. The main active products of OH transformation are H radicals and O_2 molecules. The change in the concentration of H radicals has to be the least. Under a deficit of atomic oxygen and hydroxyl radicals it is quite possible that H radicals can be the main initiating agents instead of OH and O. The H radicals can react with PP (Scheme 3-4), with successive reactions of an alkoxy radicals formation (Scheme 3-5).

Scheme 3-4 Alkyl radical formation under the action of atomic hydrogen

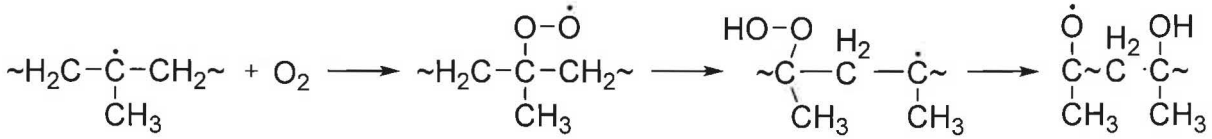

Scheme 3-5 Formation reactions of alkoxy radical and OH groups

The decomposition of alkoxy radicals results in polymer chain scission, formation of C=O and OH groups, end radicals, and low molecular weight oxidized products (Scheme 3-6, Scheme 3-7).

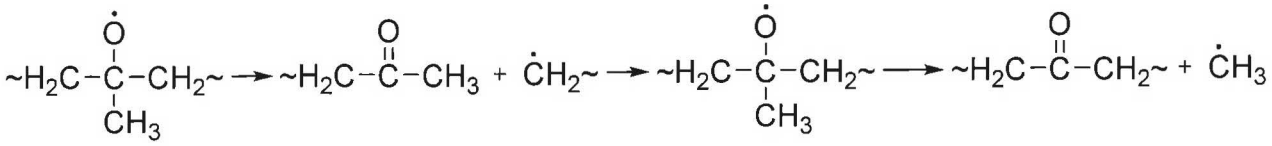

Scheme 3-6 Formation reaction of ketone groups and end radicals

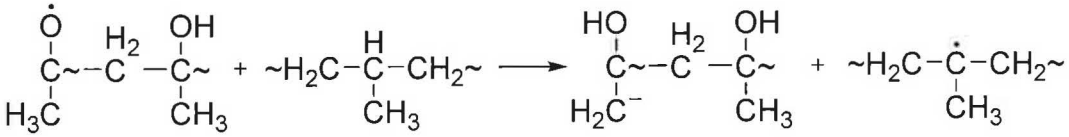

Scheme 3-7 Formation reactions of OH groups

The reactions of end radicals can result in the formation of the water-soluble low molecular weight species, the chain shorting, and etching (Scheme 3-8, Scheme 3-9).

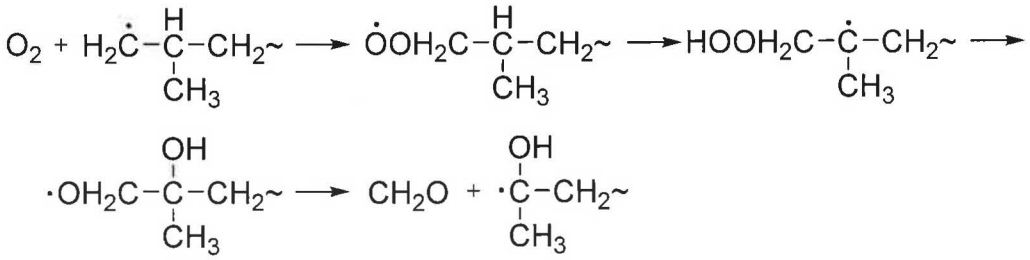

Scheme 3-8 Reactions of end radicals resulting in the formation of water-soluble oxidized species, the chain shorting and etching

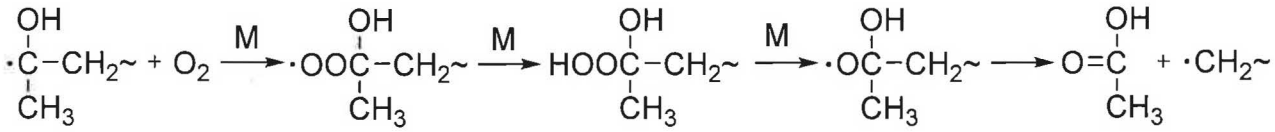

Scheme 3-9 Reactions of end radicals resulting in the formation of water-soluble oxidized species, the chain shorting and etching

According to that reaction scheme the ketone -C=O groups are dominant among other carbonyl ones. The reaction scheme proposed is similar to reactions of oxidative thermal destruction except of initiation step [130]. Under the plasma action the additional ways of reactions initiation appear ().

Scheme 3-10 Initiation reaction with participation of hydroxyl radical

Scheme 3-11 Initiation reaction with participation of hydroxyl radical

The reactions of alkyl radicals with O atoms can result in the formation of the carboxyl radicals and polymer chain scission (Scheme 3-12) followed by carboxyl radicals formation, polymer etching, and forming more wide set of carbonyl groups than in the case of afterglow action (Scheme 3-13 .. Scheme 3-16).

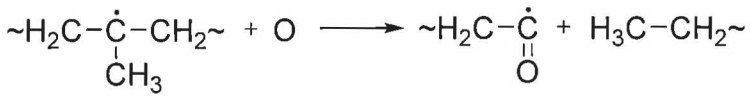

Scheme 3-12 Reactions of the carboxyl radicals formation and chain scission

Scheme 3-13 Reactions of the carboxyl radicals formation

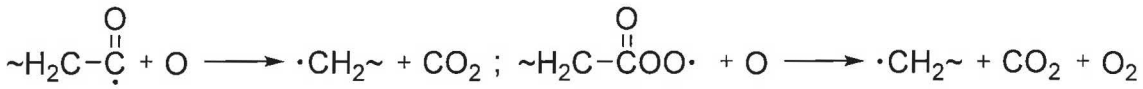

Scheme 3-14 Etching process

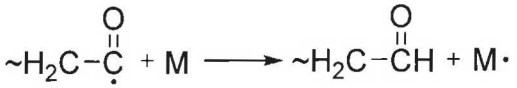

Scheme 3-15 Reactions of aldehyde groups formation

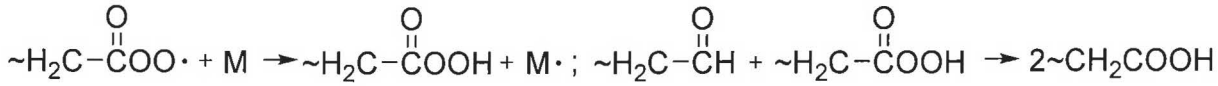

Scheme 3-16 Reactions of carboxyl groups formation

Undoubtedly, the reactions with participation of the O and OH radicals take place in afterglow as well. But their role is essentially less due to the difference in appropriate concentrations. Under treatment in plasma the higher etching rates restrict the concentrations of oxygen-containing species, the depth of modified layer, and leads to faster process kinetics. A different ratio between formation rates of carboxyl radicals and alkoxy ones results in other composition of the modified layer. Also, in plasma an additional way of the ketone groups destruction leading to a formation of carboxyl radicals can be the well-known Norrish reaction (Scheme 3-17) which promote a transformation of ketone carbonyl groups to other carbonyl groups according to the reaction scheme mentioned above. Of course, the weak spot in our discussion is that we do not take into consideration the possible reactions that occur after sample extraction from the reactors. Most probably a part of alkyl radicals will react with the atmospheric oxygen-forming hydroperoxide radicals followed by a hydroperoxides formation. The latter are stable at room temperature. For this reason, the measured concentration of the OH groups has to be little higher than the real concentration.

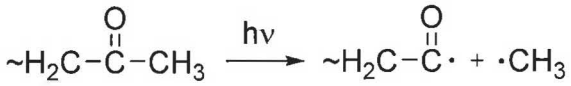

Scheme 3-17 Norrish reaction

Conclusions

- Nanocomposite Ti/hydrocarbon plasma polymer films as potential coating of various materials, including those used in medicine and biology, were deposited using DC magnetron sputtering of titanium target in argon and hexane working gas mixture.
- It has been shown that at magnetron current 0.2 A very small admixtures of hexane (Ar flow rate was 19 sccm, hexane flow rate 0.1 – 6 sccm) were sufficient to prepare nanocomposite Ti/hydrocarbon plasma polymer films.
- RBS/ERDA show 58 at.% of hydrogen content in the films rich with titanium.
- The films are shown to become more hydrophilic with decreasing of hexane flow rate.
- AFM measurement shows that the roughness of Ti/hydrocarbon plasma polymer films varies from 1.0 to 3.3 nm with increasing of Ti concentration on the surface.
- With increasing Ti content, the films become conductive, harder and show stronger adhesion to silicon as measured by Kelvin Force Microscopy and Visco-Elastic Atomic Force Microscopy, respectively.
- Biological response of the nanocomposite Ti/hydrocarbon plasma polymer films was studied in terms of adsorption of proteins and adhesion of cells. Fibrinogen adsorbs on the Ti/hydrocarbon plasma polymer films as a very soft layer with fibrinogen molecules adhering stronger to the Ti-rich films.
- Both Ti-rich and Ti-deficient films supported well the adhesion, growth and differentiation of human osteoblast-like MG 63 cells as well as bovine pulmonary artery endothelial cells of the line CPAE. In MG 63 cells, this supportive effect was similar to that on standard cell culture substrates represented by glass or polystyrene dishes, whereas in CPAE cells, the adhesion, growth and maturation were significantly enhanced on Ti-rich than on Ti-deficient films and standard cell culture substrates.
- Polypropylene foil modification was performed and showed that the flowing afterglow of water vapor discharge is quite promising for surface oxidation of PP films. Such treatment provided more homogeneous chemical composition of the modified layer as well as greater layer depth in comparison with water vapor and oxygen plasmas. The modification results were more stable in subsequent water washing.
- Possible explanation was proposed is terms of H radicals reacting with PP surface coating is successive reacting RO_2 and ROH that is dominant specie. High diffusion coefficient of atomic hydrogen is likely responsible for greater depth of the modified layer.

- The treatment of PP films led to the increase of surface-free energy and the polymer surface became smoother and homogeneous. In order to understand the process mechanism, further study of the composition of active species is necessary. Also, the study of polymer modification in plasma and its afterglow of O_2-H_2 mixture would be very useful.

References

1. Yasuda H., *Plasma Polymerization.* 1985, New York: Academic press.
2. Biederman H., Osada Y., *Plasma Polymerization Processes.* 1992, Amsterdam: Elsevier.
3. Williams T., Hayes M.W., Nature, 1966: p. 769.
4. Denaro A.R., Owens P.A., Crawshaw A., Europ. Polymer J., 1968. **4**: p. 93.
5. Denaro A.R., Owens P.A., Crawshaw A., Europ. Polymer J., 1969. **5**: p. 471.
6. Denaro A.R., Owens P.A., Crawshaw A., Europ. Polymer J., 1970. **6**: p. 487.
7. Westwood A.R., Europ. Polymer J., 1971. 7: p. 363.
8. Poll H.U., Z. angew. Physik, 1970. **29**: p. 260.
9. Poll H.U., Artz M., Wickleder K.H., Europ. Polymer J., 1978. **12**: p. 505.
10. D.K. Lam, R.F. Baddour, A.F. Stancell, *Plasma Chemistry of Polymers.* 1976, New York: Marcel Dekker.
11. J.M. Tibbitt, R. Jemsem, A.T. Bell, M. Shen, Macromolecules, 1977. **10**: p. 647.
12. Yasuda H., Hsu T., Surface Sci., 1978. **76**: p. 232.
13. d'Agostino R., Cramarossa F., Fracassi F., Illuzzi F., *Plasma Polymerization of Fluorocarbons in Plasma Deposition, Treatment and Etching of Polymers.* 1990, New York: Academic. 95-163.
14. Kvasnica S., Fallmann W., Biederman H., Boldyreva H., Slavínská D. in *15th Int. Symp. On Plasma Chemistry.* 2001. GREMI, CNRS/University of Orleans, Orleans, France.
15. J. Robertson, *Electronic processes in hydrogenated amorphous carbon.* J. Non-Cryst. Solids, 1996. **198-200**: p. 615.
16. M. Ohring, *The Materials Science of Thin Films.* 1992: Academic Press.
17. König H., Helwig G., Z Phys., 1951. **129**: p. 491.
18. Brockes A., König H., Z Phys., 1958. **152**: p. 75.
19. Schmellenmeier H., Exp. Techn. Phys., 1953. **1**: p. 49.
20. Pagnia H., Progress in Colloid & Polym. Sci., 1988. **78**: p. 143.
21. Whittmell D.S., Williamson R., Thin Solid Films, 1976. **48**: p. 255.
22. Holland L., UK Pat 1582231, 1976.
23. Nyaiesh A.R., Holland L., Vacuum, 1984. **34**: p. 519.
24. Biederman H., Martinů L., Zemek J., Vacuum, 1986. **35**: p. 447.
25. Wagner J., Wild C.H., Pohl F., Koidl P., Appl. Phys. Lett., 1986. **48**: p. 106.
26. Koidl P., Wild C.H., Locher R., Sah R.E., *Amorphous Hydrogenated Carbon Films and related Materials: Plasma Deposition and Film properties, Diamond and Diamond-Like Films and Coatings*, ed. C.R.E. et.al. 1991, New York: Plenum Press.
27. Bubenzer A., Dischler B., Brandt G., Koidl P., J. Appl. Phys., 1983. **54**: p. 4590.
28. R. d'Agostino, F. Cramarossa, F. Fracassi, F. Illuzzi, *Plasma Deposition, Treatment and Etching of Polymers*, ed. R. d'Agostino. 1990, new york: Academic Press.
29. F.W. Smith, J. Appl. Phys., 1984. **55**: p. 764.
30. Tkachuk B.V., Marusii N.Y., Laurs, E.P., Vysokomol. Soedin., 1973. **A15**: p. 2046.
31. Kny E., Levenson L.L., James W.J., Auerbach R.A., J. Vac. Sci. Technol., 1979. **16**: p. 359.
32. Kay E., Dilks A., Hetzler U., J. Macromol. Sci.-Chem., 1978. **A12**: p. 1393.
33. Biederman H., Martinů L., *Plasma deposition, treatment and etching of polymers*, ed. d.A. R. 1990, Boston: Academic Press.
34. Kay E., Z. Phys. D.- Atoms, Molecules and Clusters, 1986. **3**: p. 251.

35. Biederman H., Slavínská D., Bílková P., Stundžia V., in *Plasma Processing of Polymers*, F.P. d` Agostino R., Fracassi F., Editor. 1997, Kluwer Academic. Pub.: Dordrech, Boston, London. p. 365.
36. Luff P.P., White M., Vacuum, 1968. **18**(437).
37. Boonthanom N., White M., Thin Sol. Films, 1974. **24**: p. 295.
38. Abeles B., Appl. Solid State Sci., 1976. **6**: p. 1.
39. Craig S., Harding G.L., Thin Sol. Films, 1982. **97**: p. 345.
40. Harding G.L., Craig S., J. Vac. Sci. Technol., 1979. **16**: p. 857.
41. Sikkens M., Solar Energy Materials, 1982. **6**: p. 403.
42. Sikkens M., Solar Energy Materials, 1982. **6**: p. 415.
43. Weissmantel C., Breuer K., Winde B., Thin Solid Films, 1983. **100**: p. 383.
44. Dimigen H., Hubsch H., Memming R., Appl. Phys. Lett., 1987. **50**: p. 1056.
45. Klages C.P., Memming R., Mater. Sci. Forum, 1989. **52/53**: p. 609.
46. Bewilogua K., Dimmigen H., Surf. Coat. Technol., 1993. **61**: p. 144.
47. Window B., Savvides N., J. Vac. Sci.Technol., 1986. **A4**: p. 453.
48. Biederman H., Howson R.P., McCabe I. in *IPAT 87*. 1987.
49. Biederman H., Kohoutek K., Chmel Z., Stary V., Howson R.P., Vacuum, 1990. **40**: p. 251.
50. Monaghan D., Teer D.G., Logan P.A., Efeoglu I., Arnell R.D., Surface and Coatings Technology, 1993. **60**: p. 525.
51. Biederman H., Hlídek P., Pešička J., Slavínská D., Stundžia V., Vacuum, 1996. **47**: p. 1385.
52. Biederman H., Hlídek P., Pešička J., Slavínská D., Stundžia V., Zemek J., Kingdon R.J., Howson R.P., Vacuum, 1996. **47**: p. 1453.
53. Biederman H., Howson R.P., Slavínská D., Stundžia V., Vacuum, 1997. **48**: p. 883.
54. Biederman H., Stundžia V., Slavínská D., Žalman J., Pešička J., Vaněček, M., Zemek J., Fukarek W., Thin Sol. Films, 1999. **351**: p. 151.
55. Hlídek P., Biederman H., Boldyreva H., Slavínská D. in *15th Int. Symp. On Plasma Chemistry*. 2001. GREMI, CNRS/University of Orleans, Orleans, France.
56. Vyskočil J., Široký P., Vorlíček V., Peřina V., Diamond and Related Materials, 1996. **5**: p. 466.
57. LoBindo N. E., Aharonov R. R., Fontana R. P., Surface and Coating Technology, 1997. **94-95**: p. 652.
58. Kulikovsky V. Yu., Fendrych F., Jastrabik L., Chvostová D., Surface and Coatings Technology, 1997. **91**: p. 122.
59. Michler T., Grischke M., Bewilogua K., Dimigen H., Thin Solid Films, 1998. **322**: p. 206.
60. Krumpiegl T., Meerkamm H., Fruth W., Schaufler C., Erkens G., Böhner, Surface and Coatings Technology, 1999. **120-121**: p. 555.
61. Donnet C., Fontaine J., T. Le Mogne, M. Belin, C. Héau, J. P. Terrat, F., Vaux, G. Pont, Surface and Coatings Technology, 1999. **120-121**: p. 548.
62. Zehnder T., Patscheider J., Surface and Coatings Technology, 2000. **133-134**: p. 138.
63. Meng W. J., Meletis E. I., Rehn L. E., Baldo P. M., J. Appl. Phys., 2000. **87**: p. 2840.
64. Schüler A., Geng J., Oelhafen P., Brunold S., Gantenbein P., Frei U., Solar Energy Materials & Solar Cells, 2000. **60**: p. 295.
65. D. Strzeciwilk, Z. Wokulski, *Preparation of TiC crystals from high temperature solutions and their characterization.* Cryst. Res. Technol., 1999. **34**: p. 777–784.
66. M. Pancielejko, W. Precht, A.Czyzniewski, *Tribological properties of PVD titanium carbides.* Vacuum, 1999. **53**: p. 57-60.

67. R. S. Rawat, P. Lee, T. White, L. Ying, S. Lee, *Room temperature deposition of titanium carbide thin films using dense plasma focus device.* Surf. Coat. Technol., 2001. **138**: p. 159-165.
68. G. Radhakrishnan, P. M. Adams, *Pulsed-laser deposition of particulate-free TiC coatings for tribological applications.* Appl. Phys. A, 1999. **69**: p. 33-38.
69. A. A.Voevodin, M. A. Capano, S. J. P. Laube, M. S. Donley, J. S. Zabinski, Thin solid film, 1997. **298**: p. 107.
70. J. Vyskocil, P. Široký, V. Vorlicek, V. Perina, *Mechanical properties and Raman spectra of a-C:H and a-C:H:N coatings.* Diamond and Related Materials, 1996. **5**: p. 466-470.
71. C. Bauer, H., Leiste, M. Stuber, S. Ulrich, H. Holleck, *Mechanical properties and performance of magnetron-sputtered graded diamond-like carbon films with and without metal additions.* Diamond and Related Materials, 2002. **11**: p. 1139-1142.
72. N. E. LoBiondo, R. R. Aharonov, R. P. Fontana, *An investigation of the properties of Ti-C:H films.* Surf. Coat. Technol., 1997. **94-95**: p. 652-657.
73. D. P. Monaghan, D. G. Teer, P. A. Logan, I. Efeoglu, R. D. Arnell, *Deposition of wear resistant coatings based on diamond like carbon by unbalanced magnetron sputtering.* Surface coatings technology, 1993. **60**: p. 525-530.
74. T. Krumpiegl, H. Meerkamm,W. Fruth, C. Schaufler, G. Erkens, H. Böhner, *Amorphous carbon coatings and their tribological behaviour at high temperatures and in high vacuum.* Surf. Coat. Technol., 1999. **120-121**: p. 555-560.
75. R. d'Agostino, *Plasma deposition, Treatment and Etching of Polymers.* 1990: Academic Press.
76. R.N.S. Sodhi, *Application of surface analytical and modification techniques to biomaterials research.* J. Electr. Spectrosc. Phenom., 1996. **81**: p. 269.
77. Sioshansi P., Mater. Sci. Eng., 1987. **90**: p. 373.
78. Kizling M., Jaras S.G., *A Review of the Use of Plasma Techniques in Catalyst Preparation and Catalytic Reactions.* Appl. Catal. A: Gen, 1996. **147**(1): p. 1-21.
79. Ohl A., Schleinitz W., Meyer-Sievers A., Becker A., Keller D., Schroder K., Conrads J., *Design of an UHV reactor system for plasma surface treatment of polymer materials.* Surf. Coatings Technol., 1999. **116-119**: p. 1006-1010.
80. Ratner B.D., J. Biomater. Sci. Polym. Edn., 1992. **4**: p. 3.
81. Picraux S.T., Pope L.E., Science, 1984. **226**: p. 615.
82. Sioshansi P., Tobin E.J., Surf. Coatings Technol., 1996. **83**: p. 175.
83. Szycher M., Sioshansi P., Frisch E.E., *Biomaterials for the 1990s: Polyurethanes. Silicones and Ion Beam Modification Techniques.* 1990, Patriots Park, Bedford: Spire Corporation.
84. Ohl A., Schroder K., Surf. Coatings Technol., 1999. **116-119**: p. 820-830.
85. Vargo T.G., Bekos E.J., Kim Y.S., Ranieri J.P, Bellamkonda R., Aebischer P., Margevich D.E., Thompson P.M., Gardella J.A. Jr., J. Biomed. Mater. Res., 1995. **29**: p. 767.
86. Vargo T.G, Thompson P.M., Gerenser L.J., Valentini R.F., Aebischer P., Hook D.J., Gardella Jr. J.A., Langmuir, 1992. **8**: p. 130.
87. Inoue M., Suzuki Y., Takagi T., Nucl. Instrum. Meth. Phys. Res. B, 1997. **121**: p. 1.
88. Favia P., d'Agostino R., Surf. Coatings Technol., 1998. **98**: p. 1102.
89. M.S. Wagner, D.J. Graham, B.D. Ratner, David G. Castner, *Maximizing information obtained from secondary ion mass spectra of organic thin films using multivariate analysis.* Surface Science, 2004. **570**(1-2): p. 78-97.
90. Ratner B.D., Chilkoti A., Lopez G.P., *Plasma Deposition, Treatment and Etching of Polymers*, ed. R. d'Agostino. 1990, New York: Academic Press.

91. B. Window, N. Savvides, *Charged particle fluxes from planar magnetron sputtering sources.* J. Vac. Sci. Technol. A, 1986. **4**(2): p. 196-202.
92. S.Kvasnica, *Diagnostic of plasma polymerization process.* 1997, Charles University: Prague.
93. A.N. Magunov, Kolloid. Zh., 1989. **51**: p. 162.
94. A.N. Magunov, Vysokomolekularnye Soedineniya Ser.A, 1989. **31**: p. 1334.
95. A.J. Kinloch, *Adhesion and Adhesives, Science and Technology.* 1987, London: Chapman & Hall.
96. Bačáková L., Mareš V., Bottone M.G., Pellicciari C., Lisá V., Švorčík V., *Fluorine-ion-implanted polystyrene improves growth and viability of vascular smooth muscle cells in culture.* J. Biomed. Mater. Res., 2000. **49**: p. 369-379.
97. Bačáková L., Mareš V., Lisá V., Švorčík V., *Molecular mechanisms of improved adhesion and growth of an endothelial cell line cultured on polystyrene implanted with fluorine ions.* Biomaterials, 2000. **21**: p. 1173-1179.
98. Safi I., *Recent aspects concerning DC reactive magnetron sputtering of thin films: a review.* Surf. Coatings Technol., 2000. **127**(2): p. 203-219.
99. Pearse R. W. B., Gaydon A. G., *The identification of molecular spectra.* 4 ed. 1976: London: Chapman and Hall.
100. H. Biederman, RP Howson, D. Slavinska, V. Stundzia, J. Zemek, Vacuum, 1997. **48**: p. 883.
101. H. Biederman, P. Kudrna, D. Slavinska, *Hard plasma polymers, composites and plasma polymer films prepared by rf sputtering of conventional polymers*, in *Plasma Polymer Films*, H. Biederman, Editor. 2004, Imperial College Press: London.
102. T. Ishitani, R. Shimizu, Appl. Phys., 1975. **6**: p. 241.
103. K. Nakamoto, *Infrared and Raman Spectra of Inorganic and Coordination Compounds.* 1986: John Wiley & Sons.
104. M. Kosmulski, Colloids Surf. A, 2003. **222**: p. 113.
105. M Malmsten, J.-A. Johansson, N. L. Burns, H. K. Yasuda, Colloids Surf. B, 1996. **6**: p. 191.
106. T. R. Gengenbach, Z. R. Vasic, R. C. Chatelier, H. J. Griesser, Polym. Sci. A, 1994. **32**: p. 1399.
107. P. Cacciafesta, A. D. L. Humphris, K. D. Jandt, M. J. Miles, Langmuir, 2000. **16**: p. 8167.
108. K. Makino, H. Ohshima, T. Kondo, J. Colloid Interface Sci., 1987. **115**: p. 65.
109. P. Bernabeu, A. Caprani, Biomaterials, 1990. **11**: p. 258.
110. S.-Y. Jung, S.-M. Lim, F. Albertorio, G. Kim, M. C. Gurau, R. D. Yang, M. A. Holden, P. S. Cremer, J. Am. Chem. Soc., 2003. **125**: p. 12782.
111. V. Balasubramanian, N. K. Grusin, R. W. Bucher, V. T. Turitto, S. M. Slack, J. Biomed. Mater. Res., 1999. **44**: p. 253.
112. Z. Zhang, Q. Chen, W. Knoll, R. Foerch, R. Holcomb, D. Roitman, Macromolecules, 2003. **36**: p. 7689.
113. A. Choukourov, A. Grinevich, N. Saito, O. Takai, Surf. Sci., 2007. **601**(18): p. 3948.
114. S. Kidoaki, T. Matsuda, Langmuir, 1999. **15**: p. 7639.
115. Schroeder A., Francz G, , Bruinink A, Hauert R, Mayer J, Wintermantel E, *Titanium containing amorphous hydrogenated carbon films (a-C: H/Ti): surface analysis and evaluation of cellular reactions using bone marrow cell cultures in vitro.* Biomaterials, 2000. **21**: p. 449-456.
116. Bačáková L., Starý V, Kofroňová O, Lisá V, *Polishing and coating carbon fiber-reinforced carbon composites with a carbon-titanium layer enhances adhesion and*

growth of osteoblast-like MG63 cells and vascular smooth muscle cells in vitro. J. Biomed. Mater. Res., 2001. **54**: p. 567-578.

117. Carinci F., Volinia S., Pezzetti F., Francioso F., Tosi L., Piattelli A., *Titanium-cell interaction: analysis of gene expression profiling.* J Biomed Mater Res B Appl Biomater, 2003. **66**: p. 341-346.
118. Zlatanov I., Groth T., Lendlein A., Altankov G., *Dynamics of beta1-integrins in living fibroblasts--effect of substratum wettabilityDynamics of beta1-integrins in living fibroblasts--effect of substratum wettability.* Biophys J., 2005. **89**: p. 3555-3562.
119. Webster T.J., Smith T.A., *Increased osteoblast function on PLGA composites containing nanophase titania.* J Biomed Mater Res A., 2005. **74**: p. 677-686.
120. Polonchuk L., Elbel J., Eckert L., Blum J., Wintermantel E., Eppenberger H.M., *Titanium dioxide ceramics control the differentiated phenotype of cardiac muscle cells in culture.* Biomaterials, 2000. **21**: p. 539-550.
121. Price R.L., Ellison K., Haberstroh K.M., Webster T.J., *Nanometer surface roughness increases select osteoblast adhesion on carbon nanofiber compacts.* J Biomed Mater Res A., 2004. **70**: p. 129-138.
122. Kwok S.C., Yang P., Wang J., Liu X., Chu P.K., *Hemocompatibility of nitrogen-doped, hydrogen-free diamond-like carbon prepared by nitrogen plasma immersion ion implantation-deposition.* J Biomed Mater Res A., 2004. **70**: p. 107-114.
123. Okpalugo T.I., Ogwu A.A., Maguire P.D., McLaughlin J.A., *Platelet adhesion on silicon modified hydrogenated amorphous carbon films.* Biomaterials, 2004. **25**: p. 239-245.
124. H. Biederman, P. Bílková, J. Jezek, P. Hlídek, D. Slavínská, J. Non-Crystalline Solid 1997. **218**: p. 44.
125. H.Biederman, D. Slavínská, H. Boldyreva, H. Lehmberg, G. Takaoka, J. Matsuo, H. Kinpara , J. Zemek, *Modification of polycarbonate and polypropylene surfaces by argon ion cluster beams.* THE JOURNAL OF VACUUM SCEINCE AND TECHNOLOGY B, 2001. **19**: p. 2050-2056.
126. M. Strobel, M. J. Walzak, J.M. Hill, A. Lin, E. Karbashewski and C.S. Lyons, J. Adhesion Sci. Technol., 1995. **9**: p. 365.
127. N. Inagaki, S. Tasaka, T. Umehara, J. Appl. Polym. Sci., 1999. **71**: p. 2191.
128. M. Strobel, V. Jones, C.S. Lyons M. Ulsh, M. J. Kushner, R. Dorai and M.C. Branch, Plasmas and Polymers, 2003. **8**: p. 61.
129. V. Rybkin, A. Bessarab, E. Kuvaldina, A. Maximov, V. Titov, Pure & Appl.Chem., 1996. **68**: p. 1041.
130. E.T. Denisov, O.M. Sarkisov, G.I. Likhtenshtein, *Chemical Kineticks Fundamentls and New Developments*. 2003, Amsterdam: Elsevier.
131. Dorofeev, Y.I., High Energy Chemistry, 2004. **38**: p. 221.
132. M. Strobel, C.S. Lyons, J. Adhesion Sci. Technol., 2003. **1**: p. 15.
133. E.V. Kuvaldina, V.V. Rybkin,V.A. Titov, T.G. Shikova and D.A. Shutov, High Energy Chemistry, 2005. **39**: p. 337.
134. A. Hollaender, J.E. Klemberg-Sapieha and M.R. Wertheimer, J. Polym. Sci. A: Polym.Chem., 1995. **33**: p. 2013.
135. T.G. Shikova, V.A. Titov, V.V. Rybkin, H.S. Choi, High Energy Chemistry, 2006. **40**: p. 351.
136. A.N. Ponomarev, A.I. Maximov, V.N. Vasiletz, V.M. Menagarishili, High Energy Chem., 1989. **23**: p. 286.
137. A. Hollaender, J.E. Klemberg-Sapieha and M.R. Wertheimer, Macromolecules, 1994. **27**: p. 2893.

138. G. Kühn, St. Weidner, R. Decker, A. Ghode, J.F. Friedrich, Surf. Coatings Technol., 1999(116-119): p. 796.
139. A.K. Shuaibov, L.L. Shimon, A.I. Dashchenko, I.V. Shevera, Tech. Phys. Letters, 2001. **27**: p. 642.
140. A.H. Mahan, A. Gallaher, S.J. Smith, Phys. Rev. A, 1976. **13**: p. 156.
141. R.R. Laher, F.R.Gilmore, J. Phys. Chem. Ref. Data., 1990. **19**: p. 277.
142. Yu.I. Dorofeev, V.E. Skurat, N.A. Slovohotova, F.F. Suhov, R.R. Shifrina, Khim. Vys. Energ. **12**: p. 354.
143. G. Scott, *Atmospheric Oxidation and Antioxidants*. 1965, Amsterdam: Elsevier Co.
144. A.I. Maximov, V.Yu. Dubrovin, V.V. Rybkin, Izvestia VUZov. Khimia i Khimicheskaya Tekhnologia, 1979. **22**: p. 1469.
145. R.C. Reid, T.K. Sherwood, *The properties of gases and liquids. Their estimation and correlation*. 1966, New York, San Francisco, Toronto, London, Sydney: McGraw-Hill Company.
146. D.R. Lide, *Handbook of Chemistry and Physics*. 1998-1999, New York: CRC Press.

List of publications

(Journal articles refereed)

1. V. Rybkin, E. Kuvaldina, A. Grinevich, A. Choukourov, H. Iwai, H. Biederman, *"A comparative study of polypropylene surface oxidation in DC low pressure oxygen and water vapor discharges and in flowing afterglow of water vapor discharge"*, Plasma Proc. and Polym., 2008, available online at www.interscience.wiley.com, DOI: 10.1002/ppap.200800057

2. A. Grinevich, L. Bačáková, A. Choukourov, H. Boldyryeva, Y. Pihosh, D. Slavínská, L. Nosková, M. Škuciová, V. Lisá, H. Biederman *"Nanocomposite Ti/hydrocarbon plasma polymer films from reactive magnetron sputtering as growth supports for osteoblast-like and endothelial cells"*, J. of Bio. Mat. Res. A, 2008, available online at www.interscience.wiley.com, DOI: 10.1002/jbm.a.31918

3. A. Choukourov, A. Grinevich, D. Slavinska, H. Biederman, N. Saito, O. Takai, *"Scanning probe microscopy for the analysis of composite Ti/hydrocarbon plasma polymer thin films"*, Surf. Sci., 602/5, 2008, 1011-1019

4. A. Choukourov, A. Grinevich, N. Saito, O. Takai, *"SPM analysis of fibrinogen adsorption on solid surfaces"*, Surf. Sci., 601/18, 2007, 3948-3951.

5. Z. Remes, A. Kromka, M. Vanecek, A. Grinevich, H. Hartmannova, S. Kmoch, *"The RF plasma surface chemical modification of nanodiamond films grown on glass and silicon at low temperature"*, Diamond and Rel. Mat., 16, 2007, 671-674

6. Chichina M, Tichy M, Kudrna P, Grinevich, A., Churpita, O., Hubicka, Z., Kment, S., Olejnicek J: *A study of barrier-torch plasma jet system at atmospheric pressure*, Czechoslovak Journal of Physics 56: B1212-B1217 Part 6 Suppl. B 2006

7. A. Choukourov, J. Hanus, J. Kousal, A. Grinevich, Y. Pihosh, D. Slavinska, H. Biederman, *"Plasma polymer films from sputtered polyimide"*, Vacuum, 81, 2006, 517-526.

8. A. Choukourov, J. Hanus, J. Kousal, A. Grinevich, Y. Pihosh, D. Slavinska, H. Biederman, *"Thin polymer films from polyimide vacuum thermal degradation with and without a glow discharge"*,Vacuum, 80, 2006, 923-929.

9. A. Choukourov, A. Grinevich, J. Hanus, J. Kousal, D. Slavinska, H. Biederman, A. Bowers, L. Hanley, *"A comparison of polyatomic ion deposited, RF magnetron sputtered and plasma polymer organosilicon films"* Thin Solid Films, 502, 2005, 40-43.

10. A. Choukourov, H. Biederman, D. Slavinska, L. Hanley, A. Grinevich, A. Boldyryeva, A. Mackova, *"Mechanistic studies of plasma polymerization of allylamine"* J. Phys. Chem. B., 109, 2005, 23086-23095.

(Proceedings and other)

1. A. Choukourov, A, Grinevich A., Hanuš J., Kousal, J., Slavínská, D., Biederman, H., Bowers, A., Hanley, L.: *A comparison of polyatomic ion d eposited, RF magnetron sputtered and plasma polymer organosilicon films*, In: Proceedings of the 5th International Conference on Coatings on Glass ICCG5 July 4-8, 2004, Eds. J. Puetz, A. Kurz, M.A. AegerterSaarbruecken, Germany, p.119-124.

2. A. Grinevich: *Plasma Polymer Processes in Biomedical Applications*, Proceedings of contributed papers WDS 04, Ed. J. Šafránková, Matfyzpress Praha 2004, Part III, 508-512.

3. A. Choukourov, A. Grinevich, D. Slavínská, H. Biederman: *Ultra-Thin Coatings Deposited by Plasma Polymerization of Allylamine*, In: IV International Symposium on Theoretical and Applied Plasma Chemistry, 13.-18. 5. 2005 Ivanovo, Rusko Sbornik trudov, 1, 273-276. ME 554, BM MSM 113200002, US NSF 9986226

4. A. Grinevich A, Choukourouv A., Koshelyev H., Biederman H., Slavínská D., Boldyryeva H., Bačáková L., Pešička J.: *Nanocomposite Ti/hydrocarbon plasma polymers for biomedical aplications*, Proceedings of contributed papers WDS 05, Ed. J. Šafránková, Part III, Matfyzpress Praha 2005, 545-549. ISBN80-86732-59-2

5. A. Grinevich, J. Hanus, A. Choukourov, H. Koshelyev, H. Biederman, D. Slavínská, H.Boldyryeva, L. Bačaková, J. Pešička: *Nanocomposite Ti/hydrocarbon plasma polymers for biomedical applications* In: 17th International Symposium on Plasma Chemistry. Abstracts and full-papers CD, Eds. J. Mostaghimi, T.W. Coyle, V.A. Pershin, H.R.Slimi Jazi, University of Toronto 2005, 714-715. MSM0021620834

6. J. Kousal, J. Hanus, A. Choukourov, A. Grinevich, Y. Pihosh, P. Hlidek, P. Zemek, H. Biederman, D. Slavinska , *Diagnostics of plasma polymerization process in RF magnetron sputtering and evaporation of polymers*, In: 17th International Symposium on Plasma Chemistry. Abstracts and full-papers CD, Eds. J. Mostaghimi, T.W. Coyle, V.A. Pershin, H.R.Slimi Jazi, University of Toronto 2005, 675-676. MSM0021620834. OC 527.10

7. A. Choukourov, H. Biederman, D. Slavinska, J. Hanus, J. Kousal, A. Grinevich, L. Hanley, *Amine rich coatings prepared by plasma polymerization of allylamine*, In: 17th International Symposium on Plasma Chemistry. Abstracts and full-papers CD, Eds. J. Mostaghimi, T.W. Coyle, V.A. Pershin, H.R.Slimi Jazi, University of Toronto 2005, 658-659. MSM0021620834, USNSF9986226

8. M. Drabik, A.Grinevich, Y. Pihosh, J. Kousal, A. Choukourov, M. Trchová, A. Macková, A. Boldyryeva, D. Slavínská, H. Biederman: *Nanocomposite SiOx/plasma polymer films*, In 2nd International Workshop on Polymer/ Metal Nanocomposites, GKSS Geesthacht Německo 2005, s. 39.

9. Grinevich A., A. Choukourov, H. Boldyryeva, Y. Pihosh, D. Slavínská, H. Biederman: *Nanocomposite Ti/hydrocarbon plasma polymer films from reactive magnetron sputtering*, Proceedings of contributed papers WDS 06, Eds. J. Šafránková and J. Pavlů, Matfyzpress Praha 2006, Part III, pp. 95-100

10. M. Chichina, P. Kudrna, M. Tichý, A. Grinevich, O. Churpita, Z. Hubička, S. Kment, J. Olejníček, *Measurements of the Plasma Parameters in RF Torch Discharge Used for Deposition of Oxide Thin Films*, Proceedings of contributed papers WDS 06, Eds. J. Šafránková and J. Pavlů, Matfyzpress Praha 2006, Part II, pp. 108-113

11. Choukourov A., A. Grinevich, N. Saito, O. Takai: *SPM analysis of fibrinogen adsorption on solid surfaces*, poster presentation, European Conference on Surface Science, ECOSS24, Paris, France, September 2006

12. Grinevich A., L. Bačáková, A. Choukourov, H. Boldyryeva, Y. Pihosh, D. Slavínská, L. Nosková, M. Škuciová, V. Lisá, A. Itakura, H. Biederman: *Nanocomposite ti/hydrocarbon plasma polymer films from reactive magnetron sputtering as growth supports for osteoblast-like and endothelial cells*, In: IVC 17 Documentation CD, July 2007 Stockholm, PSTFP4-152, poster

13. Itakura Akiko, Toda Masaya ; Grinevich Andrey; Chu Liqiang ; Miyake Koji; Foerch Renate; Berger Ruediger: *Young's modulus measurement of plasma-polymerized allylamine films by*

using micro cantilever sensors, In: IVC 17 Documentacion CD , July 2007 Stockholm, ASSP3-07, poster

14. Choukourov A., A. Grinevich, M. Drabik, D. Slavinska, H. Biederman, N. Saito and O. Takai: *Micro-patterned surface potential of allylamine plasma polymers tuned by nanoprobe chemistry*, In: 18th International Symposium on Plasma Chemistry in Kyoto, Japan on August 26 - 31, 2007

15. Grinevich A., A. Choukourov, Y. Pihosh, D. Slavinska and H. Biederman: *Nanocomposite Ti/hydrocarbon plasma polymer films from reactive magnetron sputtering*, In: 18th International Symposium on Plasma Chemistry in Kyoto, Japan on August 26 - 31, 2007

16. Choukourov, A. Grinevich, H. Boldyryeva, Y. Pihosh, D. Slavinska, H. Biederman, L. Noskova, M. Skuciova, V. Lisa, L. Bacakova: *Titanium/hydrocarbon plasma polymer films for biomedical applications*, In: International Workshop for Students and Young Researchers: New Perspectives of Plasma Science and Technology , Brno 2007. CD

17. A.Itakura, A.Grinevich, M.Toda & R.Berger, *Young's modulus of Organic Thin Film measured by MCS*, In: NIMS Seminar for Advanced Nanomaterials Researchers 26th Oct.2007 at NIMS Sengen, Japan

18. A.Itakura, A.Grinevich, M.Toda & R.Berger, *Young's Modulus Measurement of Organic Thin-films*, In: NIMS Forum--Research and Innovation, 1st November.2007 at Tokyo International Forum, Japan

19. A.Itakura, A.Grinevich, M.Toda & R.Berger, *Young's Modulus compared with Atomic Structure of Thin-films*, In: 27th Symposium on Surface Science Japan, 1st-3rd Nov.2007 at Institue of Industrial Science, Tokyo, Japan

20. A.Itakura, A.Grinevich, M.Toda, L.Chu, R.Foerch & R.Berger, *Young's Modulus measurement compare with Structure of the thin film*, In: Vacuum Conference (14-16 Nob.2007 Gakusyu-in University, Tokyo, Japan

21. A.Itakura, S.Igarashi, A.Grinevich, M.Toda & R.Berger, *Local stress control and patterning by using Self-assembled monolayer*, In: 12th Annual Meeting of Japan Science and Technology Agency (semi-closed) 26-27 Nov.2007 at Hotel Osaka Garden Palace, Osaka, Japan

22. A.Itakura, A.Grinevich, M.Toda & R.Berger, *Determination of Young's modulus by using micro cantilever sensors*, In: 51th Conference on Materials Science and Engineering, 27-29 Nov.2007 at Kyoto University, Kyoto, Japan

23. Choukourov, A., Grinevich, A., Slavinska, D., Biederman, H., Saito, N., Takai, O., *Scanning probe microscopy for analysis of composite Ti/hydrocarbon plasma polymer thin films*, In: XXVIII International Conference on Phenomena in Ionized Gases, July 15-20, 2007, Prague, Czech Republic, CD and book of abstracts p. 154 (poster 3P16-25)